
BOSE-EINSTEIN CONDENSATION
OF ^{41}K AND ^{87}Rb ON AN ATOM CHIP
FOR SOUNDING ROCKET MISSIONS

Von der QUEST-Leibniz-Forschungsschule der
Gottfried Wilhelm Leibniz Universität Hannover

zur Erlangung des Grades

Doktor der Naturwissenschaften
– **Dr. rer. nat.** –

genehmigte Dissertation von

Baptist Piest, M. Sc.
geboren am 19.09.1989
in Braunschweig

2021

Referent: Prof. Dr. Ernst Maria Rasel
Institut für Quantenoptik, Leibniz Universität Hannover

Korreferent: Dr. Dennis Schlippert
Institut für Quantenoptik, Leibniz Universität Hannover

Korreferent: Prof. Dr. Eric Charron
Université Paris-Sud & Université Paris-Saclay

Vorsitz: Prof. Dr. Klemens Hammerer
Institut für Theoretische Physik, Leibniz Universität Hannover

Datum der Promotion: 21.05.2021

Abstract

Bose-Einstein condensation of ^{41}K and ^{87}Rb on an atom chip for sounding rocket missions

More than two decades after the first experimental realization of Bose-Einstein condensation in 1995, bosonic quantum gases have become an important and widely used tool for many experiments in atomic, molecular and optical physics. They present an ideal source for atom interferometry on long timescales due to their superior coherence properties, smaller size and slower expansion rates compared to thermal ensembles. Currently, many experiments strive to improve the accuracies of atom interferometers to measure tiniest accelerations of the probed ensemble. These efforts make atom interferometry a promising tool to probe the validity of the Einstein equivalence principle on a quantum level by using two different test masses. Satellite missions like STE-QUEST have been proposed to perform measurements of the Eötvös parameter using ^{41}K and ^{87}Rb with uncertainties below 10^{-15} . With the seminal drop tower experiments of the QUANTUS consortium, the sounding rocket mission MAIUS-1 and the long-term operation of the earth-orbiting Cold-Atom-Laboratory (CAL) aboard the International Space Station (ISS), the generation of Bose-Einstein condensates in miniaturized setups has entered a new level of technical maturity.

This thesis presents the next generation atom chip apparatus for the sounding rocket missions MAIUS-2 and -3. With the new apparatus, Bose-Einstein condensates containing $3 \cdot 10^5$ atoms of ^{87}Rb or $6 \cdot 10^4$ atoms of ^{41}K are generated within 3.4 s in ground-based operation. In addition, quantum degenerate mixtures with variable isotope ratios can be provided. An analysis of sympathetic cooling of ^{41}K under the influence of gravity and prospects for thermalization rates in microgravity are given. The expansion dynamics of single species Bose-Einstein condensates released from a magnetic trap is analyzed in detail. It is shown that transient magnetic fields during trap switch-off have a considerable impact on the expansion dynamics. Further, collective excitations of single and mixed ensembles are evaluated. Due to interspecies damping, collective excitations of interacting mixtures of ^{41}K and ^{87}Rb are strongly suppressed. Finally, the influence of gravity on a trapped and strongly interacting mixture is observed via rotation of the whole apparatus.

The experimental results demonstrate the fast generation of ultracold ^{41}K - ^{87}Rb mixtures in a compact and robust setup which is one of the pivotal requirements for spaceborne high accuracy tests of the Einstein equivalence principle. In the sounding rocket missions MAIUS-2 and -3, the new apparatus will perform differential atom interferometry based on Raman double diffraction of quantum-degenerate ^{41}K and ^{87}Rb .

Key words: Bose-Einstein condensation, quantum-degenerate mixtures, microgravity, space

Kurzfassung

Bose-Einstein-Kondensation von ^{41}K und ^{87}Rb auf einem Atomchip für Höhenforschungsraketenmissionen

Mehr als zwei Jahrzehnte nach dem experimentellen Nachweis der Bose-Einstein-Kondensation 1995 sind bosonische Quantengase zu einem wichtigen und weit verbreiteten Untersuchungsgegenstand in Atom-, Molekül- und optischer Physik geworden. Im Vergleich zu thermischen Ensembles weisen sie eine höhere Kohärenzlänge sowie eine geringere Größe und Expansionsgeschwindigkeit auf, wodurch sie eine ideale Quelle für die Atominterferometrie auf langen Zeitskalen darstellen. Derzeit streben viele Experimente eine Verbesserung der Genauigkeit von Atominterferometern an, um kleinste Beschleunigungen der Testmassen zu detektieren. Aufgrund dieser Bemühungen gelten Atominterferometer mit zwei unterschiedlichen Testmassen heutzutage als eine der sensitivsten Instrumente für die Durchführung von Quantentests des Äquivalenzprinzips. In der Vorstudie STE-QUEST werden satellitenbasierte Messungen des Eötvös-Parameters mit einer Unsicherheit unterhalb von 10^{-15} mit Hilfe von ^{41}K und ^{87}Rb vorgeschlagen. Durch die wegweisenden Fallturmexperimente der QUANTUS-Kollaboration, der Höhenforschungsraketenmission MAIUS-1 und des langfristigen Betriebs des Cold-Atom-Laboratory (CAL) an Bord der Internationalen Raumstation (ISS) hat die Erzeugung von Bose-Einstein-Kondensaten in miniaturisierten Aufbauten einen hohen Reifegrad erreicht.

Im Rahmen dieser Arbeit wird die atomchipbasierte Experimentierkammer für den Einsatz in den Höhenforschungsraketenmissionen MAIUS-2 und 3 aufgebaut und mit einem bodengestützten System in Betrieb genommen. Die neue Apparatur ermöglicht innerhalb von 3,4 s die Erzeugung von Bose-Einstein-Kondensaten mit $3 \cdot 10^5$ ^{87}Rb -Atomen oder $6 \cdot 10^4$ ^{41}K -Atomen. Zusätzlich können quantenentartete Mischungen mit variablen Isotopenverhältnissen bereitgestellt werden. In Untersuchungen zur sympathetischen Kühlung von ^{41}K durch ^{87}Rb wird der Einfluss der Gravitation auf Thermalisierungsraten quantifiziert. Das Expansionsverhalten frei fallender Bose-Einstein-Kondensate wird für beide Isotope untersucht. Transiente Magnetfelder während des Ausschaltens der Magnetfalle zeigen dabei einen erheblichen Einfluss auf die Expansion und müssen in Simulationen berücksichtigt werden. Im Rahmen der Analyse kollektiver Anregungen reiner und gemischter Kondensate kann eine gegenseitige Dämpfung der Anregungen aufgrund der gegenseitigen Wechselwirkung aufgezeigt werden. Schließlich wird der Einfluss der Gravitation auf den Grundzustand und die Massenschwerpunktsbewegung der wechselwirkenden Ensembles durch Rotation der Apparatur in Flugzeitmessungen untersucht.

Die experimentellen Ergebnisse demonstrieren die schnelle Erzeugung ultrakalter Mischungen aus ^{41}K und ^{87}Rb in einem kompakten und robusten Aufbau, wodurch eine der Grundvoraussetzungen geplanter atominterferometrischer Tests des Äquivalenzprinzips im Weltraum erfüllt ist. Ausblickend wird die neue Apparatur in den Höhenforschungsraketenmissionen MAIUS-2 und -3 differentielle Atominterferometrie basierend auf doppelter Ramanbeugung an Materiewellen aus ^{41}K und ^{87}Rb durchführen.

Schlagwörter: Bose-Einstein Kondensate, quantenentartete Mischungen, Mikrogravitation, Weltraum

Contents

1	Introduction	1
1.1	Atom interferometry in microgravity	2
1.2	Experiments on microgravity platforms	3
1.3	MAIUS-B	4
1.4	Scope of this thesis	5
2	Experimental Apparatus	7
2.1	Vacuum system	7
2.1.1	Source chamber and atom reservoir	10
2.1.2	Science chamber and atom chip	14
2.1.3	Detection system	16
2.2	Laser system	20
2.2.1	Overview of ground-based laser system	20
2.2.2	Laser system for manipulation of potassium atoms	21
2.2.3	Laser system for manipulation of rubidium atoms	24
2.2.4	Fiber splitter	24
2.3	Control system	26
2.3.1	TBus system	26
2.3.2	Current drivers and batteries	28
2.3.3	Calibration and characterization of current drivers	29
2.3.4	Temperature control	30
2.3.5	Software	30
2.4	Flight system	31
3	Generation of quantum degenerate mixtures of ^{87}Rb and ^{41}K	35
3.1	Cooling and trapping of mixtures	35
3.1.1	Chip-MOT and molasses	35
3.1.2	Magnetic trapping	37
3.2	Bose-Einstein condensation of ^{87}Rb	39
3.2.1	General remarks	39
3.2.2	Microwave evaporation of ^{87}Rb	42
3.3	Sympathetic cooling of ^{41}K	44
3.3.1	Inelastic collisions of mixed ensembles	46
3.3.2	Thermalization of ^{41}K and ^{87}Rb mixtures in gravity	50
3.4	Summary and perspectives	55

4 Dynamics of single and mixed BECs	59
4.1 Free expansion of ^{41}K and ^{87}Rb BECs	60
4.2 Free expansion of ^{41}K	63
4.3 Collective excitations	66
4.4 Free expansion of ^{87}Rb	68
4.5 Gradient-free magnetic trap release of mixtures	69
4.6 Influence of gravity on immiscible BECs in cylindrical traps	71
4.7 Summary and perspectives	73
5 Summary and Outlook	77
5.1 Transport	77
5.2 Delta-kick collimation	78
5.3 State preparation	80
5.4 Interferometry	80
5.5 Conclusion	83
Bibliography	85
Curriculum Vitae	109

CHAPTER 1

Introduction

Major discoveries in modern physics are often accompanied by larger improvements of experimental techniques which allow to measure basic principles or quantities with unmatched sensitivity. Among the most prominent examples is the first direct observation of gravitational waves [Abb16] which has only been possible due to the maturity of large-scale laser interferometers [Aas15]. In the field of atomic, optical and molecular physics, there is a continuously growing number of experiments which attempt to constrain fundamental theories by high-precision measurements [Saf18]. At the forefront of high sensitivity devices are atom interferometers which are based on the coherent properties of matter waves [Cro09; Tin14]. In such devices, the atomic ensemble is coherently split up into a spatial superposition in which the different interferometer arms accumulate a phase. As in laser interferometers, this phase can be read out by superimposing the interferometer arms after some evolution time. The versatility and power of atom interferometers stem from the fact that very small potential energy differences seen by the different arms translate into a large phase shift at the output ports of the interferometer. During the last decades many experimental and theoretical efforts were made in the field of atom interferometry. Up to now, these devices have been proven to work as sensors susceptible for absolute gravity [Bid13; Har16; Hau13; Pet01], gravity gradients [Ase17; Ros15], rotations [Ber15; Dut16; Tac12], magnetic field gradients [Har16], electric polarizability [Hol10] and black-body radiation [Has17]. Atom interferometry is also being used for the determination of fundamental constants like the Newtonian gravitational constant [Ros14] or the fine-structure constant [Par18].

Among the most appealing applications of atom interferometers is their utilization for testing the weak equivalence principle (WEP) which is one of the pillars of general relativity. The WEP asserts that the free fall acceleration of all particles shielded from any interactions but gravity is the same, independently of their internal composition and mass [Hau01]. Their trajectory is given by the geodesic equation which only depends on the curvature of space-time. Vice versa, any such two particles following different trajectories would imply a violation of this principle. Such violation is predicted by hypothetic models unifying gravity with other fundamental interactions, including quintessence [Wet03], fifth-force models [Dva02] and string theories [Dam02]. Any violation is expressed by a non-zero Eötvös factor $\eta = 2(a_2 - a_1)/(a_2 + a_1)$ which compares the accelerations a_1 and a_2 of the two test bodies. The T-SAGE instrument of the MICROSCOPE mission currently sets the upper bound $|\eta| < 1.3 \cdot 10^{-14}$ by measuring the differential acceleration of two encasing cylinders with different internal composition subject to Earth's gravitational field [Tou17].

By using two distinct elements or isotopes in an atom interferometer, the acceleration difference between them can be extracted by assessing the phase correlation of the interferometer output ports [Var09]. Thus, a value of η complementary to classical tests can be obtained with microscopic tests which rely on the quantum nature of matter. In contrast to macroscopic objects, quantum states offer unique access to internal degrees of freedom like different spin states. This enables to test a variety of WEP violating scenarios which are not accessible in classical tests. The phase shift ϕ for atom interferometers in Mach-Zehnder configuration scales according to $\phi = \mathbf{k} \cdot \mathbf{a}T^2$ with the wave number vector \mathbf{k} , the acceleration \mathbf{a} and the light pulse separation time T [Kas91]. Thus, the most efficient way to increase the sensitivity to the free fall acceleration and thereby to η is to increase T . In ground-based laboratories, T is constrained by the size of the apparatus which sets a limit to the quadratic scaling factor. Using atom interferometry, violations of the WEP have been constrained to uncertainties in the Eötvös ratio of 10^{-7} with ^{87}Rb and ^{39}K [Alb20b; Sch14a], 10^{-10} with ^{87}Rb and ^{85}Rb [Zho19] down to 10^{-12} , also with ^{87}Rb and ^{85}Rb [Ase20]. The striking leap of five orders of magnitude in accuracy within less than a decade illustrates the potential of atom interferometry for WEP tests. Today, the most accurate quantum tests of the WEP are performed in 10 m scale atomic fountains in order to maximize T . Extending the height of these devices is expected to push the accuracy further, as already several new experiments are under construction with baselines above 100 m [Ada18; Zha19]. However, increasing the baseline of large-scale devices will ultimately be bounded for technical reasons.

1.1 Atom interferometry in microgravity

A natural way to overcome this is given by transferring the whole apparatus into an Earth orbit. This does not only remove the limitation of the free fall time but will also be accompanied by further advantages:

- A reduction of ambient noise caused by vibrations due to the laboratory environment or geophysical processes. If the apparatus is designed as a standalone satellite without any mechanically moving parts there are only a few remaining sources of ambient vibrations like residual atmospheric drag. If used in differential mode, common-mode bias acceleration of the ensembles is rejected also in dynamic environments [McG02; Var09]. However, in single-mode operation inertial noise will be strongly suppressed compared to experiments on ground which is generally one of the major noise contributions in the interferometer output [Gou08; Hau13]. Thus, a vibration isolation or post-processing algorithms [Ric19a; Ric19b] to remove the influence of inertial noise to the interferometer signal is redundant in microgravity.
- The absence of gravity allows to release atoms from weak magnetic or optical traps which are not accessible on ground [Ave20]. This reduces the mean-field repulsion of the ensemble which leads to a velocity spread of the ensemble and thus to a loss of fringe contrast. Atoms released from weak traps are also ideal input states for delta-kick collimation techniques [Amm97].
- Perfect spatial overlap of two trapped species with different mass is not possible on ground without additional gravity compensating fields [Kle10; Lea03]. In micro-

gravity, this gravitational sag is naturally suspended. A position difference of two masses orbiting Earth leads to an atom-interferometric phase shift which might be misinterpreted as a WEP violating signal [Bla01].

- The motion of the satellite causes a frequency modulation of a possible WEP violating signal. By demodulation techniques commonly known from lock-in amplifiers the violating signal can efficiently be filtered out from noise in other frequency ranges. This technique has already been used in the MICROSCOPE mission [Tou17].
- Since the center-of-mass velocity of the atomic ensemble stays zero during the whole interferometer sequence, symmetric beam splitting techniques are naturally incorporated [Gie13; Lev09]. By this, detrimental phase contributions which depend on the momentum or internal atomic state cancel out in the interferometer output. Furthermore, the covered space-time area of the interferometer and thus its sensitivity to accelerations is increased.

In the mission proposal STE-QUEST, the feasibility of a satellite mission dedicated to test the WEP with an accuracy in the 10^{-15} range using delta-kick collimated ^{87}Rb and ^{85}Rb Bose-Einstein condensates (BEC) [Cor02; Ket02] and $T = 5$ s has been examined in detail [Agu14]. It turned out that such a measurement would require a level of control of the ensembles' initial positions and velocities beyond current technical capabilities. In particular, the position difference of the ensembles has to be known in the range of 10^{-9} m and the differential velocity at 10^{-10} m/s level. However, these colocation requirements were recently eased by techniques canceling the influence of gravity gradients [DAm17; Ove18; Rou17]. By combining these with the above mentioned demodulation technique, residual uncertainties of η in the range of 10^{-17} are targeted now using realistic experimental scenarios with ^{41}K and ^{87}Rb [Bat19; Lor20].

1.2 Experiments on microgravity platforms

Setting up an atom interferometer capable of conducting a WEP test in space is a tremendous task. The requirements on miniaturization, stability, sustainability and autonomous operation involve the combined knowledge from different disciplines. However, there is an ever-growing heritage from various experiments pioneering this field of research. In fig. 1.1, some landmark experiments on the track of a quantum test of WEP on a satellite platform like STE-QUEST are shown. The first realization of atom interferometry in a free-falling laboratory with thermal atoms has been demonstrated in 2009 in parabola flights [Ste09]. An important step towards payload miniaturization has been taken with the drop tower experiments in the QUANTUS collaboration, in particular the atom chip [For07] experiments QUANTUS-1 and QUANTUS-2. The first realization of Bose-Einstein condensation in a free falling laboratory has been demonstrated with the QUANTUS-1 experiment in the drop tower of the Center of Applied Space Technology and Microgravity (ZARM) in Bremen, Germany [Zoe10]. Using delta-kick collimated BECs, a symmetric atom interferometer has subsequently been realized in 2013 [Mün13]. The QUANTUS-2 experiment has shown the feasibility of realizing a high-flux ^{87}Rb BEC source in a miniaturized setup with a power consumption of only 364 W [Rud15] which is an achievable magnitude for space vehicles [Hec14]. Also, it demonstrated efficient delta-kick collimation with residual kinetic

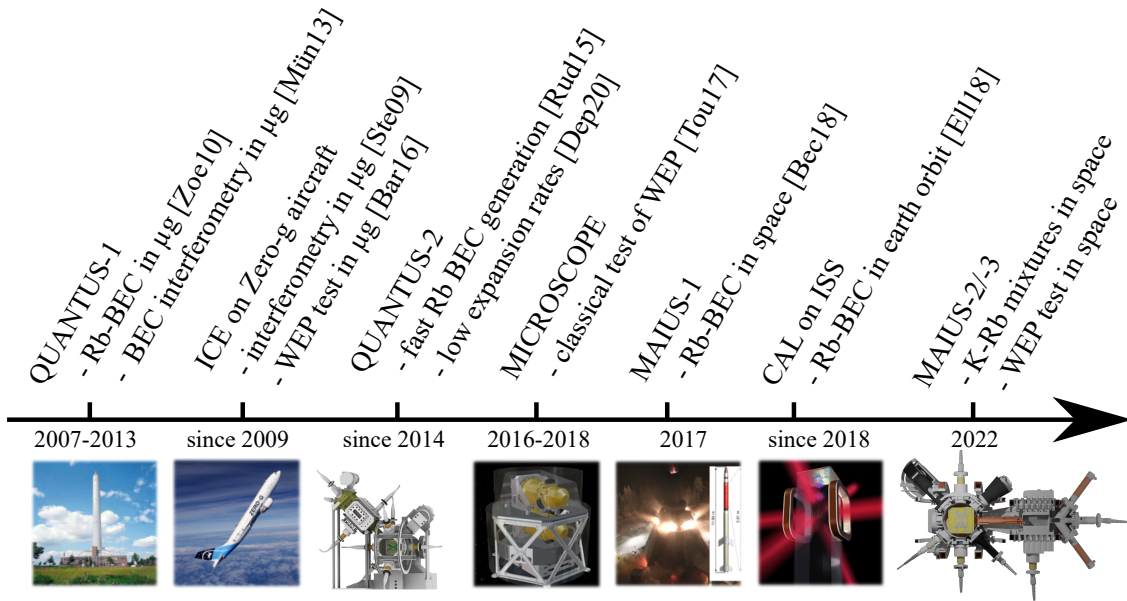


Figure 1.1: Overview of milestones towards a WEP test on a satellite platform. From left to right: The Bremen drop tower where the QUANTUS-1/-2 experiments are conducted (Image: ZARM), the Airbus A300 Zero-g aircraft as platform of the ICE experiment (Image: Novespace/CNES/DLR/ESA), a CAD drawing of the QUANTUS-2 physics package (Image: DLR), the MICROSCOPE satellite (Image: CNES/ONERA), the launch of the MAIUS-1 sounding rocket (Image: DLR), artist view of the CAL experiment onboard the International Space Station (ISS) (Image: JPL/NASA) and CAD drawing of the MAIUS-B experimental chamber.

energies of $U_{\text{kin}} = k_B \cdot 38 \text{ pK}$, enabling observation times of up to 17 s which is well above the requirements of the STE-QUEST proposal [Agu14; Dep21].

The first measurement of the Eötvös parameter with cold atoms on a microgravity platform was performed in 2016 using molasses cooled atomic samples of ^{39}K and ^{87}Rb onboard the Novespace A310 Zero-G aircraft [Bar16].

In 2017, the sounding rocket mission MAIUS-1 demonstrated the first Bose-Einstein condensation in space [Bec18]. During the flight, 110 experiments were conducted including an atom interferometer based on shear interference [Lac21]. Subsequent space-borne experiments with Bose-condensed ^{87}Rb atoms have been pursued since the installation of the Earth-orbiting laboratory CAL [Eil18] onboard the international space station (ISS) in 2018.

CAL will be replaced by the next-generation apparatus BECCAL [Fry19] which offers a versatile environment for a multitude of experiments using ultracold rubidium and potassium.

1.3 MAIUS-B

Despite the success of the seminal missions MAIUS-1 and CAL, a space-borne WEP test still remains elusive. The MAIUS-B experiment will approach this issue by providing a

payload which is capable of performing a WEP test in space using ^{87}Rb and ^{41}K . Hence, it will also demonstrate key concepts required for beyond state-of-the-art WEP test mission scenarios [Bat19].

The isotopes ^{41}K and ^{87}Rb represent an ideal choice for several technical and fundamental reasons: Technically, both isotopes have successfully been prepared in two-component BECs with controllable number ratios [Bur18]. The small spatial and narrow momentum distributions of delta-kick collimated BECs make them ideal input states for high-contrast atom interferometry. Due to the mutual proximity of the atomic transitions used for laser cooling and interferometry (780 nm for ^{87}Rb and 767 nm for ^{41}K), it can be drawn from existing narrow-band laser technology capable of space applications [Din16; Sch16]. Additionally, the interspecies interaction of both isotopes is magnetically tunable due to the zero crossing of a broad Feshbach resonance around 72 G [Kle07a; Tha08]. This allows to spatially overlap both ensembles in an optical trap by tuning the interspecies scattering length to zero. Fundamentally, a violation of the WEP in standard model extensions might be caused by a hypothetical charge which couples differently to the constituents of the test isotopes [Dam12]. A large difference in neutron excess of both test isotopes would enhance an anomalous differential acceleration [Har15; Sch14a]. Therefore, it is important to test various combinations of species depending on the violation scenario under consideration. The MAIUS-B apparatus builds upon the technological heritage of MAIUS-A but will allow for a number of additional studies focusing on atom interferometry and miscibility of ^{87}Rb and ^{41}K . These studies are performed in ground-based experiments and subsequently extended to microgravity in two consecutive sounding rocket missions, called MAIUS-2 and -3. They include the generation of BEC mixtures with tunable ratios of ^{41}K and ^{87}Rb at high repetition rate involving sympathetic cooling for the first time in microgravity. Additionally, MAIUS-B will underpin theoretical studies on the BEC ground state for mixtures of ^{41}K and ^{87}Rb examining the influence of gravity and interspecies interactions. By implementing two-species delta-kick collimation [Cor20; Tru18] and magnetic transport protocols [Amr19; Cor18], the applicability of this mixture for a WEP test will be examined experimentally. Finally, an atom interferometer with differential phase readout [Bar15; Bar16] using symmetric beam splitters based on Raman transitions will demonstrate a test of the WEP in microgravity.

1.4 Scope of this thesis

In this thesis, the MAIUS-B physics package and ground-based experiments with quantum mixtures of ^{41}K - ^{87}Rb are presented. Starting with an overview of the new apparatus in chapter 2, a ground-based testbed comprising a laser system, control electronics and an experimental control system is introduced. In chapter 3, experimental results on dual-species Bose-Einstein condensation with a focus on sympathetic cooling are presented. Following the mission goals, the ground state of the BEC mixture and the expansion dynamics of ^{41}K and ^{87}Rb are explored in chapter 4. In chapter 5, an outlook for future ground-based and prospects for microgravity measurements are given.

CHAPTER 2

Experimental Apparatus

In this chapter, an overview of the experimental apparatus MAIUS-B is given. The main focus lies on the setup of the physics package and the ground-based testbed comprising a laser system, electronics system and software environment. The integration of the physics package as part of the overall system in flight configuration is also briefly discussed.

2.1 Vacuum system

The design of the vacuum chamber is based on the MAIUS-A chamber [Sei14] which has demonstrated a high robustness against vibrational loads during transport, launch and reentry at the sounding rocket mission MAIUS-1. At the flight campaign in 2017, it has been shown that the system is capable to withstand temperature changes within the range between 30° C at reentry and down to -34° C ambient temperature at recovery, more than three days later. This robustness of the experimental chamber is an inevitable and distinctive feature of the MAIUS-A/-B apparatuses which ultimately allows to use the experiment in consecutive flights and further exploitation in micro-g facilities¹.

An overview of the vacuum chamber of MAIUS-B consisting of a pumping system together with two further chambers, referred to as science and source chamber is shown in fig. 2.1. By this two chamber design, a high-flux two-dimensional magneto-optical trap (2D-MOT) loaded from background vapor can be utilized as an atom source. At the same time, ultra-high vacuum conditions are maintained in the science chamber to provide the working conditions for BEC experiments. The resulting pressure gradient is maintained by a differential pumping stage which separates both chambers. To prevent magnetic stray fields and the earth magnetic field from affecting the internal states of the atoms, the science and source chambers are surrounded by a three-layer Mu-metal shield [Kub16] separating it from the pumping system and further external components. The pumping system comprises a titanium sublimation pump (*Vg Sienta ST22*), an ion getter pump (*Agilent VacIon 20 Plus Diode*) and a cold cathode gauge (*Pfeiffer IKR 270*) to directly measure the pressure at the pumping system down to the 10^{-11} mbar level. A second, home-built titanium sublimation pump is mounted at the science chamber inside the magnetic shield and has been manufactured using paramagnetic titanium Grade 5. The science chamber is connected to the pumping system with a CF16 connection and to the

¹ Depending on the facility, the whole payload might be split up into different modules to reduce the total height of the system.

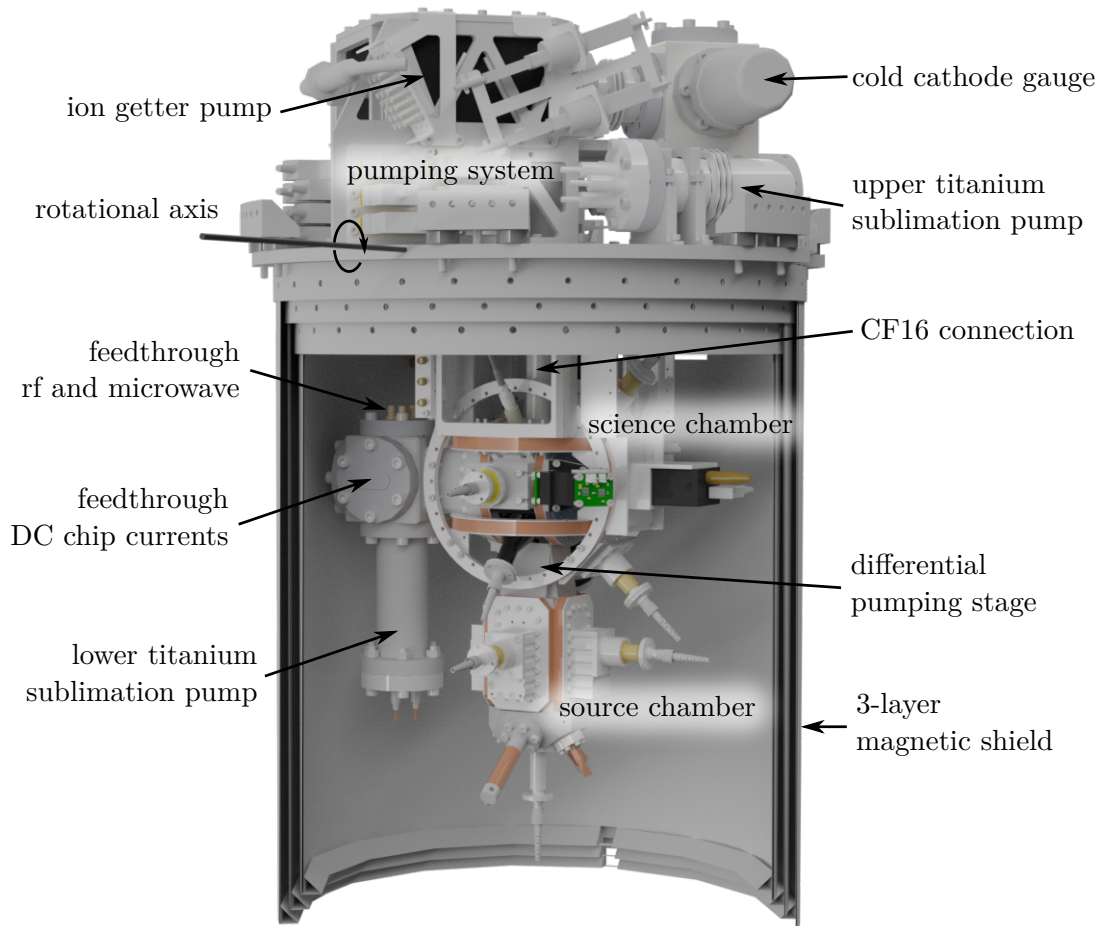


Figure 2.1: CAD drawing of the vacuum chamber and its mechanical design comprising the pumping system, science and source chamber. A detailed view of the science and source chamber within the magnetic shield is shown in fig. 2.3.

source chamber with a differential pumping stage (DPS) (see also in fig. 2.3). The DPS has a total length of 84 mm and expands from 1.5 mm to 7.0 mm in diameter. A graphite inlay increases the adsorption of rubidium and potassium atoms due to its large surface. Compared to MAIUS-A, the new vacuum system comes along with a few minor changes in the source chamber and the pumping system. Most importantly, the design of the atomic sources has been revised and the potassium source has been added to the system. A detailed characterization of the rubidium and potassium sources is given in chapter 2.1.1. Furthermore, the ion getter pump in the pumping system (*Agilent VacIon Plus 20*) has been mounted in a horizontal orientation in contrast to the 45° orientation in MAIUS-A to reduce the total height of the vacuum chamber [Els21].

To ensure high vacuum quality, macroscopic particles entering the vacuum chamber were avoided by cleaning all in-vacuum components with an ultrasonic bath and assembling the chamber in a clean room. During vacuum initialization with an external pump stand

consisting of a backing pump and a turbomolecular pump (*Pfeiffer HiCube 80 Classic*), the system was baked out at moderate temperatures of 80° C for four weeks. The temperature was limited to avoid any damage on the atom chip and its optical coatings. After the residual pressure measured by the gauge has reached a value below $< 3 \cdot 10^{-10}$ mbar, two glass ampoules containing potassium and rubidium in natural abundance were broken (cf. chapter 2.1.1) to provide a reservoir connected to the source chamber. Afterwards, the external pump system has been detached by sealing pinch-off tubes made of copper using a hydraulic jaw (*Custom Products & Services Inc. HY750*). This circumvents the use of valves which have been prone to leakages during vibrational tests [Sei14]. After activation of the titanium sublimation pumps, the residual pressure in the pumping system settles in the low 10^{-11} mbar range at room temperature. However, the pressure at the position of the atom clouds turned out to be an order of magnitude higher¹ such that the indicated value of the gauge serves only as a rough estimate. This is due to the reduced vacuum conductance of the CF16 connection between science chamber and pumping system and additional outgassing of the atom chip and its wires.

The vacuum chamber was qualified for the sounding rocket missions in vibrational tests at the Zentrum für angewandte Raumfahrtforschung und Mikrogravitation (ZARM) in Bremen. During these tests, different random vibrational profiles were applied, referred to as *acceptance* and *flight level* in the following. The *flight level* models the maximal expected vibration level of a VSB-30 rocket during launch with an RMS value of 2.0 g, with $g = 9.81 \text{ m/s}^2$. This value was not exceeded during a VSB-30 test flight [Gro16]. The vibration load of the more intense *acceptance level* is a factor of 2.7 above the flight level. This takes into account the higher loads during reentry which are expected to lie within this range. Respective frequency spectra of the applied vibrations are listed in table 2.1. The pressure at the pumping system was monitored during and after the tests which is shown in fig. 2.2. In these tests, the initial pressure before applying the random

Table 2.1: Random vibration test profiles with power spectral density (PSD) and root mean square (RMS) values along lateral and longitudinal axes. Each profile is applied for 60 s.

Frequency in Hz	PSD in g^2/Hz	
	acceptance level	flight level
20 - 400	0.002	0.0003
400 - 600	0.03	0.004
600 - 1300	0.002	0.0003
1300 - 2000	0.03	0.004
RMS Value	5.4 g	2.0 g

accelerations, was $2 \cdot 10^{-10}$ mbar due to an early state of the experiment which suffered from a virtual leakage inside the vacuum chamber stemming from fabrication residues. At flight level, the vacuum pressure rises by more than one order of magnitude to a value of

¹ The vacuum pressure can be determined by lifetime measurements and an analysis of the various atom loss channels in the atom chip trap [Bar21; Fol02].

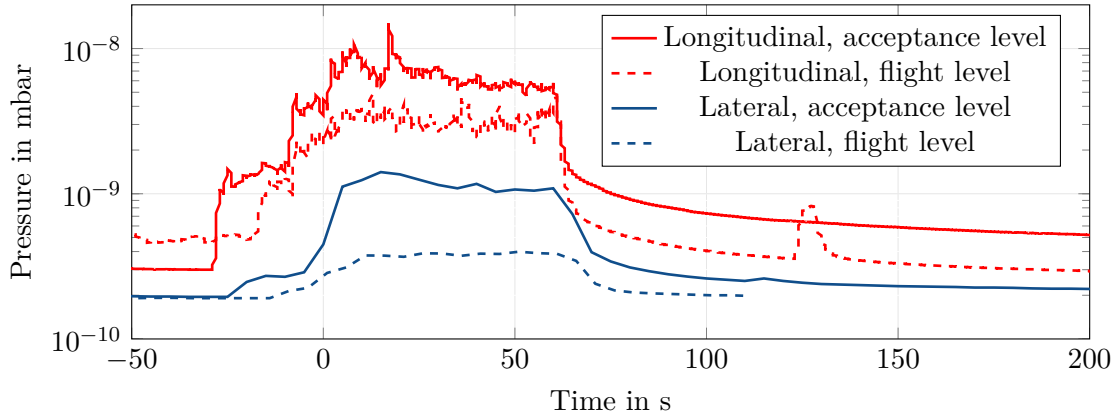


Figure 2.2: Measurement of the vacuum pressure during vibrational tests in longitudinal direction (red) and lateral direction (blue). At $t = 0$ s, the respective vibration profiles given by table 2.1 are applied to the system for 60 s. The flight level is indicated by dashed lines, the acceptance level by solid lines. The rise of pressure at $t < 0$ s is due to a stepwise increase of the vibrations to the nominal value.

$4 \cdot 10^{-9}$ mbar. After the vibration test (i.e. after burning and detachment of the rocket motor), the pressure decreases back to its initial value, being below $5 \cdot 10^{-10}$ mbar after 17 s. Vibrations in lateral direction have less impact on the vacuum pressure which stays below $1.5 \cdot 10^{-9}$ mbar during flight and acceptance level. Thus, the impact of vibrations is more severe in longitudinal direction. This behavior was also observed at a vibration test of the isolated pumping system, which narrowed down its cause to the mounting of the ion getter pump. Ensuring a fast decay of the vacuum pressure after launch is important to increase the lifetime of the trapped atoms. As a consequence, it has direct influence on the number of atoms left after evaporation. To speed up the settling time, the titanium layer generated by the sublimation pumps has to be renewed prior flight.

After fixing a virtual leakage inside the vacuum chamber, the pressure at the pumping system decreased an order of magnitude down to $2 \cdot 10^{-11}$ mbar. Thus, the here presented results of the vibration tests are expected to be outperformed by the current setup.

2.1.1 Source chamber and atom reservoir

In fig. 2.3, a cut through the science and source chambers is shown. Two alkali ovens are used to tune the rubidium and potassium vapor pressure within the source chamber. The design of the rubidium and potassium reservoir is depicted in fig. 2.4. In each oven, 1 g of potassium (*Strem Chemicals 93-1990 Potassium 1 g 99.95%*) or rubidium (*Strem Chemicals 93-3736 Rubidium 1 g 99.9+%*) in natural abundance are kept under protective atmosphere in a glass ampoule. The ampoules are broken once the system is under vacuum. A grit prevents broken glass fragments or parts of the not vaporized substance from entering the rest of the vacuum system. With a counterrotating heating coil, the temperature of a surrounding titanium cylinder can be controlled to change the temperature of each alkali reservoir independently. Thus, the vapor pressure within the source chamber can be tuned for each species separately. A higher vapor pressure of rubidium or potassium

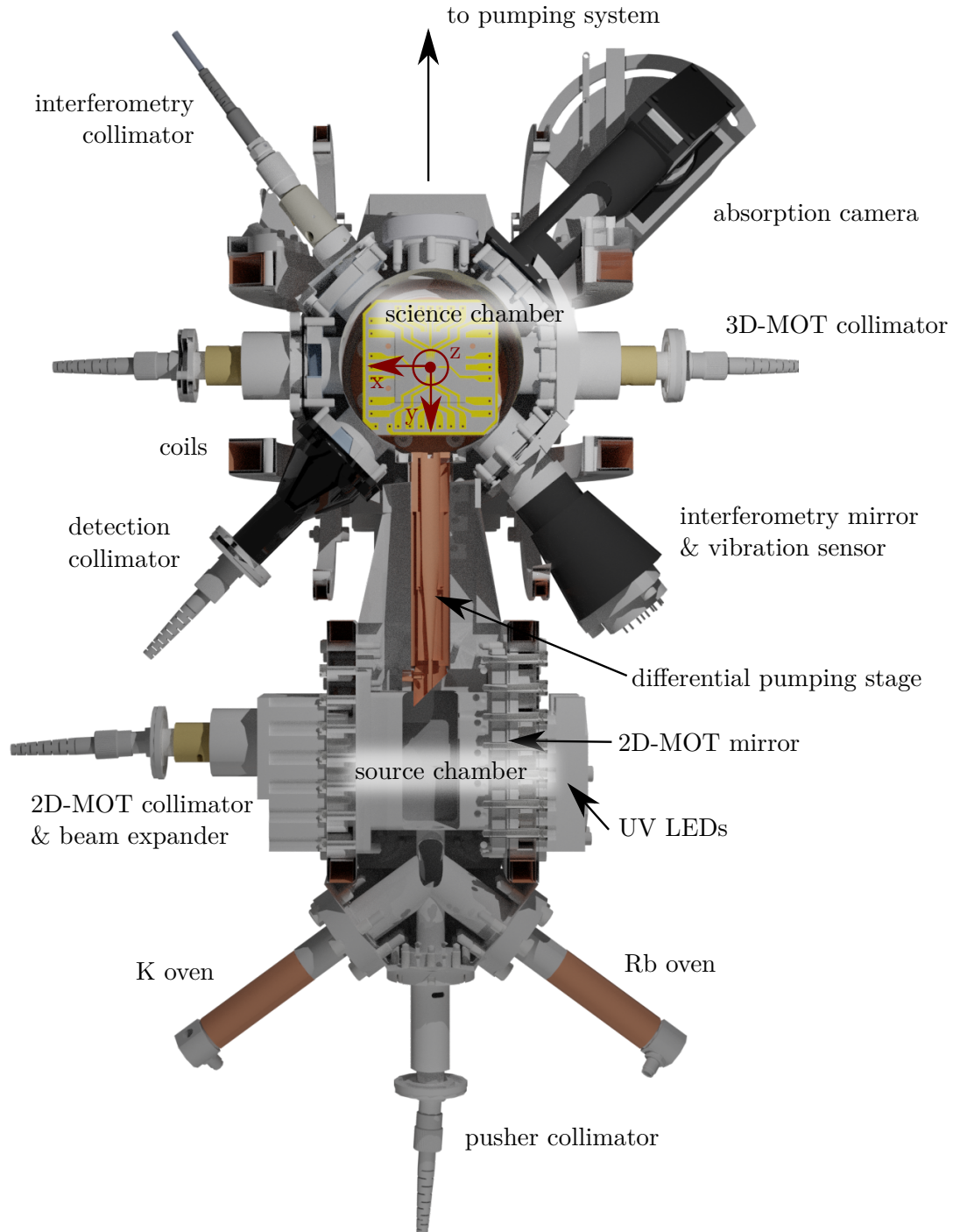


Figure 2.3: Rendered image of the science and source chamber (top view). The pumping system is not shown here and is indicated with an arrow. On top of the atom chip, the coordinate system is defined which is used throughout this thesis. The origin sits on the surface of the Science chip.

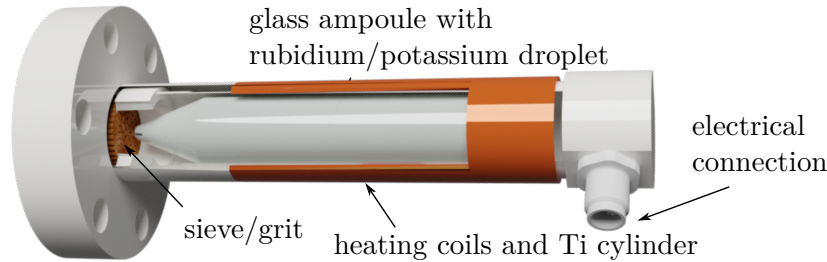


Figure 2.4: CAD image of the alkali oven. The ampoule is broken by directed mechanical stress using two screws on opposite sides of the cylinder.

increases the flux of the corresponding 2D-MOT¹. However, it turned out that a high vapor pressure of rubidium leads to a chemical reaction with the indium sealing of the vacuum windows. Ultimately, this has led to severe leakages in the MAIUS-A chamber which could be verified by a chemical analysis of the indium residues using X-ray fluorescence spectroscopy. Although the same problems have not been reported with potassium yet, it is safe to assume a similar behavior for all alkaline elements here. It is therefore beneficial to keep both oven temperatures as low as possible. In this work, the rubidium oven is kept at room temperature while the potassium oven is heated up to approximately 50° C.

By monitoring the incoming and outgoing intensity of laser light at the D2-transition of ⁸⁷Rb passing through two opposite windows in the source chamber, the number of absorbing atoms within the beam path can be measured [Sei14]. Given the temperature of the chamber walls, the ⁸⁷Rb partial pressure in the source chamber can subsequently be inferred using the ideal gas law. By using this method, the vapor pressure in the source chamber is measured during a gradual decrease of the oven temperature from 43° C to 26° C over 33 min. The results are shown in fig. 2.5 (top panel) and demonstrate the vapor pressure virtually following the temperature at the oven.

Likewise, also vibrations and shocks might show a considerable impact on the partial pressure, for example during rocket launch. This might be ascribed to a temporal increase of the surface of the alkali droplets during vibrations which would enhance the amount of vaporized atoms. Within the scope of the vibration tests, the influence of vibrations on the vapor pressure of ⁸⁷Rb was analyzed, as shown in fig. 2.5 (bottom panel). Since the temperature of the laboratory and the slip table changed during the measurement series, the increase of vapor pressure can not be solely caused by the exposure to vibrations.

Four rectangular coils in anti-Helmholtz configuration are placed around rectangular N-BK7 vacuum windows and provide a two-dimensional quadrupole field which is symmetric along the axis connecting the source and science chamber. The 2D-MOT is set up in a retroreflective configuration and the atomic flux is enhanced by using a further pusher collimator to accelerate atoms into the science chamber. The polarization of the 2D-MOT laser beams is tuned from linear to circular behind beam expanders by using two custom-built rectangular

¹ By adding a pusher and retarder light field to the 2D-MOT for ⁸⁷Rb, the flux increases with higher vapor pressure until a temperature optimum is reached as shown in [Cha06].

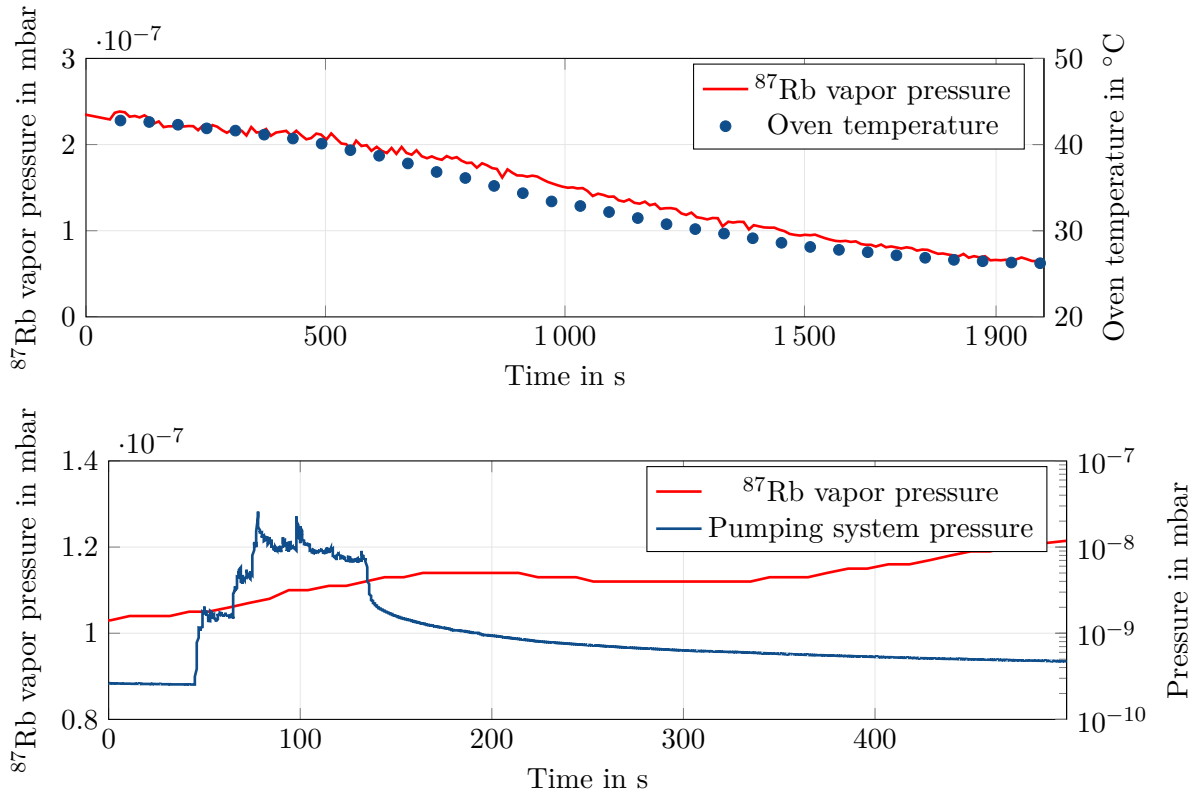


Figure 2.5: Top panel: Temporal change of ^{87}Rb vapor pressure in the source chamber (red curve) during change of rubidium oven temperature (blue dots). Bottom panel: Temporal change of ^{87}Rb vapor pressure in the source chamber (red curve) during a vibration test of the longitudinal axis. The blue curve represents the pressure measured at the pumping system using the vacuum gauge and indicates the vibration exposure. The oscillations in ^{87}Rb vapor pressure can be attributed to the periodic change of the air condition fins in the laboratory. The residual linear slope can not necessarily be correlated with the vibration exposure due to continuous heat transfer from the slip table to the experiment.

quarter-wave plates (*Foctek, true zero@773 nm AR-coated*) which rotate 767 nm and 780 nm light into the same circular helicity.

Flux measurements with a further retarder collimator [Cha06] being reflected at the wedged surface of the differential pumping stage showed no simultaneous gain in atomic flux for both two species compared to the configuration using only additional pusher light.

A slight and immediate enhancement of the vapor pressure in the source chamber can be achieved by shining ultraviolet (UV) light into the chamber by three UV light emitting diodes (LEDs). This technique is based on light induced atomic desorption (LIAD) and can be understood as an atomic analogue of the photoelectric effect [Tor15]. It is commonly used in single chamber experiments and works most efficiently on glass surfaces [Kle06].

2.1.2 Science chamber and atom chip

Like in all other experiments of the QUANTUS and MAIUS family, the core of MAIUS-B is the atom chip. It is located in the center of the science chamber and is used to generate a variety of magnetic field configurations at the position of the atoms. Additionally, microwave and radiofrequency fields are transferred to the vacuum chamber using its structures to enable couplings between internal atomic states based on oscillating magnetic fields. The design of this chip has originally been developed for the QUANTUS-2 apparatus [Her13] and is shown in fig. 2.6. A photograph of the complete assembly after electrical connection is shown in fig. 2.7. It consists of three layers which are glued on top of each other. The outermost layer (a) provides mesoscopic copper wires in U-, H- and I-geometry to generate magnetic field configurations resulting in a quadrupole or harmonic trapping potential. The Mesoscopic structures provide large volume quadrupole or harmonic traps with a center at distances of several millimeters from the chip surface. They are primarily used to generate the quadrupole magnetic fields for the 3D-MOT and a Ioffe-Pritchard trap [Wil04] for magnetic trapping. Typical currents used in these structures are in the order of 5-10 A which is limited by the wire diameter (*Allectra 311-KAP2*, $\varnothing 0.6$ mm). To allow for higher magnetic field gradients, the U-structure is enhanced by a five-fold, the H- and I-structures by a two-fold winding. They are fixed on a bulk copper block which acts as a heat reservoir.

The next layer above the Mesoscopic structures is the Base chip (b) which consists of an aluminum nitride (AlN) substrate. On top of the substrate, gold structures in different shapes are grown using microfabrication techniques. Shown in magenta is the outermost Z-structure (Base-Z) which is used to create a harmonic trap in combination with externally applied homogeneous bias fields along its plane. It serves as a medium size magnetic trap

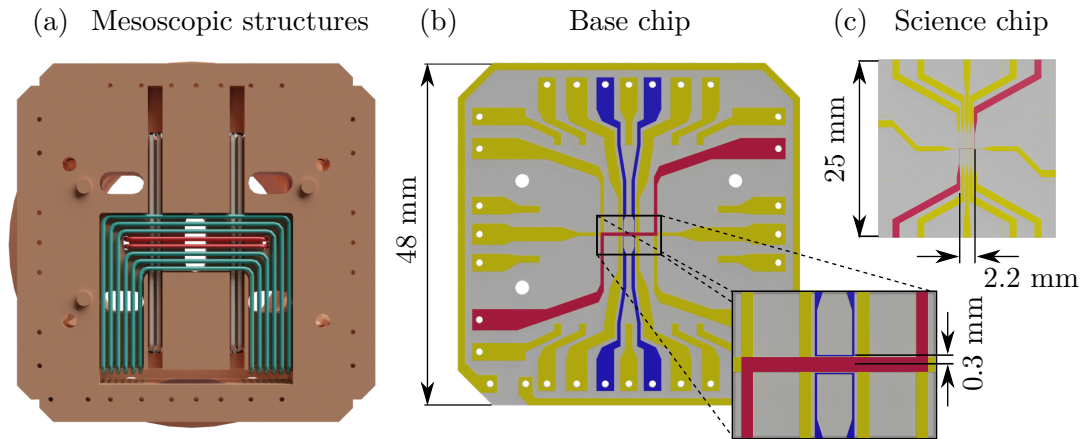


Figure 2.6: The three layers of the atom chip comprising the (a) Mesoscopic structures, (b) Base chip and (c) Science chip. The Mesoscopic structures consist of U- (cyan), I- (red) and H-structures (gray). The Z-structures of the Base and Science chip used for magnetic trapping close to the chip surface are highlighted in magenta. The structures used for microwave and radiofrequency manipulation are shown in blue. The holes around the Base chip are used for electrical connections.

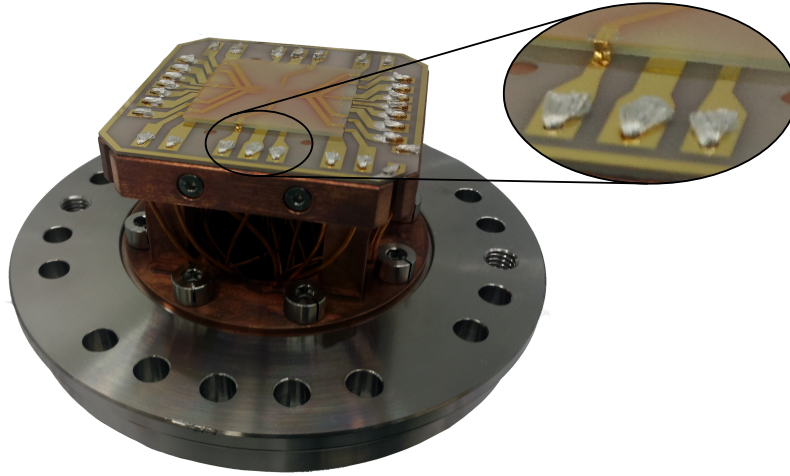


Figure 2.7: Photograph of the atom chip assembly mounted on the vacuum flange. The magnified view shows exemplarily a bonded gold ribbon between the two layers and the glued wires which are connected to the electrical vacuum feedthroughs.

which can also be utilized for magnetic lensing of the atomic ensembles (see also 5.2). Above and below the central Z-structure with a distance of $300\ \mu\text{m}$ are U-shaped structures (shown in blue) which are used to create microwave and radiofrequency fields at the position of the atoms. The employed microwave frequencies are in the range of the hyperfine splittings of the ground states of ^{87}Rb and ^{41}K , which are 6.8 GHz and 256 MHz, respectively. Typical radiofrequencies are in the range of moderate Zeeman-splittings (0.1 - 50 MHz). These oscillating magnetic fields are conveniently used for evaporative cooling of magnetically trapped atoms (cf. chapter 3.2), for driving internal transitions between Zeeman substates or hyperfine levels using direct Rabi transitions, and for adiabatic transfer or stimulated Raman adiabatic transfer techniques [Dup15]. A thorough characterization of the properties of the generated microwave fields and the implementation of an adiabatic transfer is given in [Mis20]. The structures can also be employed to generate adiabatic radiofrequency or microwave potentials which can be used for trapping [Hof06] or for continuous out-coupling of trapped atoms to form an atom laser [Bol14]. Since the position of the atom ensembles is typically in the near-field regime of these structures which is governed by high intensity gradients, they are also suitable to study the ac-Zeeman effect [Fan18].

The topmost layer of the atom chip assembly is the Science chip (c) which is glued centrally on the Base chip. The AlN substrate has a thickness of $635\ \mu\text{m}$. Parallel and directly above the Base chip Z-structure, it contains a further microscopic Z-structure which has a central length of 2.2 mm and thickness of $10\ \mu\text{m}$ (Science-Z). In combination with external bias fields, small volume magnetic traps close to the chip surface are formed by this structure providing trapping frequencies up to a few kHz. To connect the conductive gold structures of the Science chip with the structures of the larger Base chip, a thin gold ribbon is bonded between them (see inset in fig. 2.7).

The gold structures of the Science and Base chip are bonded with stranded wires which

are glued at the edge of the Base chip layer. All conductive structures of the three chip layers are accessible outside the chamber via vacuum feedthroughs in D-Sub standard (see fig. 2.1). The microwave and radiofrequency structures of the Base chip are connected via coaxial cables (*380-SMA-MX-500-S*) with SMA feedthroughs to keep power losses due to high frequency emission low.

The Science chip is coated with a high-reflective dielectric mirror (*OIB Jena*) which provides a reflectivity of more than 99.5% for 780 nm light at 45° incidence angle. The coating enables to implement a mirror-MOT using only four collimators with two of them being superimposed via reflections on the chip surface [Rei99].

The atom chip was manufactured in-house at the Laboratorium für Nano- und Quantenengineering in Hannover by M. Sahelgozin. For further details on the microfabrication techniques used to create the structures, it is referred to her thesis [Sah19].

To generate the quadrupole and harmonic traps above the atom chip, three external pairs of bias coils are needed in addition to the chip structures which are placed around the chamber. To distinguish between the different coils, they are named according to their magnetic field component which they produce (i.e. x-, y- and z-coil, see fig. 2.3 for coordinate system definition). To allow for a precise tuning of the magnetic field at high offset currents, the y-coil is further split into a large and small coil (y1- and y2-coil). In the course of this thesis the coils are serially connected. However, it might be advantageous to control them separately if small changes of a magnetic field in y-direction show large effects, for example in the vicinity of a Feshbach resonance [Tha08]. The characteristics of the bias coils are listed in table 2.2.

The science chamber can optically be accessed from the side by six N-BK7 viewports with a diameter of 30 mm. From the top, a 86 mm viewport allows direct optical access to the atom chip surface. This is used by fluorescence detection and two further 3D-MOT collimators which are mounted on 45° orientation to the atom chip to form the mirror-MOT configuration. Additionally, a closed waveguide with a design wavelength of 6.8 GHz is directed onto the atom chip to couple in additional microwave fields externally.

2.1.3 Detection system

For atom detection, two different systems are used in perpendicular orientation. One is based on absorption detection, the other one on atomic fluorescence. The cameras (*Point*

Table 2.2: The technical characteristics of the bias coils used in the experiment. The magnetic fields have been calibrated using microwave spectroscopy of cold ^{87}Rb clouds. The y-coils are connected serially which results in the single value of the magnetic field. The separation refers to the center-to-center distance.

coil	diameter in mm	separation in mm	windings	magnetic field in G/A
x-coils	157	76	21	2.54
y1-coils	121	65	85	14.42
y2-coils	138.3	65	17	
z-coils	95	49	30	5.37

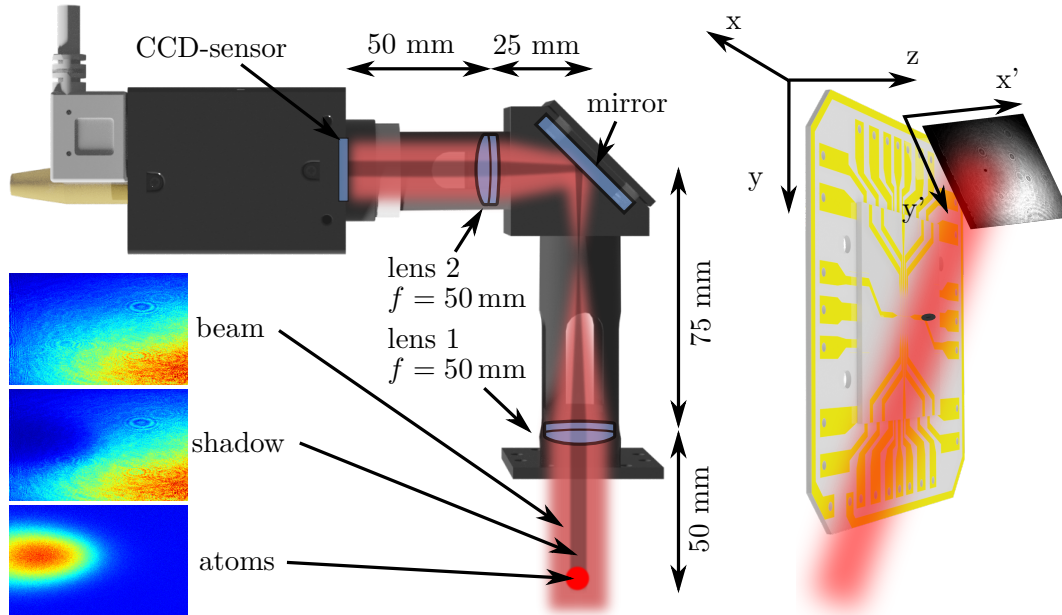


Figure 2.8: CAD drawing of absorption detection setup, image construction and coordinate system of absorption pictures. In the left panel, images of the detection beam with and without atoms are shown. The bottom picture shows the calculated density distribution of the atom cloud [Rei07].

Grey GS3-U3-15S5M) feature an ICX825 charged couple device (CCD) sensor with a pixel size of $6.45 \mu\text{m}$ and a resolution of 1384×1032 pixels. They provide an image buffer of 128 MB which can be read out using a USB 3.0 interface. The outer protective glass has been removed from the devices. Additionally, a second protective glass covers the CCD-sensor and could only be removed externally by a specialized company (*EURECA*) which led to a considerably improved image quality without any spurious interference fringes. The quantum efficiency of the cameras has been determined experimentally to 0.42^1 for a wavelength of 780 nm.

In the fluorescence detection setup, the light from the atoms is imaged with an aspheric lens (*Edmund Optics #49-114*, $d = 25 \text{ mm}$) in a $2f-2f$ ($f = 25 \text{ mm}$) configuration onto the camera sensor. The detection system is oriented directly onto the atom chip such that the axes of the recorded images coincide with the x- and y-axis of the Cartesian atom chip coordinate system which is defined in fig. 2.3. To reduce stray light, especially reflections coming from the central vacuum viewport, the lens is fixed in a black anodized lens tube reaching from the viewport to the camera sensor. Due to reflections of the detection light at the metallic surface of the atom chip copper holder and the connection wires, the fluorescence detection suffers from a high background signal which is proportional to the

¹ This is slightly higher than the value stated in the datasheet which is caused by the removed protective glasses.

light intensity. In order to avoid reflections at the copper mount of the atom chip, the unexploited part of the detection beam is cut with a razor blade behind the collimator. The magnification of the fluorescence imaging system depends on the distance between the atoms and the lens. Depending on the orientation of the experiment with respect to gravity, the magnification factor might change for different free fall times of the atoms.

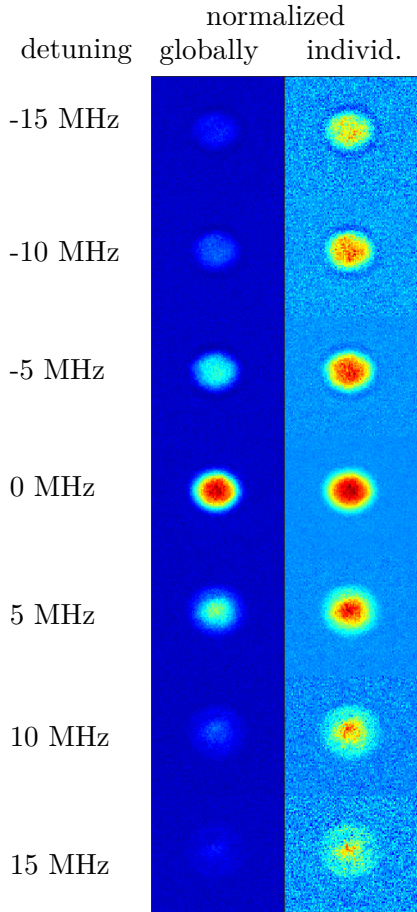


Fig. 2.9: Absorption pictures of ^{87}Rb BECs over a wide range of detection light detunings to resonance after calibration of the imaging system. The left image series shows all pictures normalized globally. The right series is normalized individually such that diffraction features are better visible. The diffraction patterns around the cloud have been minimized via tuning the position of the second lens of the absorption detection system.

detuning of the imaging beam to the atomic resonance $|F = 2\rangle \leftrightarrow |F' = 3\rangle$ which leads to a change of its refractive index over the detuning. Therefore, a misaligned focus of the

As shown in fig. 2.8, the absorption detection is able to image the plane spanned by $\mathbf{e}_{x'} = \mathbf{e}_z$ and $\mathbf{e}_{y'} = 1/\sqrt{2}(\mathbf{e}_y - \mathbf{e}_x)$ with $\mathbf{e}_{x',y'}$ denoting the direction vectors of the image axes and $\mathbf{e}_{x,y,z}$ the axes of the chip coordinate system. It consists of a pair of two achromatic lenses (*Linos/Qioptiq G322265525*) with a diameter of 18 mm and a focal length of $f = 50$ mm arranged in a 90° folded f-2f-f geometry. The light is reflected at a rectangular mirror between the two lenses in order to fit the detection setup within the magnetic shield. In an external setup with a USAF-1951 test target, a resolution down to $9.8_{-1.2}^{+0} \mu\text{m}$ is reached under optimal conditions with the test target at the center of the imaging system. By moving the test target to the corner of the field of view, the resolution drops to $17.7_{-2.0}^{+0} \mu\text{m}$ due to spherical aberration. The resolution is therefore not limited by the pixel size of the camera sensor. To limit specular reflections and stray light entering the absorption detection, all components are anodized black.

Due to the Gaussian envelope of the absorption beam, the atoms would be detected with different intensities depending on their position along the beam. In order to work in a similar intensity regime along different distances z to the chip surface, the Gaussian profile of the detection beam is flattened by using an apodizing filter (*Thorlabs NDY10B*). To avoid high frequency distortions due to a non-zero parallelism of the surfaces of the filter, it is attached in a 1.5° wedged mount between collimation lens and vacuum viewport.

The final alignment of the lens positions at the science chamber is done *in-situ* via minimization of diffraction patterns around absorption pictures of Bose-Einstein condensed ^{87}Rb clouds. The dielectric function of the dense cloud strongly depends on the

detection system would result in altering diffraction patterns around the BEC which can be minimized by adjusting the position of the focus lens. At the optimal setting, most of the diffraction patterns can be mitigated as shown in 2.9.

The magnification m of the absorption detection system is experimentally determined to $m = 0.991$ in a time-of-flight series of free falling ^{87}Rb atoms assuming a local gravity of $a = 9.813 \text{ m/s}^2$ [Bon12], shown in fig. 2.10. For this measurement, the experiment was rotated such that gravity points along z-direction. In this configuration, a free fall time of up to 40 ms can be observed until the atom cloud leaves the detection area. This corresponds to a maximum observable distance of 8 mm to the atom chip surface. The measured value $m = 0.991$ confirms the positioning of the two lenses in the absorption detection which results in a magnification of 1.0 for an ideal alignment.

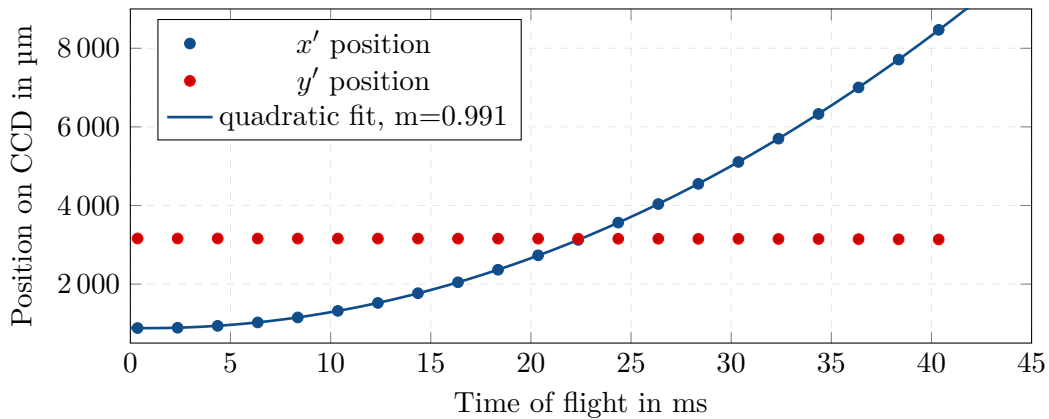


Figure 2.10: Measurement of the magnification of the absorption detection system. The distance of the center of the atomic cloud is shown in x' - and y' -direction depending on the time of flight of the ensemble. The constant value of the y' -position shows that gravity acts only in x' -direction.

2.2 Laser system

There are two distinct laser systems associated with the MAIUS-B apparatus. The *flight* laser system is developed and built in the collaborative groups of A. Peters, M. Krutzik and P. Windpassinger [Mih19]. The microintegrated laser diode modules are developed and fabricated in the group of A. Wicht [Kür20]. The flight laser system will be used in the actual sounding rocket missions MAIUS-2/3 and is briefly discussed in section 2.4.

To facilitate a parallel commissioning of the physics package, a flexible *ground-based* laser system has been built up independently. On a fundamental level, its layout and specifications are similar to the flight laser system. However, the actual implementation differs in many ways due to the different used optical components, a more simple approach for the actual diode lasers and a variant modular splitting. Additionally, it is larger than the flight system and not designed for space applications. The ground-based laser system has been utilized for the experiments within the scope of this thesis and shall be introduced in the following section. Its diligent development has been part of several master and bachelor projects [Fry17; Her17; Het15]. The reference modules for rubidium and potassium heritage from the QUANTUS-II experiment and were developed in [Bec09; Sch10].

2.2.1 Overview of ground-based laser system

An overview of the ground-based laser system is shown in fig. 2.11. It is based on a modular approach to the extent that closed modules contain functional groups which are linked to each other via optical fibers. There are four separate modules for each alkaline: i) the reference module providing the absolute frequency lock, ii) the external cavity laser diode (ECDL) module housing the actual lasers and their frequency stabilization, iii) and iv) the 2D-/3D-tapered amplifier (TA) modules¹ which amplify the laser light and distribute it to the respective fiber splitters. The modules are comprised of cuboid aluminum boxes of different sizes which are based on M3-threaded 10 x 10 mm optical breadboards. The small pitch in combination with solely used 10 mm or 1/2" optics allow for a compact volume of

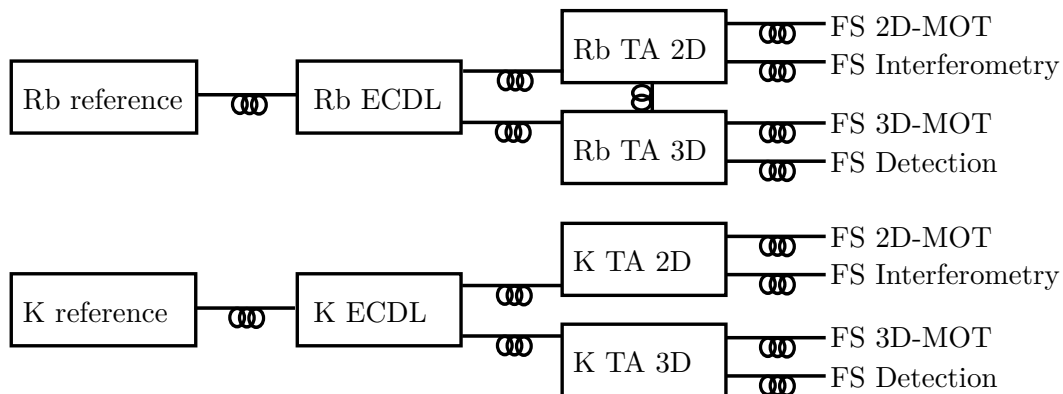


Figure 2.11: Overview of the modular ground-based laser system. Each module contains a closed subsystem with fiber inputs and outputs.

¹ Here, the prefixes 2D and 3D refer to the purpose of the amplified light for either 2D- or 3D-MOT light.

the modules. In fact, it is possible to fit the whole laser system into a transportable 19'' rack. This facilitates an easy transfer of the setup to other laboratories or institutions, if necessary. Furthermore, the fiber-based approach supports a flexible positioning of the apparatus. To give an example, the vacuum chamber can be rotated around its base plate (cf. fig. 2.1) to change the direction of gravity relative to the atoms without realigning any optics (section 4.6).

2.2.2 Laser system for manipulation of potassium atoms

The transitions relevant for laser cooling and Raman interferometry for the bosonic potassium isotopes ^{39}K and ^{41}K are shown in fig. 2.12. For standard Doppler-cooling [Phi98], the D2-transition $|S_{1/2}, F = 2\rangle \leftrightarrow |P_{3/2}, F' = 3\rangle$ at 766.701 nm is used. Due to the comparably small nuclear magnetic moment, the hyperfine splitting of the $P_{3/2}$ -manifold is only on the order of the linewidth $\Gamma = 6$ MHz of the D2-transitions. This inevitably leads to off-resonant excitation of atoms into $|P_{3/2}, F' = 2\rangle$ with a high rate compared to the cooling transition. Hence, they can decay into the dark ground state $|S_{1/2}, F = 1\rangle$. By using a second laser on the transitions $|S_{1/2}, F = 1\rangle \leftrightarrow |P_{3/2}, F' = 2\rangle$ these atoms re-enter the cooling cycle. Although referred to as the repumper laser, the second laser also acts as a cooling laser due to the high off-resonant excitation rate. Therefore, laser cooling of potassium and in particular of ^{41}K demands a flexible control over intensities and frequencies of both cooling lasers compared to laser cooling of ^{87}Rb .

As shown in fig. 2.13, the design of the laser system accounts for this by using four lasers, two used for cooling, trapping and detection within the science chamber and two for the 2D-MOT and interferometry.

The reference laser is locked to the $|S_{1/2}, F = 1/2\rangle \leftrightarrow |P_{3/2}, F' = 1/2\rangle$ crossover transition of ^{39}K using frequency modulation spectroscopy [Bjo83]. This transition is the most prominent feature in the spectroscopy signal of the vapor cell which contains potassium in natural abundance and is heated above 50 °C. To modulate and demodulate the frequency of the reference laser, the continuous diode current is mixed with a 6.25 MHz square-wave of the frequency controller electronics (cf. section 2.3.1). The reference laser light is overlapped in the ECDL-module with the light of three 767 nm lasers. The respective beat signals are detected on fast photodiodes, amplified and sent to the frequency control loops which stabilize the lasers on the desired frequencies.

The architecture of the home-built ECDL-lasers is based on the design originally presented in [Bai06]. They feature a compact design with all optical components glued within the aluminum housing. The external cavity has a lengths of 43 mm and Lorentzian linewidths (unstabilized) of down to 100 kHz have been measured [Her17]. To control the frequency of the laser light, the lengths of the cavity is controlled with a piezo element. This allows large frequency jumps up to some GHz within the mode hop free range. For fast frequency jumps and short-time stabilization, the diode current can be used as a second control variable if necessary.

By optical fibers the laser light is directed to the K-2D-TA and K-3D-TA modules where it is amplified to a power of up to 1 W, respectively. In the K-2D-TA module, the cooling and repumping light is overlapped and the resulting beat signal is detected with a photodiode. This offers the possibility to stabilize the frequency of the 2D-cool laser on the 2D-repumper

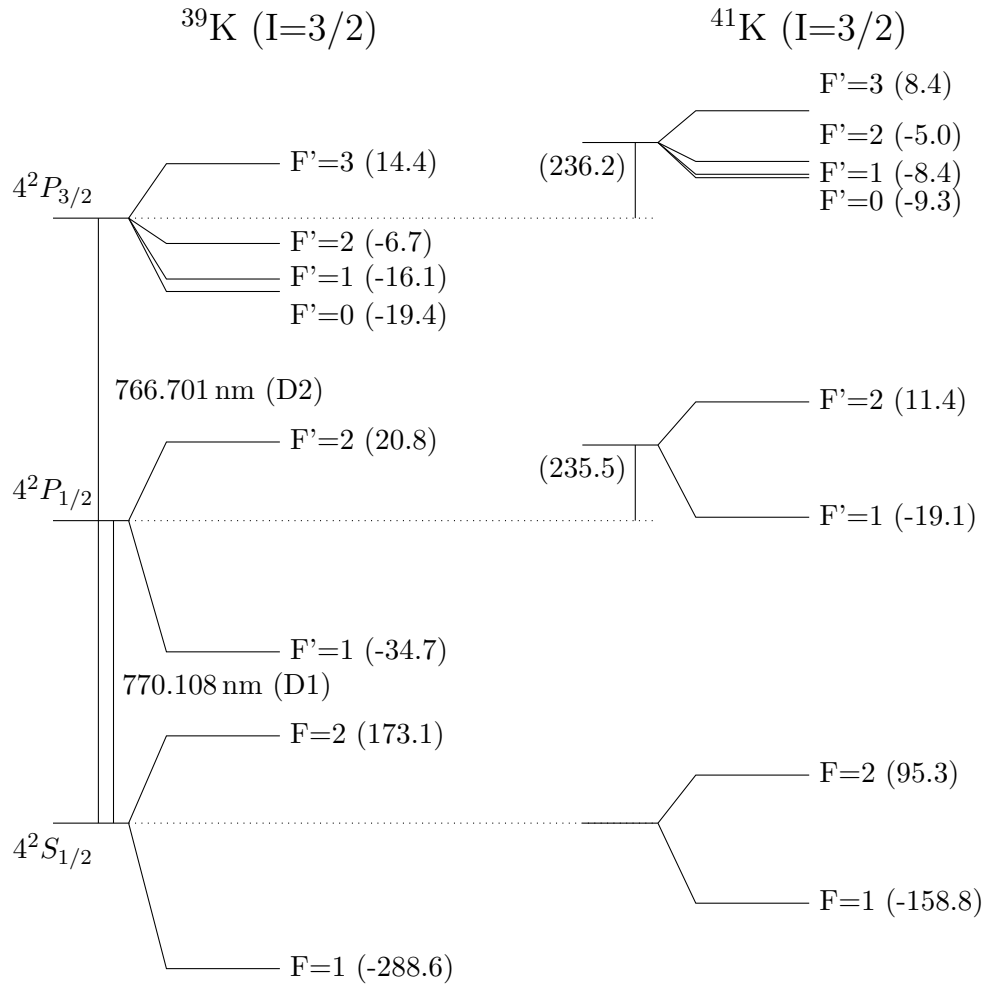


Figure 2.12: Level structure of the optical D1 and D2 transitions of ^{39}K (left) and ^{41}K (right). Values taken from [Tie19]. The values in brackets refer to the hyperfine level shifts in MHz.

laser using a digital phase-lock loop (PLL) which has been developed in [Pap17] for the flight laser system and tested for the first time in the here presented ground-based system. Once overlapped, the beams are split up and the first part is coupled into the 2D-fiber splitter (cf. 2.2.4) where it is distributed to the 2D-MOT collimators of the vacuum chamber. The second part passes an acousto-optical modulator (AOM, *Pegasus Optik, MT80-A1,5-IR*) which allows for a fast switching required by light pulses for atom interferometry. Afterwards, the light is coupled into the interferometry fiber splitter where it is delivered to the interferometry collimator (see fig. 2.3) once it is overlapped with the respective light fields for ^{87}Rb . To further reduce stray light in the optical fibers, shutters mounted on miniaturized stepping motors (*Faulhaber AM1020-V-3-16-01*) allow to fully cover the fiber collimators. They are controlled by the shutter electronics (cf. 2.3.1) and show a fast switching time of 1 ms with reaction times ranging from 3 ms to 6 ms, depending on

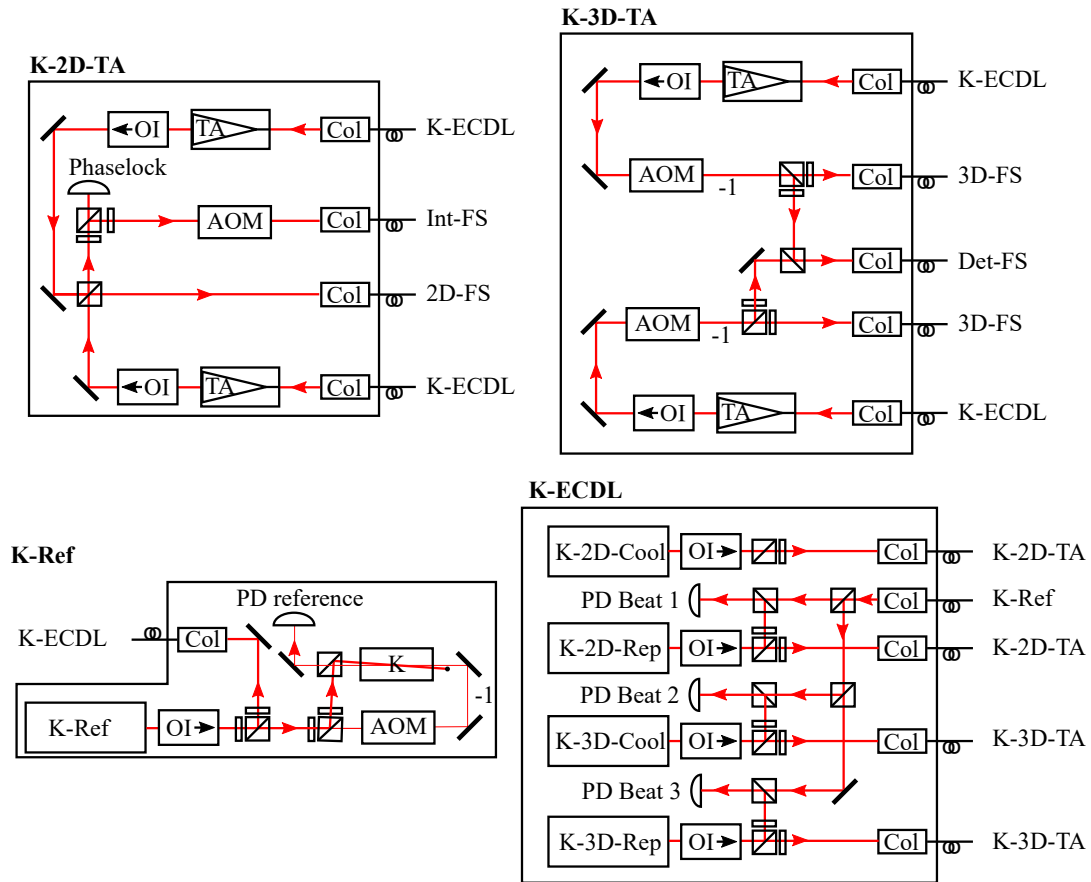


Figure 2.13: Laser system for manipulation of potassium atoms. The four modules are connected via optical fibers which is indicated at the respective fiber collimators (Col). The beam splitters are 50/50-splitters or polarizing beam splitters indicated with half-wave plates to tune the intensities. Mirrors used for coupling and polarizers for beam cleaning are omitted for clarity. OI: Optical Isolators, TA: Tapered Amplifier, AOM: Acousto-Optical Modulator, PD: Photodiode, K: Spectroscopy Cell, FS: Fiber Splitter.

their alignment. The reaction times, however, can be mitigated by triggering them right in advance in the timed experimental sequences.

In the K-3D-TA module, the amplified laser light for cooling and repumping is separately guided through two AOMs into the 3D-fiber splitter where it is combined with the light for rubidium and distributed to the science chamber. A smaller part of each frequency is branched off and overlapped in the middle of the module where it is subsequently coupled into the detection fiber splitter. By using two separate AOMs in this module, it is possible to control the intensities of the light fields independently during MOT and optical molasses phase as well as later for detection and optical pumping pulses. To prevent from coupling into the detection and 3D-MOT fiber splitters simultaneously, the AOMs are driven with two different frequencies (90 MHz and 70 MHz). This allows for fast switching between cooling and detection light. Mechanical shutters allow to block any residual light at all

fiber inputs.

2.2.3 Laser system for manipulation of rubidium atoms

The level structures of ^{85}Rb and ^{87}Rb are shown in fig. 2.14. In contrast to the bosonic isotopes of potassium, the spacing between the hyperfine states of ^{87}Rb is large enough to treat the cooling transition $|S_{1/2}, F = 2\rangle \leftrightarrow |P_{3/2}, F' = 3\rangle$ as an approximate two-level system. Still, there is a non-zero probability to excite atoms unintentionally into the $|P_{3/2}, F' = 2\rangle$ -state where they might decay to the dark state $|S_{1/2}, F = 1\rangle$. Therefore, also for laser cooling of ^{87}Rb a repumper laser is needed. However, the repumper laser does not contribute to the actual cooling as in the case of potassium. It is therefore sufficient to add repumper light with low intensity to the cooling light which keeps the ^{87}Rb atoms within the cooling cycle.

This has been taken into account for the design of the rubidium laser system which deploys only a single ECDL for repumping the atoms while having two separate ECDLs addressing the cooling transition. The reference module of the rubidium laser system (Rb-Ref) is structurally identical to the K-Ref module. The spectroscopic transition used for the rubidium reference lock is the crossover transition of ^{85}Rb which is located in the middle between the strong absorption lines $|S_{1/2}, F = 3\rangle \leftrightarrow |P_{3/2}, F' = 3/4\rangle$.

The light of the reference laser is overlapped with both cooling ECDLs in the ECDL-module and detected with a photodiode to offset-lock the cooling lasers to their respective transitions in ^{87}Rb .

The repumper laser is phase stabilized to the 2D-Cool laser in the Rb-2D-TA module after the two light fields are overlapped behind the TAs. As there is only a single ECDL for the repumper transition, the amplified repumper light is directed from the Rb-2D-TA module into the Rb-3D-TA module where it does not pass a further TA.

In the Rb-3D-TA module, to allow for a fast switching and intensity control of the repumper laser without shifting the laser frequency, two consecutive AOMs are needed which are adjusted to diffract into the +1st and -1st order which frequencies cancel. The remaining part of the Rb-3D-TA module, in particular the path of the 3D-cool and detection light, is identical to the K-3D-TA module.

2.2.4 Fiber splitter

The outputs of the Rb- and K-TA modules are connected via polarization maintaining (PM) fibers (*Corning PM85-U25D*) to the fiber splitters. Four different splitters at a design wavelength of 773.5 nm are used.

The 3D fiber splitter (*Evanescence Optics, S/N 7340-1, 4x4 Spliceless PM Coupler*) has four input and four output ports. The input ports are connected with the two corresponding fiber collimators of the Rb- and K-3D-TA modules. In the fiber splitter, the laser frequencies for cooling and repumping of rubidium and potassium are mixed and distributed to the four MOT collimators at the experimental chamber. The distribution ratio of the fiber splitter has been measured to $(25 \pm 2)\%$ for both wavelengths.

The 2D fiber splitter (*Evanescence Optics, S/N 7340-4, 2x4 Array*) has two inputs, each one connected to the Rb- and K-2D-MOT output collimators. It features four output ports with a nominal splitting ratio of 49-45-5-1. The two high power output ports are

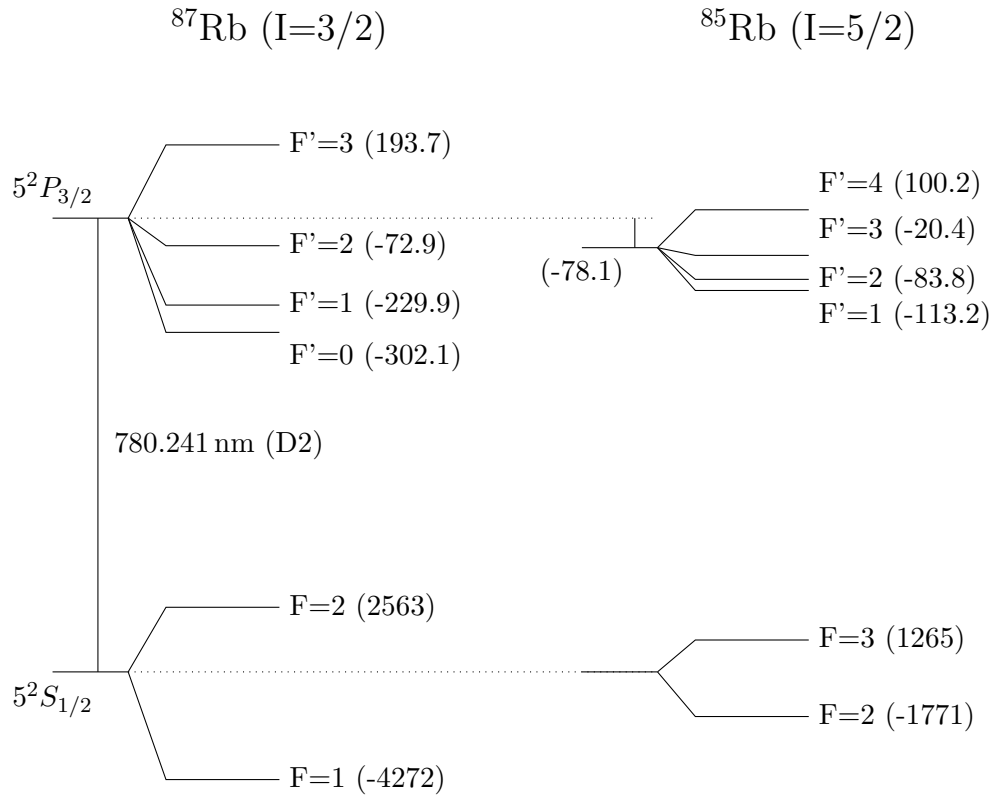


Figure 2.14: Level structure of the D2 transitions of ^{87}Rb (left) and ^{85}Rb (right). Values taken from [Ste01; Ste10]. The values in brackets refer to the hyperfine level shifts in MHz.

connected to the transversal beam expanders of the 2D-MOT. The 5% output delivers the pusher light and the 1% output has intentionally been added for a further retarder collimator to allow for a longitudinal molasses configuration. However, it turned out to be advantageous to deploy only the pusher collimator when working with ^{87}Rb and ^{41}K simultaneously. Thus, the remaining port is utilized for monitoring purposes.

The detection fiber splitter (*Evanescent Optics, S/N 7340-3, 954P Fixed Ratio Coupler*) is a 2x2-splitter and combines the corresponding output ports of the Rb- and K-3D-TA modules. One of the output fibers is connected to the detection collimator (see fig. 2.3) at the experimental chamber. The other output is used for monitoring and fiber coupling.

The interferometry fiber splitter uses the same type of 2x2-splitter. It is connected to the interferometry outputs of the Rb- and K-2D-TA modules. The outgoing fiber is connected to the interferometry collimator at the experimental chamber. The remaining output may be used for monitoring and fiber coupling but also offers the option to replace the retroreflecting mirror by a second collimator.

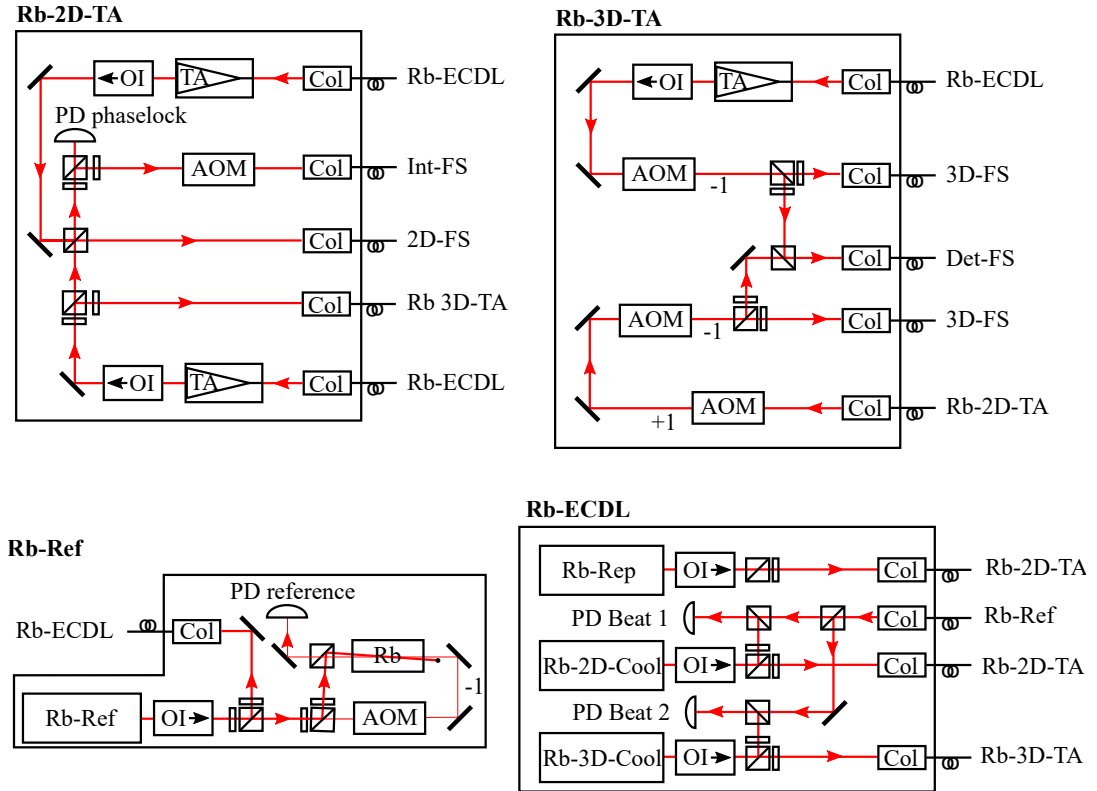


Figure 2.15: Laser system for manipulation of ^{87}Rb . The four modules are connected via optical fibers which is indicated at the respective fiber collimators (Col). The beam splitters are 50/50-splitters or polarizing beam splitters indicated with half-wave plates to tune the intensities. Mirrors used for coupling and polarizers for beam cleaning are omitted for clarity. OI: Optical Isolators, TA: Tapered Amplifier, AOM: Acousto-Optical Modulator, PD: Photodiode, Rb: Spectroscopy Cell, FS: Fiber Splitter, Det: Detection.

2.3 Control system

The control system of the ground-based MAIUS-B apparatus comprises all hardware and software components which are required to operate the laser system and to control the electronic parts of the experimental chamber such as the atom chip, coils and sensors of different kinds.

The overall structure of the ground-based control system is shown in fig. 2.16. It is based upon the modular electronic platform TBus which has already been used in various transportable experiments with miniaturized control electronics such as QUANTUS-1, QUANTUS-2 or MAIUS-A, to mention only a few. In the following section, the different parts of the ground control system including the TBus system, current drivers, temperature control of the laser system and the software environment are introduced.

2.3.1 TBus system

The basic infrastructure of the utilized TBus standard with a focus on the card design and software interface is described in [Pop18]. Its distinctive features are compact electronic

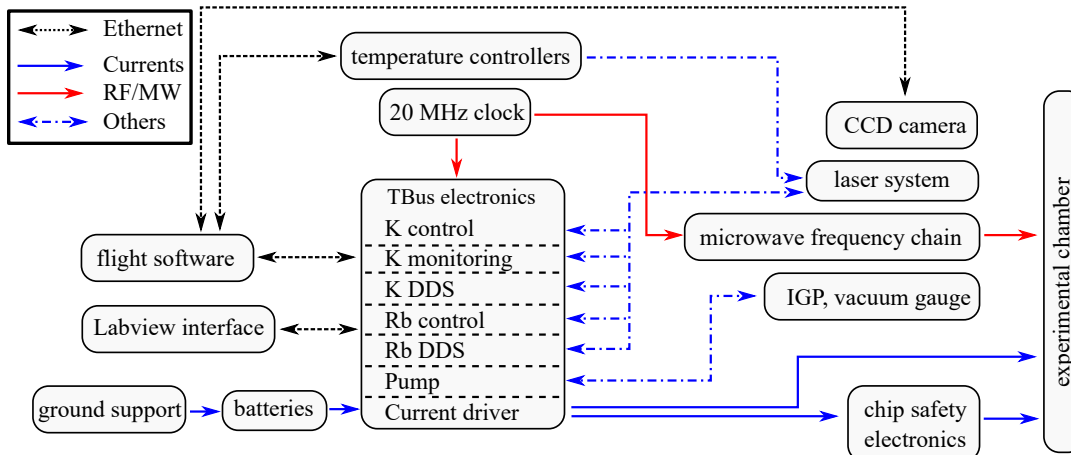


Figure 2.16: Overview of the ground-based experimental control system and its internal communication. Details on the microwave frequency chain are given in fig. 3.5.

boards in PC/104 form factor which are stacked above each other. The whole experiment uses seven different stacks which are all mutually connected via a common trigger line and a 20 MHz clock. The reference oscillator (*Abracon AOCJY-20MHZ-E*) has a nominal frequency stability of ± 100 ppb on an annual basis.

Every TBus stack contains a power supply card which provides the other cards with the voltages necessary for operation ($+3.3$ V, ± 6.6 V, ± 15 V, ± 20 V). Ultimately, the electrical power is supplied by power adapters but might be changed to batteries in future to reduce 50 Hz noise from the power line. Further, each stack contains an Ethernet interface to communicate with the control computer, to convert the external frequency reference to the bus clock (10 MHz or 24 MHz) and to manage the trigger lines of the respective stack. The other functions of the stacks are listed below.

- The *K control* stack contains the current drivers needed to operate the ECDLs of the potassium laser system. It further controls the piezo actuators of the potassium ECDLs in a control loop to realize spectroscopy, offset and phase locks.
- The *K monitoring* stack contains two high power current drivers to drive two TAs of the potassium laser system. It also offers 24 channels for temperature and photodiode monitoring. The negative temperature coefficient (NTC) sensors are distributed throughout the experimental chamber and record the temperatures of the magnetic coils, the chip holder and the sublimation pumps among other positions of interest. The photodiodes are glued into the collimators and allow to measure the stray light within the collimator tube. A dedicated card for analogue voltage outputs in the range of -10 V to 10 V allows to control external instruments such as analogue power supplies, switches or function generators.
- The *K DDS* stack controls the frequency and intensity of the radiofrequencies used to feed the AOMs in the potassium laser system. All frequencies are bandpass filtered and subsequently amplified to 1 W or 2 W by radiofrequency power amplifiers

(*AMPA-B-30/AMPA-B-34*). Further cards control the ten shutters used in the whole laser system and deliver the voltages for the fans to air-cool the control system. Two additional TA current drivers for the potassium system are as well included in this stack.

- The *Rb control stack* contains the current drivers and frequency controllers for the rubidium lasers.
- The *Rb DDS stack* controls the five AOMs of the rubidium laser system. One output is connected to the microwave frequency chain which delivers the frequencies needed for evaporative cooling of rubidium. It is described in section 3.2 in more detail. Three further cards power the TAs of the rubidium laser system.
- The *Pump stack* contains a high voltage section which delivers 5 kV to the ion getter pump. It further reads out the pressure sensor on the vacuum chamber. The pump stack sits on the base plate of the physics package and is part of the flight hardware.
- The *Current driver stack* contains the low-noise current drivers for the coils and atom chip structures and is described in the following section in more detail.

Thus, the TBus system controls all key components of the ground-based system which allows a complete remote operation of the experiment.

2.3.2 Current drivers and batteries

The low noise coil and chip current drivers heritage from the MAIUS-A system and are discussed and characterized in [Pop18]. A further characterization of the current noise and its influence on the lifetime of the trapped ensembles is part of the thesis of Wolfgang Bartosch [Bar21].

The chip current drivers control the currents delivered by pairs of two lithium ferrophosphate (LiFePO_4)-battery cells with 3.2 V nominal voltage (*A123 26650M1B*) which are galvanically isolated from the rest of the electronics. In particular, the current drivers are electrically isolated from each other which is explicitly necessary when working with galvanically connected atom chip structures. The battery packs are loaded with the ground support electronics which comprise several power supplies controlled remotely via a LabView[®] virtual instrument (VI). During the experimental cycles, the batteries can either be remotely disconnected from the power supplies or work in a buffered mode. The latter mode is utilized for most of the sequences up to single component BEC generation. For more involved sequences including dual-species BEC generation, magnetic lensing and magnetic transport the batteries are galvanically isolated from the power supplies. This results in a significantly higher shot-to-shot stability which mainly stems from a reduction of noise from the power line.

All currents delivered to the chip structures pass a chip safety board which contains a combination of current sensors and conventional ultra rapid fuses which trigger at 8.5 A for the Mesoscopic structures, at 5.0 A for the Base-Z structure and at 2.0 A for the Science-Z structure.

The coil current drivers are designed to control high inductive loads such as the x-, y-, z- and 2D-MOT coils. They control the currents delivered by a high power 9.6 V three-cell

battery pack (*Headway 40152SE*) which can also be used in isolated or buffered mode. In contrast to the flight system, the ground-based control system allows to control the coils of the 2D-MOT independently by driving the current outputs of analogue power supplies.

2.3.3 Calibration and characterization of current drivers

To provide an absolute calibration of the output currents of the chip and coil current drivers, they were tested and calibrated with reference measurements. The setup for the measurements is shown in fig. 2.17. A constant current I_0 is requested from the current driver and sent through a test structure. In case of the chip current drivers, a $R_{\text{ref}} = 1\ \Omega$ reference resistor (*Isabellenhuetten WID.RTO 50W 1R0*) fixed on a heat sink is utilized as a test object. For the coil current drivers, the actual coil with its respective inductance $L_{x,y,z}$ and resistance $R_{x,y,z}$ is connected to the current driver. After a settling time of 1 s, the measurement of the voltage V between the structure is triggered. Subsequently, the resistance $R_{x,y,z}$ is measured using a triggered 4-point probe to compensate for the resistance of the measurement wire. Since the coil resistance changes with temperature, special care has been taken to repeat the voltage and resistance measurements in the same temporal order. The measurements are carried out using an *Agilent 34461A* precision multimeter which suggests a relative uncertainty of $\Delta I/I < 0.02\%$ using Gaussian error propagation. The deviations of the inferred current from the requested are exemplarily depicted in fig. 2.18 and show a nearly constant slope. Thus, to compensate for the deviations, they are fitted linearly and the requested currents are corrected by the respective offsets and slopes of the fits. The relative deviation of the delivered currents after the correction is $\Delta I/I < 0.2\%$ for the y-coil over the whole examined range. Typical deviations are expected to be smaller since only negative currents are employed in the experimental sequences. The currents through the Science-Z are known to an accuracy of $\Delta I/I < 0.05\%$.

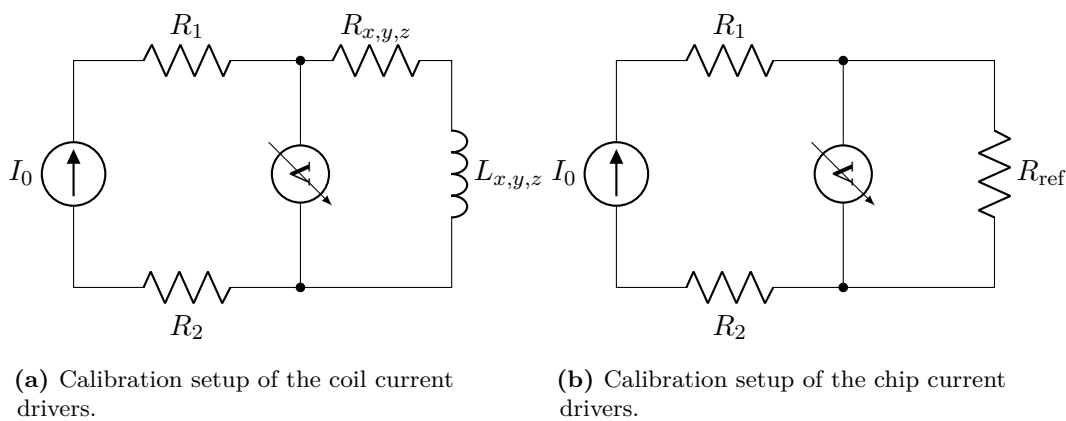


Figure 2.17: Measurement of the currents through the coils (a) and chip structures (b). $R_{1,2}$ denote the equivalent circuits of the cables in the measurement setup. $R_{x,y,z}$ and $L_{x,y,z}$ label the equivalent circuit of the coils and R_{ref} the reference resistor of $1\ \Omega$.

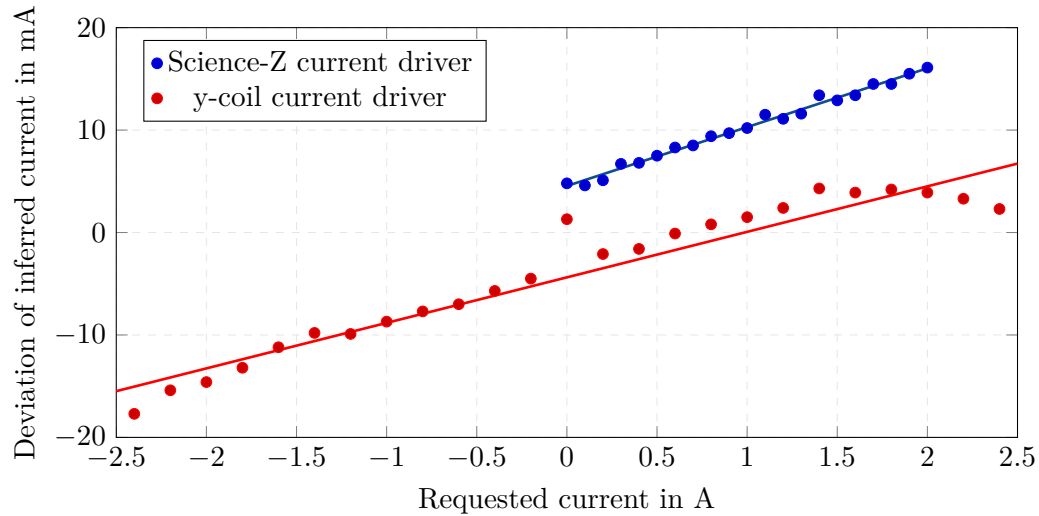


Figure 2.18: Comparison of the inferred current with the requested current of the y-coil and Science-Z structure. The results of the linear correction are fed to the calibration.

2.3.4 Temperature control

The operation of frequency stabilized ECDL lasers requires a reliable and stable temperature control. In each ECDL, two $10\text{ k}\Omega$ NTC resistors are integrated to measure the temperature of the laser diode and the housing, respectively. They are stabilized with an instability below 1 mK in a control loop using commercial temperature controllers (*Meerstetter TEC-1091*) which adjust the currents through Peltier elements connected to the housing. Similarly, the TAs are temperature stabilized using a single $10\text{ k}\Omega$ NTC resistor in combination with a Peltier element. All 25 temperature controllers are accessible with a control computer via an XPort Serial-To-Ethernet Module. To change the temperature of an ECDL the supplied firmware is used, however it is also possible to adjust and read out the temperatures with the flight software.

2.3.5 Software

The software of the MAIUS-B ground-based system undertakes the control of all digital electronics. It is based on three pillars, the laboratory control environment, the experiment control software (ECS) and the experiment design tools (EDT) which are briefly introduced in the following.

The LabView based laboratory control environment allows to communicate with all TBus stacks via Ethernet. It is predominantly used for initial configuration and frequency stabilization of the laser system. Thus, in the graphical user interface (GUI) the ECDL and TA currents can be switched and adjusted, the FMS of the reference lasers and the offset frequency locks of the other lasers are implemented. Further, the settings for the digital control loops (PID-parameters) of the frequency stabilization are stored in the laboratory control environment. Due to the convenient GUI and access to all hardware parameters it is also used for debugging in case of a software failure or when new components are added

to the system.

The ECS is developed at the Institut für Softwaretechnologie, Deutsches Zentrum für Luft- und Raumfahrt (DLR), and the foundation of its architecture lies in the MAIUS-1 mission where it was implemented as the on-board software [Wep18]. It communicates with the experimental hardware and uses a modular approach for the hardware implementation. To describe the various TBus cards and their possible control parameters, a domain-specific language (DSL) is used which summarizes the specifications in a `.card` file. A second DSL summarizes the TBus cards in a `.stack` file which allows to assign stack specific trigger channels, clock rates and default values for various output channels. The described experimental hardware is translated into C++ code once the *Makefile* is processed by the *Make* build automation tool. The experimental sequences are described with specific sequence (`.seq`) files which summarize time-ordered subsequences (`.subseq`) files. The sequence and subsequence DSLs are interpreted by the ECS. The highest level of sequence description is represented by a *sequence graph* which encompasses several sequences and allows to introduce control structures like multi-dimensional scans and conditional execution depending on the outcome of previous sequences. The sequence graph permits to automate daily routine scans like the characterization of the system performance. Its main purpose, however, is the description of the specific mission program of a single flight. It is arranged as a decision tree and therefore allows autonomous operation including self-optimization. The EDT include a number of Python based GUIs which act at the interface between the experimentalist and the ECS. Most importantly, it contains the sequence editor which allows to create and execute sequences. A data proxy tool collects and stores all monitoring data in a database which are subsequently being plotted in an open-source browser based chart tool (*Grafana*). A further tool implements machine learning algorithms based on a Gaussian modelling process [Ras06] or differential evolution [Gei13] which are comprised in the open MLOO-algorithm (*Machine-Learner Online Optimization*, [Wig16]). These learners are nowadays routinely used in cold atom experiments to self-optimize experimental sequences incorporating many parameters which make multidimensional scans unfeasible. Most of the tools which are part of the EDT have been continuously developed and advanced by Hauke Müntinga at the Zentrum für angewandte Raumfahrttechnologie und Mikrogravitation (ZARM) in Bremen.

2.4 Flight system

In the following section, a brief overview of the MAIUS-B payload is given. Furthermore, a short discussion of the flight electronics and laser system will reveal the similarities and differences to the ground-based system. For a more detailed discussion see [Bar21].

The MAIUS-B payload is shown in fig. 2.19. It consists of five modules on top of a two-stage VSB-30 sounding rocket motor. These are (from top to bottom) general electronics, physics package, laser system, laser electronics and the battery module. This order has been chosen to shift the payload center-of-mass as close to the atoms as possible which minimizes the effects of residual payload rotations Ω on the outcome of matter wave interferometry experiments. These include:

- Rotation components Ω_{\parallel} parallel to the interferometry axis lead to a position shift

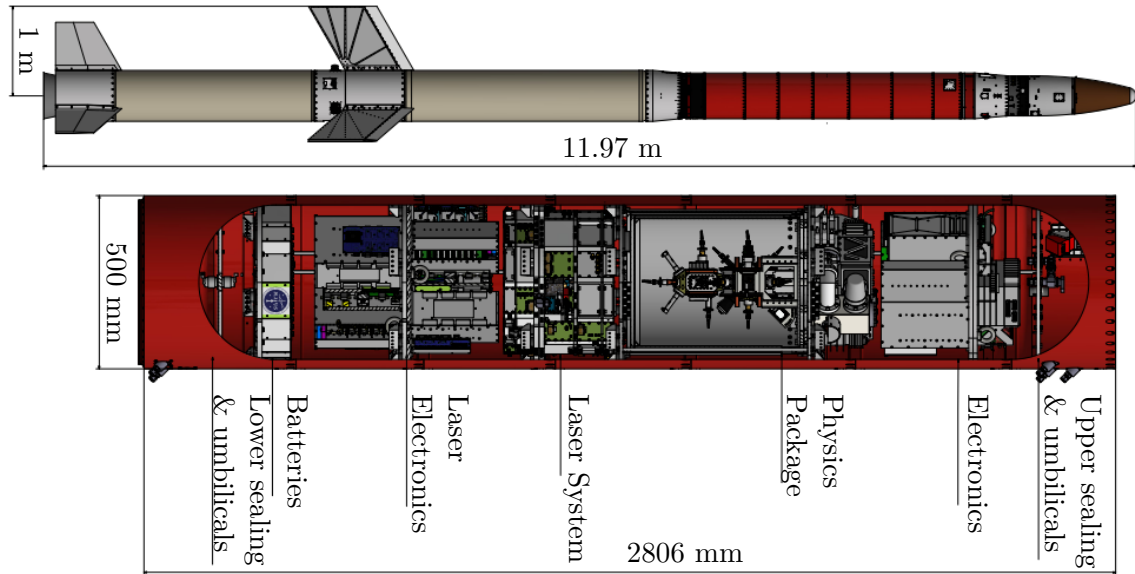


Figure 2.19: CAD drawing of the scientific payload (in red) MAIUS-B on the two-staged VSB-30 motor. Figure taken from [Els20].

Δ_r of the atom cloud radially along the interferometry beam according to $\Delta_r = R \sin \Omega_{\parallel} T \approx R \Omega_{\parallel} T$ for $\Omega_{\parallel} T \ll 1$ between two light pulses resulting from geometric considerations. Here, R denotes the distance between the interferometry axis and the center-of-mass of the payload and T the pulse separation time. Since the interferometry beam has a Gaussian intensity profile, the duration of an optimal $\pi/2$ - or π -pulses is changed accordingly. In principle, this can be counteracted if the center-of-mass position and the rotation vector are precisely known. The maximum rotation rate of the rocket is kept below $0.05^\circ/\text{s}$ by the position control system of the rocket. Thus, a displacement of the payload center-of-mass 20 cm away from the atoms would lead to a maximum shift of $174 \mu\text{m}$ after 1 s.

- Rotation components Ω_{\perp} vertical to the interferometry axis induce a Coriolis phase $\Delta\Phi_C$ which adds to the phase evolution of the atoms during the interferometer [Dic13; Hog08; Len97]. To first order, this phase shift is given by $\Delta\Phi_C = k_{\text{eff}} R \Omega_{\perp}^2 T^2$ with the effective wave number k_{eff} . Notably, this effect is *not* cancelled in a differential measurement using ^{41}K and ^{87}Rb due to their difference in k_{eff} .
- If the condensates do not overlap perfectly at the last beam splitter in a Mach-Zehnder interferometer due to rotations of the effective wave vector between the pulses, the wave nature of the condensates induce a spatial interference pattern with a fringe period according to the de-Broglie wavelength of the *relative* motion of the two ensembles [And97].

The payload is sealed at the top and bottom hull segments with sealing plates to guarantee a constant air pressure during flight. In contrast to the air-conditioned laboratory environ-

ment, the system in flight configuration is exposed to additional heat loads due to friction of the hull with the atmosphere during launch and reentry. Furthermore, neither air nor water cooling is applicable during flight. This leads to the necessity of minimal thermal contact between the payload and the hull segments. To buffer the internally produced heat, the high power consuming modules and components such as radiofrequency amplifiers are fixed on bulk aluminum plates acting as heat sinks. Further details on the cooling concept of the payload and a discussion of thermal simulations can be found in [Els21; Els20].

The flight laser system consists of four ECDLs running at 767.7 nm for the manipulation of potassium atoms, three ECDLs at 780.2 nm for the manipulation rubidium atoms and one ECDL at 1064 nm which offers the implementation of an optical dipole trap. These are set up in master-oscillator-power-amplifier configurations integrated on micro-optical benches made of aluminum nitride (AlN) ceramic substrates [Kür20]. Two additional distributed feedback (DFB) diode lasers act as reference lasers [Mih19] to stabilize the ECDLs on their respective frequencies.

The amplified laser light is fiber-coupled into five compact optical benches made of Zerodur[®] featuring optical isolators, AOMs and shutters. Similar to the ground-based laser system, the amplified light is overlapped in fiber splitters. The laser light used for interferometry and the 2D-MOT is overlapped directly after the ECDLs where it is phase locked.

The laser electronics module, batteries and general electronics represent the control system of the payload. In contrast to the laboratory system, all electronics and lasers run in battery mode which requires a highly resilient battery system. In return, the flight system benefits from the decoupling to electrical noise stemming from the power line. The laser electronics and general electronics show many similarities to the ground system as they are based on the TBus system as well. Although the internal compositions of the different TBus stacks differ from the ground-based system, the underlying concepts remain the same.

A major improvement of the flight electronics is given by a more flexible control of the 6.8 GHz and 254 MHz microwave sources which are needed for evaporation or state preparation of atomic ensembles and will allow species selective internal state manipulation techniques such as microwave stimulated Raman adiabatic passage (STIRAP) [Dup15]. Additionally, capabilities for laser power stabilization are provided which are not present in the ground system. This will improve the long term stability of the experimental performance and thus reduce time consuming sequence optimization.

The flight system features an updated version of the chip- and coil current drivers and a chip safety board which offers additional high resolution measurements of the currents and voltages with a bandwidth up to the kHz regime. A parallel temperature measurement of the output circuit of the current drivers will enable a feedback loop to correct for temperature drifts during operation. In the predecessor experiment MAIUS-A, these temperature drifts were identified as a major source for drifts of the bottom potential of the magnetic trap during evaporative cooling which resulted in a shift of the condensate fraction and the trap position [Pop18].

Since the communication of the flight and ground-based systems deploy the same software and communication protocols, it is possible to transform the experimental sequences from the ground system to the flight system with only minor modifications.

CHAPTER 3

Generation of quantum degenerate mixtures of ^{87}Rb and ^{41}K

The generation of ultracold ensembles of ^{87}Rb on atom chips is a well established technique and has been demonstrated in several preceding experiments [Hän01; Ott01; Rou08; Rud15]. Conventionally, the atoms are prepared in a (chip-) MOT, further cooled down in an optical molasses and subsequently loaded into a magnetic trap generated by a z-shaped structure on the atom chip in combination with external bias fields. Afterwards, the phase space density (PSD) of the ensemble is increased by radiofrequency evaporation until quantum degeneracy is reached. Detailed manuals for this procedure on similar atom chip setups can be found in [Her13; Rud16; Sah19; Sei14]. However, by adding ^{41}K as a second species, this approach can not be applied anymore since the radiofrequency field would be simultaneously resonant with Zeeman transitions of both species. Since the trapped ^{41}K atoms are typically outnumbered by ^{87}Rb atoms by up to three orders of magnitude, this would hinder the phase transition in ^{41}K .

One widely employed method to reach Bose-Einstein condensation for both species is to utilize sympathetic cooling. Here, the most energetic ^{87}Rb atoms are removed from the magnetic trap using the microwave transition at 6.8 GHz between $F=2$ and $F=1$. Due to interspecies elastic collisions, the ^{41}K atoms are cooled sympathetically while keeping their atom number nearly constant [Bur18; Ell18; Mod01].

In the following section, we present the generation of quantum degenerate ^{41}K - ^{87}Rb mixtures with high repetition rate and controllable particle number ratios. After a brief discussion of the experimental performance for cooling and trapping of ^{41}K and ^{87}Rb , a focus is put on the microwave evaporation of ^{87}Rb and detailed analysis of sympathetic cooling of ^{41}K .

3.1 Cooling and trapping of mixtures

The efficient preparation of magnetically trapped ^{41}K and ^{87}Rb with high PSDs is pivotal for the generation of BEC mixtures. Since we follow a sympathetic cooling approach in this work, the optimization of the MOT and molasses sequences has been done in favor of the buffer gas ^{87}Rb . In turn, the here presented performance results do not reflect the optimal conditions for cooling and trapping of single species ^{41}K . With slightly adjusted parameters, we reach higher PSDs for ^{41}K , albeit at the cost of ^{87}Rb .

3.1.1 Chip-MOT and molasses

We start an experimental cycle by loading of a 3D-MOT with cold atomic beams of ^{87}Rb and ^{41}K from the 2D-MOT. In fig. 3.1, the separate and simultaneous loading of the 3D-MOTs of ^{41}K and ^{87}Rb is shown in comparison. It is clearly visible, that the loading

rate and the saturation value of the ^{87}Rb MOT surpasses the ^{41}K MOT by roughly an order of magnitude. Due to the higher loading rate of the ^{87}Rb MOT, saturation is reached after less than 1 s with an atom number of $9 \cdot 10^8$ atoms. The ^{41}K MOT reaches an atom number of $1.4 \cdot 10^8$ atoms after a loading time of 1 s. If both MOTs are loaded simultaneously, we observe a typical drop of trapped ^{41}K -atoms by a factor of 0.7 which we attribute to light-assisted heteronuclear collisions and subsequent escape from the MOT. The loss occurs only for the ^{41}K -atoms while the ^{87}Rb MOT is unaffected. Similar observations have also been reported for mixed MOTs with ^{40}K - ^{87}Rb [Gol02] and ^{39}K - ^{85}Rb [Mar00b]. After initial loading of the MOTs, we switch off the 2D-MOT laser light and shift the trap minimum towards the chip by ramping the current through the Mesoscopic-U structure from 7.0 A to 5.9 A and the y-coil from -0.36 A to -0.89 A. This step ensures a better mode match of the ^{87}Rb atom ensembles with the following magnetic trap¹. Afterwards, the atoms are released from the MOT by switching off the cooling lasers and the chip structures. We cancel residual magnetic fields at the position of the atoms by applying small compensation currents in the external coils of $I_{x,y,z} = (0.12 \text{ A}, -0.018 \text{ A}, -0.06 \text{ A})$. In the following 5.5 ms, both ensembles are further cooled by different sub-Doppler cooling protocols. The ^{87}Rb atoms are cooled down to temperatures of $15 \mu\text{K}$ by switching the cooling light to a detuning of $\delta = -114 \text{ MHz}$ and ramping down its peak intensity from

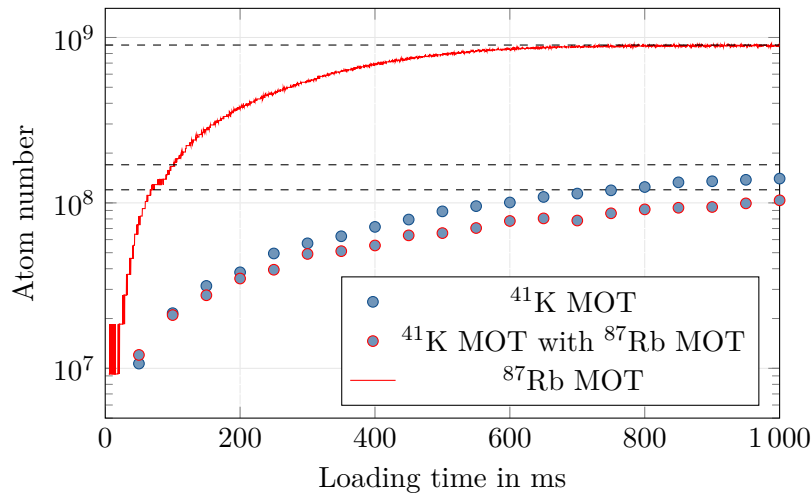


Figure 3.1: Loading of single and mixed ^{41}K and ^{87}Rb MOTs. The atoms released from the ^{41}K MOT are detected via absorption imaging. Since the size of the ^{87}Rb MOT exceeds the detection area of the CCD chip, the atom number of ^{87}Rb is derived from an in-situ measurement of its fluorescence. The ^{41}K MOT saturates at $1.7 \cdot 10^8$, the ^{87}Rb MOT at $9.0 \cdot 10^8$ atoms. The mixed ^{41}K MOT shows a drop of 30% in particle number and saturates at $1.2 \cdot 10^8$ atoms.

¹ If the trap is compressed simultaneously by increasing the Mesoscopic-U current, it is possible to enhance the ^{41}K PSD and allow to trap more ^{41}K in the magnetic trap - by cost of ^{87}Rb . This technique is also used by other experiments [Kis09] but has not been progressed in the here-described approach which is based on an optimal ^{87}Rb performance.

36 mW/cm² to zero. Here, δ denotes the detuning of the cooling light to the resonant cooling transition $|F = 2\rangle \leftrightarrow |F' = 3\rangle$.

By applying the same approach for ⁴¹K, no sub-Doppler cooling would be observed since the neighboring atomic levels in the vicinity of the cooling transition (cf. fig 2.12) lead to additional heating forces for large detunings. Instead, we follow the sub-Doppler cooling procedure described in [Lan11]. Thus, the detuning of the cooling light is ramped from $\delta = -3$ MHz to $\delta = -8$ MHz. Thanks to a natural depumping of atoms into the $F=1$ groundstate, the ⁴¹K repumping laser can be utilized to control the amount of atoms in the cooling cycle and reduce the heating due to photon reabsorption [Coo94]. This works most efficiently for very low repumping intensities around $I_{\text{rp}} \approx 1/100 I_{\text{cool}}$ with the cooling laser intensity I_{cool} and a repumper frequency resonant to the transition $|F = 1\rangle \leftrightarrow |F' = 2\rangle$. Using this approach, we reach ⁴¹K temperatures of 78 μ K which is below the Doppler temperature $T_{\text{D}} = \frac{\hbar\Gamma}{2k_{\text{B}}} = 144 \mu\text{K}$ with the Planck constant \hbar , Boltzmann constant k_{B} and the natural linewidth $\Gamma = 2\pi \cdot 6$ MHz of the cooling transition [Tie19].

3.1.2 Magnetic trapping

After optical molasses, we trigger two light pulses for 0.9 ms resonant to the $|F = 2\rangle \leftrightarrow |F' = 2\rangle$ transitions of ⁴¹K and ⁸⁷Rb using the detection collimator to pump the atoms into the stretched state $|F = 2, m_F = 2\rangle$ which is suitable for magnetic trapping. During optical pumping, we apply a bias magnetic bias field of 4.9 G along the direction of the pumping beam to maintain only σ^+ -transitions until the atoms accumulate in the target state $|F = 2, m_F = 2\rangle$.

Following the approach discussed in [Her13], we initiate the magnetic trap by applying

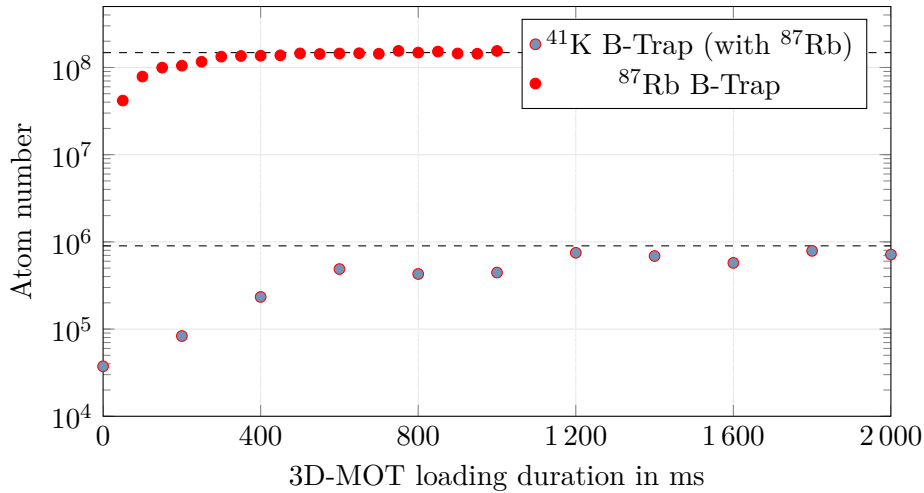


Figure 3.2: Atom numbers of mixed ⁸⁷Rb and ⁴¹K ensembles in the magnetic trap for different 3D-MOT loading durations. Saturation is reached for $1.48 \cdot 10^8$ ⁸⁷Rb atoms and $0.9 \cdot 10^6$ ⁴¹K atoms. The ensembles are detected after a holding time of 150 ms in the magnetic trap via absorption imaging. During this time, both ensembles experience a fast decay in atom number due to atoms spilling over the trap barrier and inelastic collisions in the case of ⁴¹K (see also chapter 3.3.1).

8.9 A through the Mesoscopic-H and 5.12 A through the Base-Z structure (cf. fig. 2.6). In combination with an external bias field in y-direction of -16.6 G, the resulting field forms a large volume magnetic trap with a geometric mean trapping frequency of $\bar{\omega}_{\text{Rb}} = 2\pi \cdot 40.3 \text{ Hz}$ for ^{87}Rb ($\bar{\omega}_{\text{K}} = 2\pi \cdot 59.6 \text{ Hz}$ for ^{41}K)¹. During evaporation, higher frequencies are desirable to enhance the collision rate between the atoms which leads to a faster thermalization. To achieve this, we move the minimum of the initial trap closer to the atom chip by ramping down the currents through the Mesoscopic structures to zero and simultaneously ramping up the current in the Science-Z structure to 2.0 A and the y-coils to -2.0 A. The duration of this ramp is optimized to 18.5 ms in order to trap as many ^{87}Rb and ^{41}K atoms as possible in the target magnetic trap. To minimize the loss rate in this trap due to Majorana spin-flips [Bri06], we add a further magnetic field in x-direction of -1.3 G in order to lift the trap bottom to a non-zero magnetic field. The loading curves of this magnetic trap for ^{41}K and ^{87}Rb after a holding time of 150 ms are shown in fig. 3.2. The cigar shaped target Ioffe-Pritchard type trap features trapping frequencies of $\omega_{x',y',z',\text{Rb}} = 2\pi \cdot (23, 908, 911) \text{ Hz}$ for ^{87}Rb and $\omega_{x',y',z',\text{K}} = 2\pi \cdot (33, 1324, 1329) \text{ Hz}$ for ^{41}K . The directions (x',y',z') refer to the respective eigenfrequencies after diagonalization of the Hessian matrix of the trapping potential. Since the Base-Z and Science-Z structures are inherently non-axisymmetric, the eigenaxes (x',y',z') do not match the chip coordinate system (x,y,z) exactly even without gravity. The trapping potentials for ^{87}Rb and ^{41}K along the eigenaxes are shown in fig. 3.3. Thanks to the same magnetic coupling strengths of ^{41}K and ^{87}Rb , the curves almost overlap. Due to the higher mass of ^{87}Rb , its potential curve lies below the ^{41}K potential. Consequently, both curves perfectly match in microgravity.

1 The different trap frequencies for ^{87}Rb and ^{41}K ω_{Rb} and ω_{K} can be converted into each other by using the relation $\omega_{\text{Rb}} = \sqrt{m_{\text{K}}/m_{\text{Rb}}}\omega_{\text{K}}$ with the isotope masses m_{K} and m_{Rb} . In presence of gravity, this relation is just an approximation due to the different position of the traps.

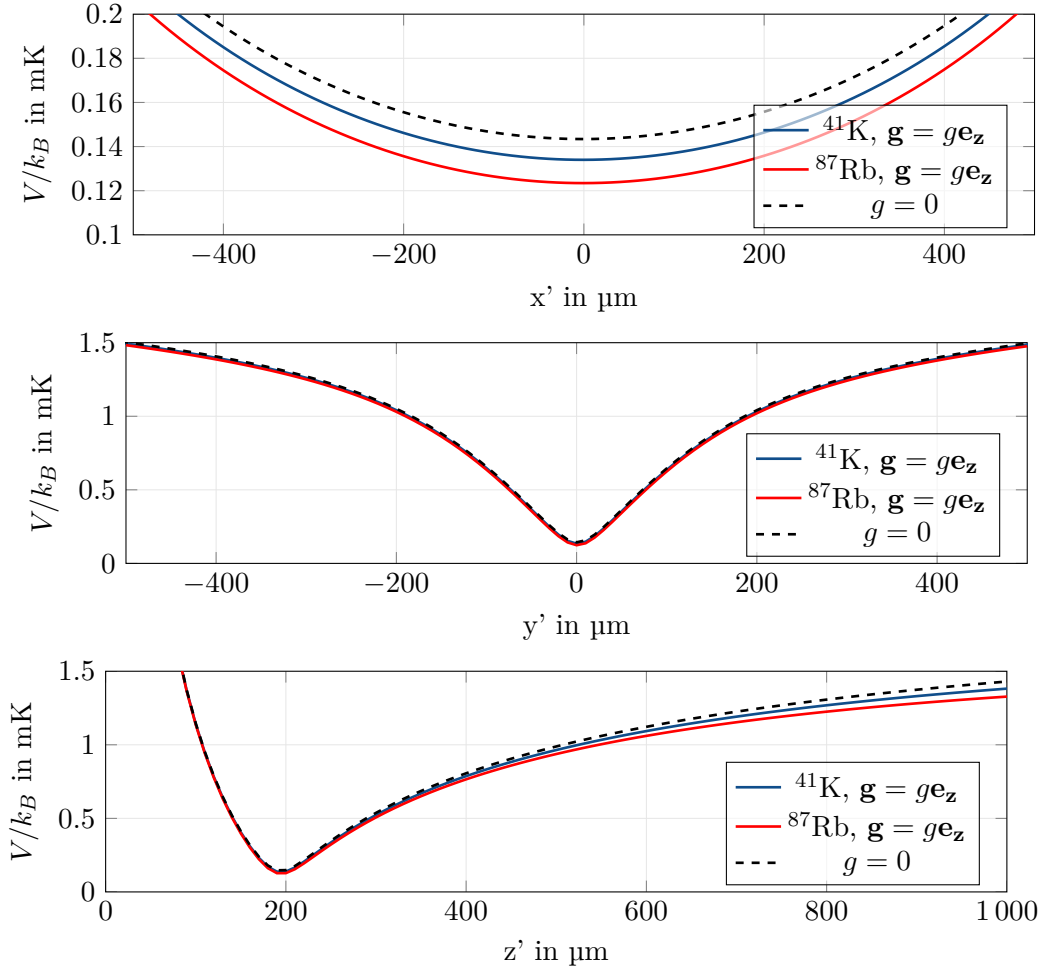


Figure 3.3: Simulated trapping potentials V/k_B for ^{41}K (solid blue line) and ^{87}Rb (solid red line) in the initial evaporation trap (Base-Z: 5.0 A, Science-Z: 2.0 A, y-coil: -2.0 A, x-coil: -0.5 A, z-coil: 0.0 A). Gravity points along z-axis, thus vertically to the atom chip surface. The offset of the ^{41}K potential is due to its smaller atomic mass. In microgravity, the curves perfectly overlap (dashed black line). The eigenaxes are tilted slightly ($< 2^\circ$ for all axes) to the reference coordinate system. As seen in the bottom curve, the trap minimum is located at a distance of $194\mu\text{m}$ to the surface of the Science chip. The geometric mean trapping frequencies are $\bar{\omega}_{\text{Rb}} = 2\pi \cdot 267\text{Hz}$ and $\bar{\omega}_{\text{K}} = 2\pi \cdot 387\text{Hz}$, respectively.

3.2 Bose-Einstein condensation of ^{87}Rb

3.2.1 General remarks

Since a sympathetic cooling approach is followed in this experiment, it is necessary to evaporate ^{87}Rb atoms from the magnetic trap without affecting the ^{41}K atoms. This is possible by removing the most energetic ^{87}Rb atoms in the low-field seeking state $|F = 2, m_F = 2\rangle$ by applying a microwave resonant to the high-field seeking state $|F = 1, m_F = 1\rangle$. After thermalization of the truncated energy distribution, the temperature of the ^{87}Rb ensemble

settles at a lower value. By sweeping the microwave frequency down with an appropriate rate depending on the scattering rate of the atoms, the PSD of the ensemble can be increased efficiently [Ket96]. It turns out that an impurity of ^{87}Rb atoms accumulates in the weakly trapped state $|F = 2, m_F = 1\rangle$ during the evaporation process (see fig. 3.4). As long as the maximum total energy of an atom in any trapped state is larger than $\mu_B B_0$ with the trap bottom magnetic field B_0 and the Bohr magneton μ_B , the evaporation microwave (fig. 3.4, in red) removes also atoms in the impurity state [Ell18]. In later stages, when the maximum total energy of a trapped atom is less than $\mu_B B_0$, the impurity atoms would heat up the atoms sitting in $|F = 2, m_F = 2\rangle$ since they are in thermal contact. To avoid this, a second depumper microwave at a fixed frequency (shown in blue) removes the remaining atoms in the $|F = 2, m_F = 1\rangle$ state. A depumper microwave is a commonly used tool for reaching quantum degeneracy in magnetic traps and is also utilized in [Cam10; Ell18; Haa07; Kle07b; Mar07; Mod01; Wan11], among others. It is also possible to tune the depumper microwave into resonance with the non-magnetic state $|F = 1, m_F = 0\rangle$ which would also deplete the impurity state. This approach, however, would not work sufficiently in microgravity due to the absence of a gravitational field which pulls the atoms away from the trap. As observed in microgravity experiments, atoms left in a magnetically insensitive state lead to a non-vanishing halo-cloud of thermal atoms which might disturb any subsequent measurements [Ave20; Vog20].

There are four known mechanisms which lead to an accumulation of atoms in $|F = 2, m_F = 1\rangle$:

1. Imperfections of the polarization of the optical pump beam lead to a finite amount of atoms trapped initially in the weakly confined state. This can be minimized by a careful adjustment of the polarization and the offset magnetic field during state preparation.

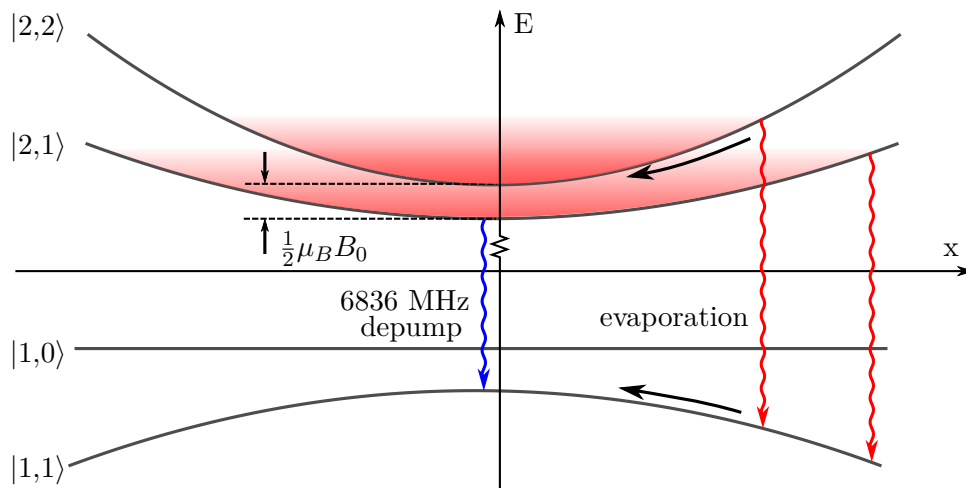


Figure 3.4: Relevant energy levels of ^{87}Rb during microwave evaporation. The evaporation frequency is shown in red. It is resonant for both trapped states since the highest energy atoms in $|2,1\rangle$ have an energy higher or equal than $\mu_B B_0$. A second microwave (blue) removes atoms accumulating in the impurity state.

2. Atoms in the high-field seeking ground state $|F = 1, m_F = 1\rangle$ leave the trap center and later become resonant with the impurity state again (cf. red arrows in fig. 3.4). This effect has also been presumed in [Ell18; Haa07; Wan11; Xio10] and cannot be avoided in the here pursued scheme.
3. Noise in the chip current drivers resonant to the Larmor frequency $1/2\mu_B B_0$ induce transitions between the two states. A more detailed characterization of the effects of current noise in this experiment is discussed in [Bar21]. To reduce this effect, special care in the design of the chip current drivers is required to minimize the noise spectrum in this frequency range.
4. Due to spin-spin dipole interaction and a second-order spin-orbit interaction, spin-polarized ^{87}Rb -atoms can undergo dipolar relaxation. This process of the form $|2,2\rangle + |2,2\rangle \rightarrow |2,1\rangle + |2,2\rangle$ is non-intuitive since it does not conserve the total spin projection and is only explained due to relativistic forces [Mie96]. Nonetheless, it has been identified to populate the impurity state as reported in [Sil05]. As a two-body collision process, it scales with the atom density n^2 and can thus be reduced by decompression of the trap.

It turns out that ^{87}Rb atoms in the impurity state lead to a dramatic decrease of the co-trapped ^{41}K atoms. Thus, special care has to be taken to remove them in order to minimize their detrimental effect.

The impurity state does not show up if the evaporation is conducted using a radiofrequency field resonant to $|F = 2, m_F = 2\rangle \rightarrow |F = 2, m_F = 1\rangle$ [Her13; Sei14] since it is (to first order) also resonant to the other Zeeman substates which naturally depletes any impurity states by the transition $|F = 2, m_F = 1\rangle \rightarrow |F = 2, m_F = 0\rangle$.

The setup of the two-frequency microwave source is shown in fig. 3.5 and consists of two separate circuits: The depumper microwave is set to a fixed frequency at 6836.44 MHz which is synthesized using a PLL with an integrated voltage controlled oscillator (*Analog*

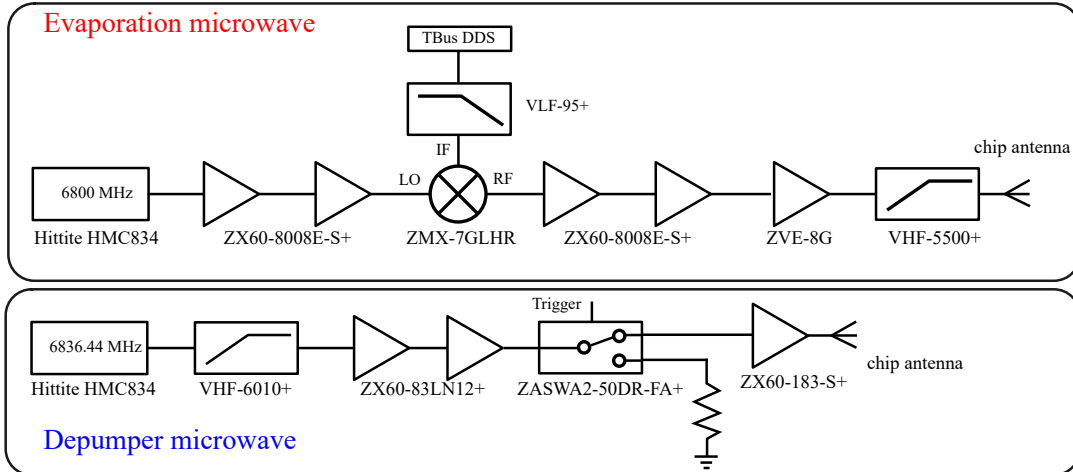


Figure 3.5: Setup of the microwave source used for evaporation (upper panel) and depumping (lower panel) of ^{87}Rb in the magnetic trap.

Devices HMC834), amplified and directed to a microwave structure on the Base chip (see fig. 2.6). The depumper can be triggered using a high isolation microwave switch which transmits up to 18 dBm. The evaporation microwave has to allow for frequency- and amplitude sweeps and is thus realized with a frequency mixer which generates flexible radiofrequency sidebands around the carrier of 6.8 GHz with an amplitude of 20 dBm.

3.2.2 Microwave evaporation of ^{87}Rb

The trajectory of the evaporation frequency is constrained by nine concatenated linear ramps which are optimized in duration and frequency. Furthermore, the magnetic trap can be decompressed during a ramp by relaxing its trap frequencies. This is achieved by decreasing the current through the y-coils. The decompression reduces losses which originate from inelastic three-body recombination processes which start to become relevant at atomic densities above $10^{15}/\text{cm}^3$ [Bur97]. The optimization of the ramps has been conducted using an automated, open-source learning algorithm which is based on a Gaussian process (MLOO, [Wig16]): In each experimental run, a predefined cost function is calculated and the ramp parameters are adjusted with the help of the learning algorithm to minimize the cost. The exploited cost function did not include the total duration of the evaporation ramp and rather produces large and pure condensates. The optimized ramps for the microwave frequency, magnetic bias field in y-direction and resulting trap frequencies and PSD are shown in fig. 3.6. The PSD is measured after each ramp using the relation

$$PSD = N \left(\frac{\hbar\bar{\omega}_r}{k_b T} \right)^3, \quad (3.1)$$

with the atom number N , temperature T and geometric mean frequency $\bar{\omega}_r = (\omega_{x'}\omega_{y'}\omega_{z'})^{1/3}$ of the release trap.

A PSD above 2.6 is accompanied by the onset of Bose-Einstein condensation [Pet08]. Any further evaporation leads to a higher condensate fraction N_0/N with the number of condensed atoms N_0 and the total atom number N . The phase transition is associated with the emergence of a bimodal density distribution of the atom cloud from which the thermal and condensed fractions are inferred, as shown in fig. 3.7(b). The phase transition in a harmonic trap is characterized by a critical temperature given by the approximation [Pet08]

$$T_c = \frac{\hbar\bar{\omega}}{k_B} \left(\frac{N}{\zeta(3)} \right)^{1/3} \approx 0.94 \frac{\hbar\bar{\omega}}{k_B} N^{1/3}, \quad (3.2)$$

with the geometric average of the trap eigenfrequencies $\bar{\omega} = (\omega_{x'}\omega_{y'}\omega_{z'})^{1/3}$ and the Riemann Zeta function $\zeta(3) \approx 1.202$. For typical experimental parameters with $N = 10^6$ ^{87}Rb atoms at the onset of condensation and a release trap $\omega_{x',y',z'} = 2\pi \cdot (26, 322, 323)$ Hz, the critical temperature is given by $T_c \approx 625$ nK. In fig. 3.7(a), the temperature dependence of the condensate fraction at the phase transition is shown in comparison with the theoretical prediction for a non-interacting Bose gas in an anisotropic harmonic potential (dashed line)

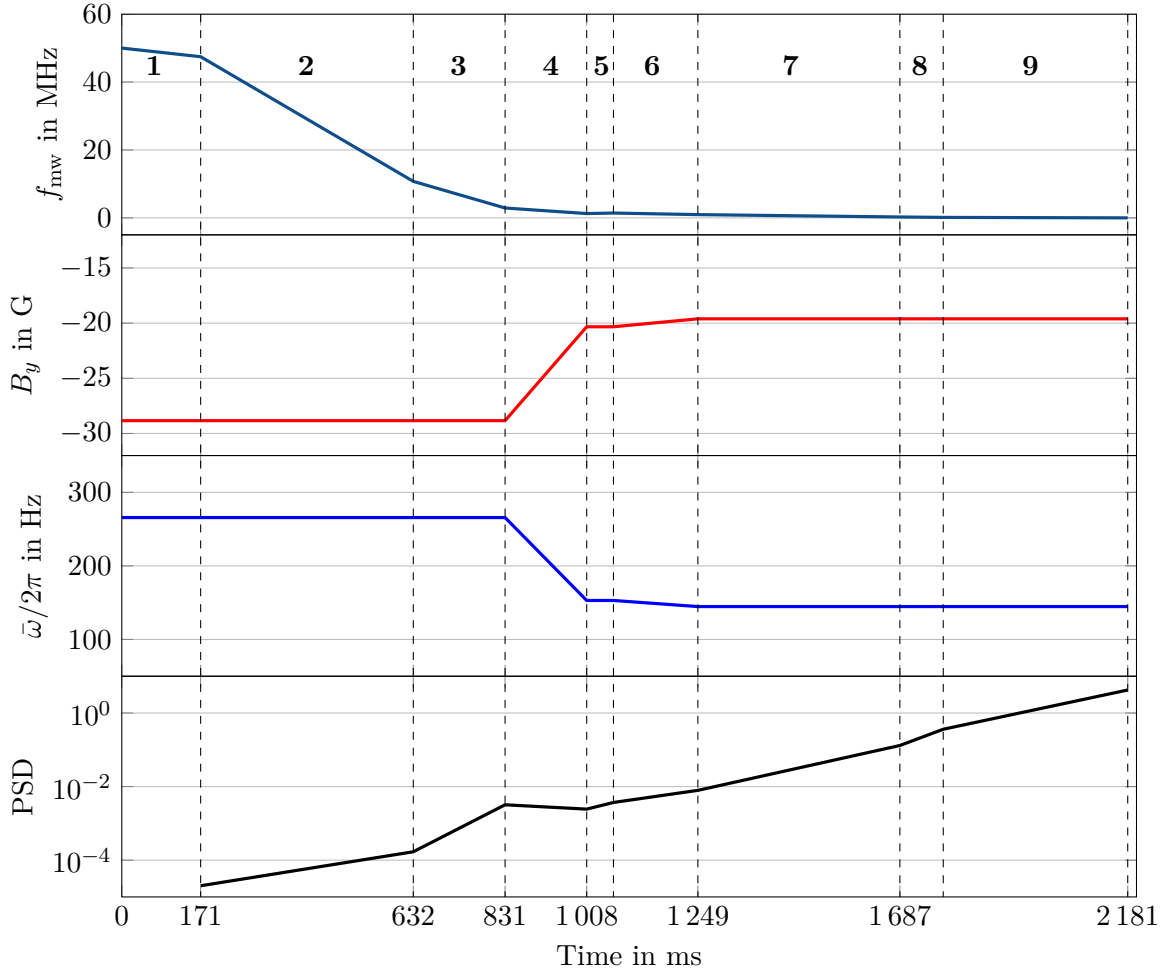
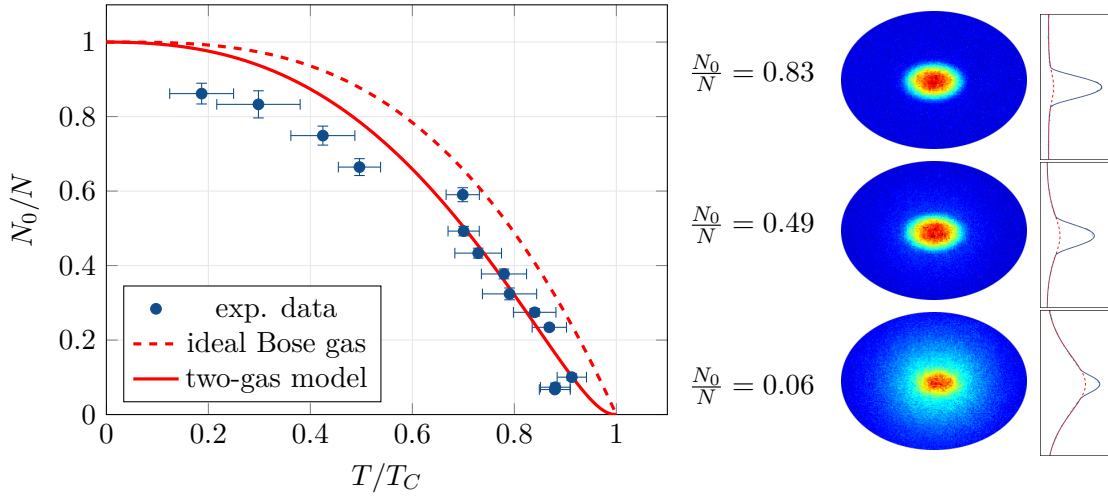


Figure 3.6: Ramps for microwave frequency (upper graph) and y-component of the bias magnetic field (second graph) during evaporation of ^{87}Rb . The frequency f_{mw} is given relative to the final evaporation frequency of 6839.99 MHz. The resulting geometric mean trapping frequency is shown in the third graph. The bottom graph shows the PSD during the evaporation. The fourth and sixth ramp are the decompression steps. The currents through the Science-Z, Base-Z and x-coil are stabilized at 2.0 A, 5.12 A and -0.5 A during the evaporation, respectively.

$$\frac{N_0}{N} = 1 - \left(\frac{T}{T_c(N)} \right)^3, \quad (3.3)$$

with the critical temperature given by eqn. (3.2) [Bag87]. A systematic shift of the condensed fraction below the prediction of the ideal Bose gas is clearly visible. This shift can be understood by taking an additional thermal depletion of the condensate into account due to repulsive interactions of the atoms [Gio96]. In [Nar98] it is shown that the thermal depletion originates mainly from mean-field repulsion of condensed atoms. However, the



(a) Bose condensed fraction N_0/N below the critical temperature T/T_C .

(b) Density distributions of the condensed ensembles.

Figure 3.7: Phase transition of the ^{87}Rb ensemble. The theoretical curves in panel (a) show the expected behaviour for an ideal, non-interacting Bose gas given by eqn. (3.3) (dashed line) and a numerical solution of a two-gas model taking mean-field repulsion of the condensed fraction into account [Nar98]. In panel (b), three exemplary density distributions along the phase transition are shown. The solid blue curve shows the condensed fraction on top of the thermal background (red dashed line) following a two-dimensional Bose-enhanced Gaussian function [Szc09]. The topmost picture shows an almost pure BEC with $2 \cdot 10^5$ condensed atoms.

thermal part can still be treated as an ideal gas in an effective potential which is given by the trap potential and a mean-field repulsion of the condensate. A comparison of the experimental data with the numerical integration of this two-gas model (solid line) shows good agreement especially at moderate condensate fractions $N_0/N < 0.5$. The systematic deviation at high condensate fractions might have its origin from a systematic overestimation of the thermal fraction in the image analysis.

3.3 Sympathetic cooling of ^{41}K

Direct evaporative cooling of trapped atoms puts stringent requirements on trapped atom numbers, atom densities and advantageous collision properties of the evaporated species. Owing to the low scattering energies of cold atoms, the collision properties are mainly given by the position of the last bound states of the interatomic potential. This fixes the value of the s-wave scattering length a which describes the strength of an attractive ($a < 0$) or repulsive interaction ($a > 0$) between two atoms.

Table 3.1 lists the homo- and heteronuclear s-wave scattering lengths of ^{87}Rb and ^{41}K atoms. Since the ensembles are prepared in the stretched state $|F = 2, m_F = 2\rangle$, only the triplet scattering length a_t applies for the determination of the cross section during evaporation.

Although the ^{41}K - ^{41}K scattering length is sufficiently high to allow for fast thermalization during direct evaporative cooling [Che16; Kis09] it would require a large initial atom number

Table 3.1: Singlet (a_s) and triplet (a_t) zero-energy s-wave scattering length of ^{41}K and ^{87}Rb in units of Bohr radii a_0 .

Isotopes	a_s/a_0	a_t/a_0	experimental method
^{41}K - ^{41}K	85.53 ± 0.06	60.54 ± 0.06	molecular photoassociation [Fal08]
^{41}K - ^{87}Rb	14.6 ± 0.6	165.3 ± 0.9	Feshbach spectroscopy [Fer06]
^{87}Rb - ^{87}Rb	90.6	98.96	Feshbach spectroscopy [Mar02]

in the magnetic trap comparable to ^{87}Rb to produce condensates with reasonable particle numbers. It turns out that this is not feasible in the present setup due to the known drawbacks in laser cooling efficiency of ^{41}K . The demonstration of highly efficient and robust sub-Doppler cooling of ^{39}K [Nat13; Sal13] and ^{41}K [Che16; Wu17] using dark state enhanced cooling techniques on the D1-line at 770.1 nm shows alternative routes to generate magnetic traps of ^{39}K and ^{41}K with high particle numbers. In collaboration with a Bachelor project [Fre18], this alternative cooling scheme for ^{41}K has successfully been demonstrated in the experiment. However, for the following discussion of sympathetic cooling of ^{41}K , this technique has not been applied to ensure applicability to the flight system¹.

Sympathetic cooling for neutral atoms has first been applied to produce BEC mixtures of different internal composition [Mya97], for bosonic isotopes of the same species like ^{85}Rb and ^{87}Rb [Blo01] and for the first generation of quantum-degenerate Bose-Fermi mixtures using ^6Li and ^7Li [Sch01; Tru01]. Since then, the technique has frequently been used to promote efficient cooling either for smaller bosonic atom ensembles like $^{39}\text{K}/^{41}\text{K}$ or for fermions which lack of s-wave collisions due to Pauli-blocking.

Here, ^{41}K -atoms are loaded simultaneously with a buffer gas of ^{87}Rb -atoms into the magnetic trap. Since the 3D-MOT of ^{87}Rb saturates after a short loading time, the additional loading of ^{41}K -atoms can be used to tune the ratio $N_{0,\text{K}}/N_{0,\text{Rb}}$ of initially trapped ^{41}K and ^{87}Rb . Alternatively, the detuning of either the Rb-2D-Cool or K-2D-Cool laser during the 2D-MOT phase might be used to tune $N_{0,\text{K}}/N_{0,\text{Rb}}$ to explore further ratios beyond a maximum ^{87}Rb atom number. For sympathetic cooling, the previously optimized evaporation ramps for ^{87}Rb have not been altered except for the last ramp: Due to the mutual repulsion of ^{41}K and ^{87}Rb , the position of the ^{87}Rb atoms within the trap is slightly displaced which leads to a small increase of the trap bottom magnetic field B_0 and thus final evaporation frequency. This shift amounts to (70 ± 10) kHz and has to be added to the target value of the last ramp. In fig. 3.8, the evaporation and sympathetic cooling phase-space evolution of the mixed ensembles as well as the ^{87}Rb -only case are shown in comparison. In red, the trajectory of the ^{87}Rb ensemble is shown with (solid) and without (dashed) ^{41}K . In the single-species case, it can be approximated by a monomial function $\propto N^{-\Gamma}$ (black dashed line) with the evaporation efficiency $\Gamma = 2.03$ [Dav95]. In the mixed case, below a PSD of 10^{-2} , no influence of the co-trapped ^{41}K -atoms on the

¹ The flight laser system does not provide laser light at 770.1 nm. The required laser module including a spectroscopy setup would implicate a larger rescheduling of the overall laser- and electronics system.

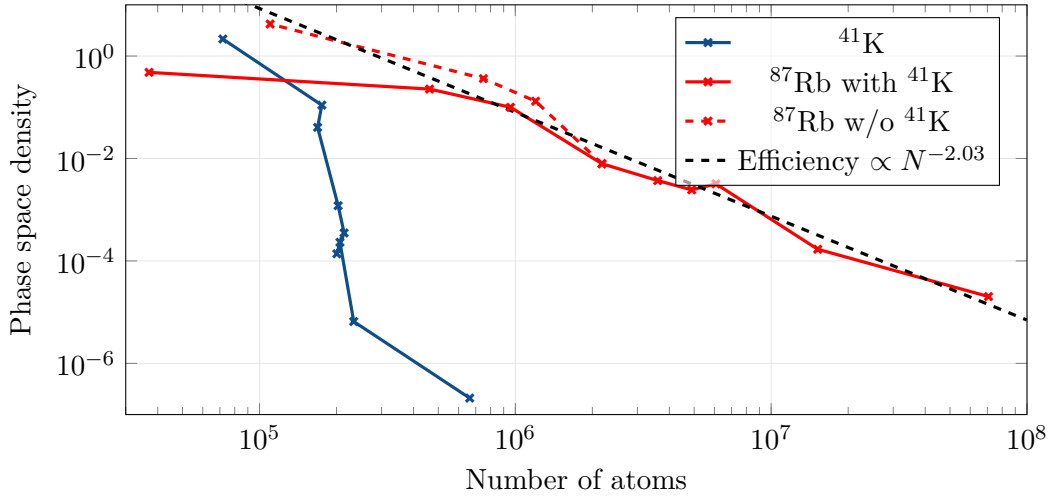


Figure 3.8: Evaporation trajectory of sympathetically cooled ^{41}K (solid blue), ^{87}Rb while acting as a buffer gas (solid red) and ^{87}Rb alone (dashed red). From the latter one, the evaporation efficiency is extracted with a monomial fit (dashed black). The number of atoms always refers to either ^{41}K (solid blue) or ^{87}Rb (other curves).

^{87}Rb -ensemble is observed. This is due to the comparatively low number of ^{41}K -atoms which barely changes the thermal load of the trapped ensembles. At the end of evaporation, when the atom numbers become comparable, the trajectory shows a clear flattening. In blue, the PSD of the sympathetically cooled ^{41}K -ensembles is shown which exhibits a vast atom loss during the first ramp, followed by a steep growth in PSD until Bose-Einstein condensation is reached. The flattening at high PSD is misleading due to a "loss" of thermal atoms into the condensate fraction which is a remnant of the bimodal fit. A detailed discussion of the losses during the first ramp is part of sec. 3.3.1. Depending on the ratio of initially trapped atoms $N_{0,\text{K}}/N_{0,\text{Rb}}$, the number of condensed ^{87}Rb and ^{41}K atoms reveals a quasi-linear dependence with a negative slope as shown in fig. 3.9 (left). Corresponding absorption images of the quantum-degenerate mixtures are shown in the right panel. A mutual repulsion of the clouds is clearly visible and is due to the presence of the co-trapped species as investigated in [Cor20] for different interspecies scattering lengths. Additionally, the presence of gravity leads to an asymmetric ground state of the two-particle wave function which has also been observed and analyzed in [Bur18]. The influence of different gravity orientations and mutual atom repulsion on the ground state of the quantum mixture is investigated in 4.6.

3.3.1 Inelastic collisions of mixed ensembles

By adding more ^{87}Rb into the initial magnetic trap one might guess to enable the production of larger ^{41}K BECs since more ^{87}Rb can handle a larger thermal load. Fig. 3.10 shows a comparison of the resulting atom numbers in the ^{41}K BEC with two different initially trapped ^{87}Rb fractions. The blue dots show the resulting BEC components for $6 \cdot 10^7$

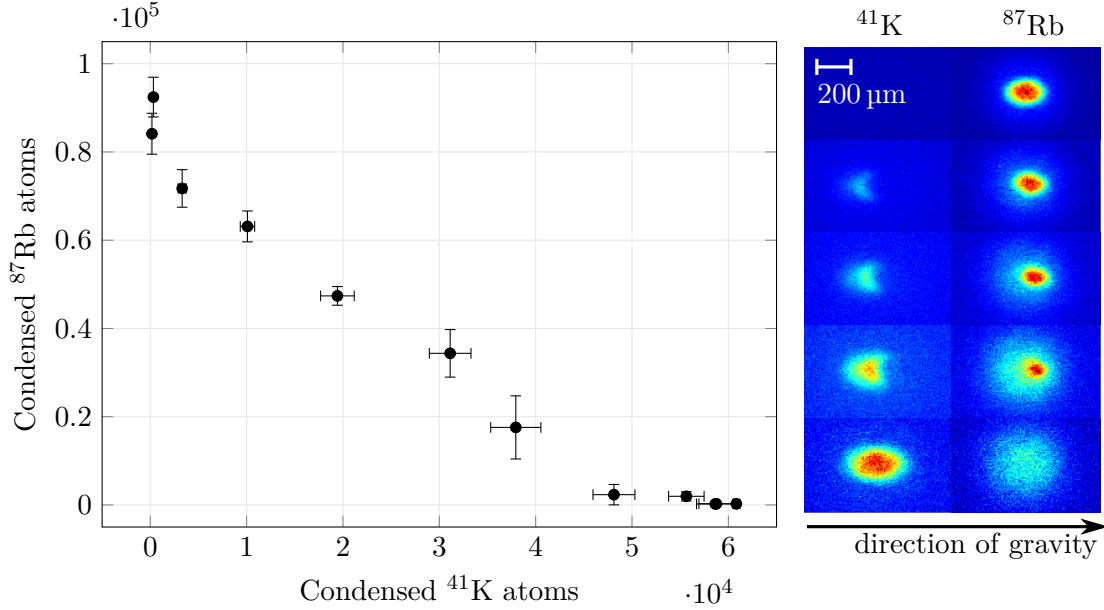


Figure 3.9: Quantum-degenerate mixtures of ^{87}Rb versus ^{41}K . In the left panel, the number of Bose-condensed atoms are shown against each other. Each point corresponds to a mean value of three consecutive measurements each for detecting ^{87}Rb and ^{41}K . The different points correspond to a scan of the K-2D-Cool laser frequency at fixed 3D-MOT loading times of $T_{\text{Rb}} = 250$ ms and $T_{\text{K}} = 1200$ ms. In the right panel, absorption pictures of the mixtures are shown after a time of flight of 20 ms. The particle numbers are extracted using a one-dimensional Gauss+Thomas-Fermi Fit along the vertical direction which gives a symmetric density distribution despite the deformation of the clouds. The direction of gravity is indicated and shows that the heavier ^{87}Rb atoms are pulled below the ^{41}K atoms.

initially trapped ^{87}Rb atoms¹, corresponding to a 3D-MOT loading time of 250 ms. The red dots represent data for 2000 ms MOT-loading of ^{87}Rb resulting in a magnetic trap with $8 \cdot 10^7$ atoms. In both cases, the atom number of magnetically trapped ^{41}K is varied to produce different BEC mixtures. A linear anticorrelation with different slopes between the condensed fractions is observed. The inverse relationship between the BEC atom numbers is a direct consequence of the larger thermal load which is added to the ^{87}Rb buffer gas by increasing the number of initially trapped ^{41}K , denoted by $N_{0,\text{K}}$ in the following. In [Del01], an analytic model for particle number and temperature evolution during sympathetic cooling is developed. The model is based on a simple energy budget and assumes both species to be always thermalized. Further, the number of target atoms $N_{\text{K}}(T) = N_{0,\text{K}}$ is supposed to be constant during the whole evaporation process and all losses in the ^{87}Rb ensemble are due to the truncation of the microwave knife. From these assumptions, the

¹ Atom numbers measured after a holding time of 200 ms.

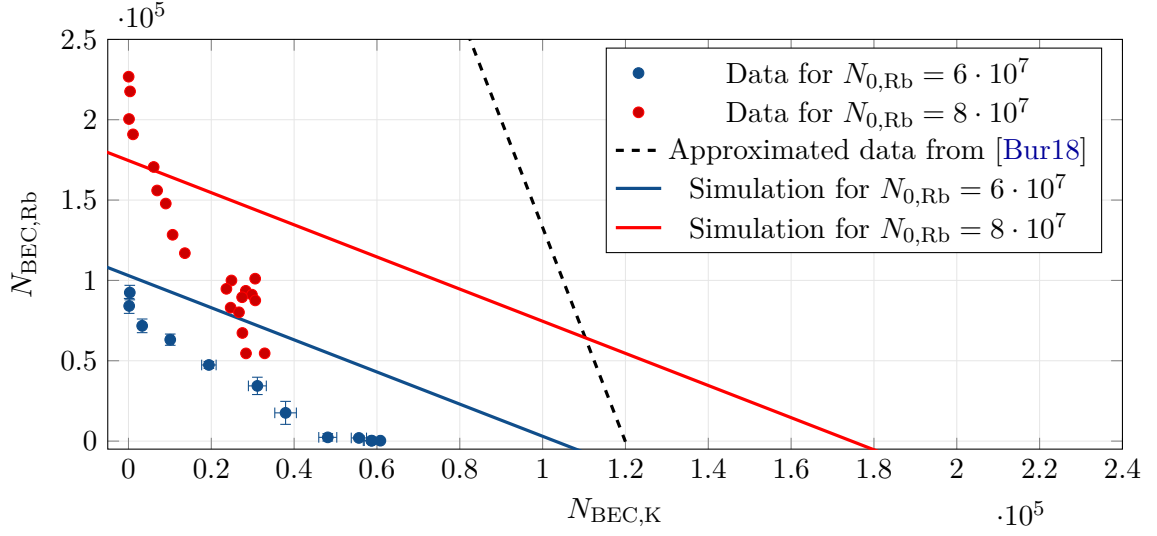


Figure 3.10: Bose-condensed ^{87}Rb and ^{41}K -atoms after sympathetic cooling. Experimental data is shown (red and blue dots) for two different numbers of initially trapped ^{87}Rb atoms. Blue dots are averaged over three experimental runs. The solid lines show the results of a simulation based on eqn. (3.5) and two corresponding different initial conditions. Parameters: $N_{0,\text{K}} = 0$ to 250000, $T = 300$ nK, $\eta = 5.5$, $T_0 = 270$ μK , $\omega_{x,y,z,\text{Rb}} = 2\pi \cdot (26,322,323)$ Hz (for ^{41}K it is multiplied with 1.46 accordingly). For comparison, the data from [Bur18] is indicated with a linear fit (dashed line).

temperature T for given atom numbers N_{Rb} and $N_{0,\text{K}}$ can be determined:

$$T(N_{\text{Rb}}) = T_0 \left(\frac{N_{\text{Rb}} + N_{0,\text{K}}}{N_{0,\text{Rb}}} \right)^{\frac{\eta-2}{3}}. \quad (3.4)$$

Here, T_0 denotes the temperature at the beginning of the evaporation and $N_{0,\text{Rb}}$ the number of initially trapped ^{87}Rb atoms. The parameter η is a measure for the energy cutoff $\eta k_B T$ during evaporation. By using eqn. (3.2), the number of Bose-condensed particles $N_{\text{BEC,K/Rb}}$ at a given target temperature T is determined by

$$N_{\text{BEC,K}} = N_{0,\text{K}} \cdot \left(1 - \left(\frac{T}{T_{\text{C,K}}} \right)^3 \right) \quad (3.5)$$

and

$$N_{\text{BEC,Rb}} = N_{\text{Rb}}(T) \cdot \left(1 - \left(\frac{T}{T_{\text{C,Rb}}} \right)^3 \right), \quad (3.6)$$

with $N_{\text{Rb}}(T)$ implicitly given by (3.4). The calculated condensed atom numbers at $T = 300$ nK for $N_{0,\text{Rb}} = 6 \cdot 10^7$ and $N_{0,\text{Rb}} = 8 \cdot 10^7$ are shown in fig. 3.10 (solid lines). As naively expected, an increase of $N_{0,\text{Rb}}$ allows to condense more ^{87}Rb - and ^{41}K -atoms while

keeping the same slope of the anticorrelation. This is in obvious contradiction with the experimental observation. Indeed, the measurement suggests, that a higher $N_{0,\text{Rb}}$ might even lead to less condensed ^{41}K . Similar observations while producing two-component condensates have been made for ^{41}K - ^{87}Rb mixtures [Bur18; Fer02] and also for ^{39}K - ^{87}Rb mixtures [Wac15].

To investigate the underlying loss processes, the loss rates Γ of pure ^{41}K - and ^{87}Rb -ensembles in the magnetic trap after a single 170 ms evaporation ramp down to a frequency of 6.887 GHz corresponding to an ensemble temperature of 100 μK are measured. Comparison with the loss rates of ^{41}K -atoms co-trapped with different amounts of ^{87}Rb reveal the impact of interspecies loss channels. To measure Γ , the atoms are kept in the magnetic trap and detected after different durations t_{hold} . From an exponential fit $N_0 \cdot \exp(-\Gamma t_{\text{hold}})$, the loss rate can be deduced. This follows the assumption that the loss channels are dominated by one-body losses $\Gamma_{\text{K},1\text{-body}}$ and spin-changing heteronuclear two-body collisions $\Gamma_{\text{K-Rb}}$, while three-body collisions are negligible due to low atom densities. Thus, the total loss rate is given by $\Gamma_{\text{K}} = \Gamma_{\text{K},1\text{-body}} + \Gamma_{\text{K-Rb}}$.

The one-body loss rates are deduced from the lifetimes of the pure ensembles and results in $\Gamma_{\text{K},1\text{-body}} = 0.44 \text{ s}^{-1}$ and $\Gamma_{\text{Rb},1\text{-body}} = 0.29 \text{ s}^{-1}$ as shown in fig. 3.11, left panel. The influence of co-trapped ^{87}Rb atom numbers is shown in the right panel. In this measurement, the same amount of ^{41}K -atoms is loaded into the magnetic trap and ^{87}Rb atoms are added by increasing the ^{87}Rb MOT duration in steps of 20 ms. Obviously, ^{87}Rb -atoms lead to a substantial loss of trapped ^{41}K . The corresponding two-body loss rate $\Gamma_{\text{K-Rb}}$ is deduced for each data point. Notably, $\Gamma_{\text{K-Rb}}$ does not increase linearly to $N_{0,\text{Rb}}$, as one would expect from mere two-body collisions with the entire ^{87}Rb ensemble.

As discussed in section 3.2.1, ^{87}Rb -atoms trapped in the impurity state $|F = 2, m_F = 1\rangle$

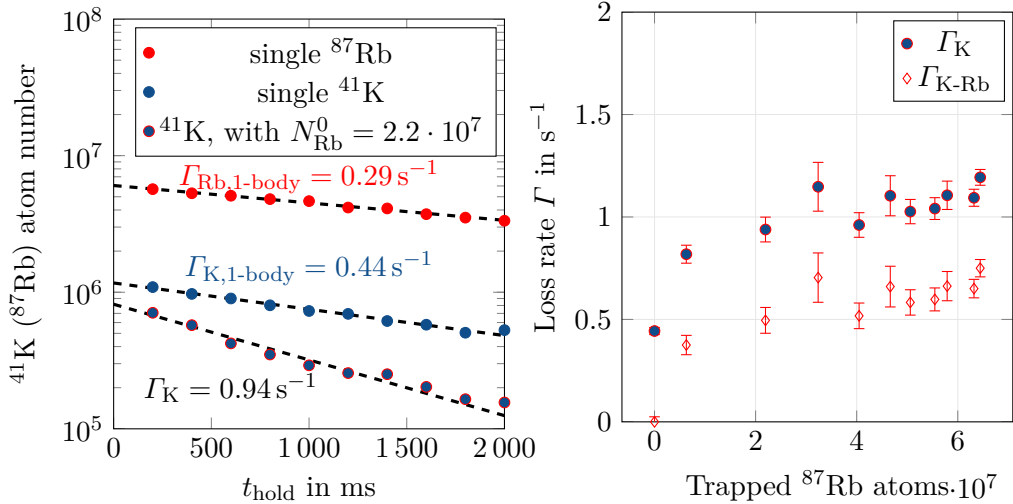


Figure 3.11: Left panel: Three exemplary evaluations of the ensemble lifetimes after the first evaporation ramp ($T = 100 \mu\text{K}$) and determination of loss rates. Right panel: Dependence of ^{41}K loss rate with increasing number of co-trapped ^{87}Rb -atoms and deduced inelastic two-body loss rate $\Gamma_{\text{K-Rb}}$.

are generated before and during the evaporation by various processes. In [Bur18], the inelastic collision rate between $^{87}\text{Rb}|2,1\rangle$ and $^{41}\text{K}|2,2\rangle$ has been calculated using the methods described in [Sim08] which reveals a peak value at collision energies in the range $E/k_B = (100 - 150) \mu\text{K}$. In this energy range, the p-wave scattering exceeds the s-wave contribution by a factor of five, giving a total inelastic collision rate of $L = 1.9 \cdot 10^{-10} \text{ cm}^3\text{s}^{-1}$. Assuming these collisions as the dominant loss-channel for ^{41}K the inelastic collision rate is given by $\Gamma_{\text{K-Rb}} = L \cdot n_{\text{Rb}|2,1}$ which would require a density of $n_{\text{Rb}|2,1} \approx 2.6 \cdot 10^9 \text{ cm}^{-3}$ with $\Gamma_{\text{K-Rb}} \approx 0.5 \text{ s}^{-1}$. The peak atom density in a harmonic magnetic trap is given by [Rei11]:

$$n_0 = N \left(\frac{M\bar{\omega}^2}{2\pi k_B T} \right)^{\frac{3}{2}}. \quad (3.7)$$

Here, $\bar{\omega}$ is the geometric mean of the trap frequencies, T the ensemble temperature, N the number of atoms and M the atomic mass. With typical values ($T = 100 \mu\text{K}$, $M = 87u$, $\omega_{x',y',z',\text{Rb}} = 2\pi(23, 908, 911) / \sqrt{2}^1$), only $N_{\text{Rb}|2,1} \approx 2.3 \cdot 10^4$ atoms in the impurity state suffice to explain the observed drop in lifetime.

At such high temperatures it is not possible to measure $N_{\text{Rb}|2,1}$ directly since the temperature expansion of the magnetic substates is too high to be resolved by Stern-Gerlach separation. Nonetheless, the influence of the depumper microwave can be investigated since it should deplete the magnetic trap of $^{87}\text{Rb}|F = 2, m_F = 1\rangle$ at least during later evaporation stages as described in section 3.2.1. Comparing the number of remaining ^{41}K atoms co-trapped with $N_{0,\text{Rb}} = 4.8 \cdot 10^7$ after a holding time of 1000 ms in the non-evaporated magnetic trap with and without a depumper field reveals a gain of 48% for the remaining ^{41}K fraction if the microwave is switched on. Notably, this gain has only been reached by using the high power evaporation microwave (cf. fig. 3.5, upper circuit) instead of the conventionally used depumper microwave (lower circuit). This result strongly suggests to increase the output power of the depumper microwave which would allow to improve the purity of the ^{87}Rb ensemble while still keeping a high evaporation efficiency.

At later evaporation stages, a higher depumper power does not provide a decrease of Γ_{K} , as already indicated by the evaporation trajectory in fig. 3.8. This is due to the much narrower energy distribution of $^{87}\text{Rb}|2,1\rangle$ at lower temperatures which facilitates a higher efficiency of the depumper rate.

3.3.2 Thermalization of ^{41}K and ^{87}Rb mixtures in gravity

A high spatial overlap of both ensembles is a prerequisite for effective thermalization during sympathetic cooling. It is therefore important to understand the influence of (micro-) gravity to the mutual overlap and thermalization of the ensembles in a quantitative way. In the following, we numerically model the thermalization rate of a ^{41}K - ^{87}Rb mixture in different traps under influence of gravity. The potential $U(\mathbf{r})$ of magnetically trapped

1 The factor $1/\sqrt{2}$ arises from the considered magnetic substate $^{87}\text{Rb}|2,1\rangle$.

atoms with mass m at position \mathbf{r} in presence of a gravitational acceleration \mathbf{g} is given by

$$\begin{aligned} U(\mathbf{r}) &= \mu_B g_F m_F |\mathbf{B}(\mathbf{r})| - m\mathbf{g} \cdot \mathbf{r} \\ &= \frac{1}{2}m (\omega_{x'}^2 x'^2 + \omega_{y'}^2 y'^2 + \omega_{z'}^2 z'^2) - m\mathbf{g} \cdot \mathbf{r}, \end{aligned} \quad (3.8)$$

with the Bohr magneton μ_B , g-factor g_F and magnetic quantum number m_F . In the second line, the trap has been approximated harmonically using its eigenfrequencies $\omega_{x'}, \omega_{y'}, \omega_{z'}$. The gravitational term $-m\mathbf{g} \cdot \mathbf{r}$ leads to a tilt of the trapping potential and a mass dependent shift of the trap minimum as depicted in fig. 3.12. The potential minimum suffices $\nabla U(\mathbf{r}) = 0$. Assuming gravity to act along the z-eigenaxis, the minimum position \mathbf{r}_0 is given by $\mathbf{r}_0 = (0, 0, g/\omega_z^2)$. In general, the direction of gravity is tilted with respect to the eigenaxes of the chip trap, which leads to a gravitational sag in all directions. By using $\omega_{\text{Rb}}^2 = m_{\text{Rb}}/m_{\text{K}}\omega_{\text{K}}^2$, the relative gravitational sag Δ_g between ^{41}K and ^{87}Rb along z is given by

$$\Delta_g = z_{0,\text{Rb}} - z_{0,\text{K}} = g \left(\frac{m_{\text{Rb}} - m_{\text{K}}}{m_{\text{Rb}}\omega_{z,\text{Rb}}^2} \right) \approx \frac{5.19}{\omega_{z,\text{Rb}}^2} \text{Hz}^2\text{m}. \quad (3.9)$$

It depends quadratically on the inverse of the trap frequency in z-direction and thus becomes relevant especially for shallow traps. The relative gravitational sag causes a decrease of overlap between the thermal clouds and will thus reduce the thermalization rate of ^{41}K during sympathetic cooling. The normalized density distribution of a thermal atom cloud is given by the Boltzmann distribution

$$n(\mathbf{r}) = \frac{1}{Z} \exp\left(-\frac{U(\mathbf{r})}{k_B T}\right) \quad (3.10)$$

with the trapping potential given by eqn. (3.8) and a normalization factor Z which can be evaluated using $N = \int d^3r n(\mathbf{r})$. Note that the spatial distributions $n(\mathbf{r})$ depend on the ensemble temperature T . For high temperatures, the size of the trapped atom clouds might be larger than Δ_g , resulting in a high spatial overlap. Correspondingly, the effect

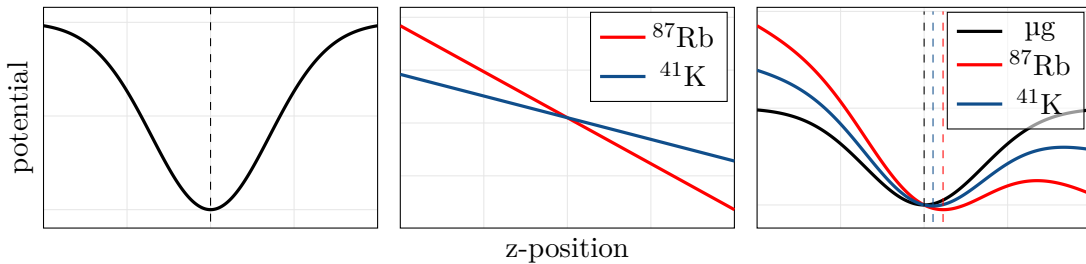


Figure 3.12: Gravitational sag for ^{41}K and ^{87}Rb . The left picture shows the magnetic trapping potential. The central picture indicates the gravitational potentials which scale with the atom mass. The right picture shows the added potentials and the resulting shift of the trap minimum (dashed lines).

of the relative gravitational sag is only visible for atoms at sufficiently low T . A decrease of spatial overlap directly modifies the interspecies collision rate Γ_{coll} which is given by [Mos01]

$$\Gamma_{\text{coll}} = \sigma_{\text{KRb}} \bar{v} \int d^3r n_{\text{K}}(\mathbf{r}) n_{\text{Rb}}(\mathbf{r}), \quad (3.11)$$

with the interspecies scattering cross section $\sigma_{\text{KRb}} = 4\pi a_{\text{K,Rb}}^2$ which depends on the triplet scattering length $a_{\text{K,Rb}}$ (cf. table 3.1). The mean thermal relative velocity \bar{v} is given by

$$\bar{v} = \left[\frac{8k_B}{\pi} \left(\frac{T_{\text{Rb}}}{m_{\text{Rb}}} + \frac{T_{\text{K}}}{m_{\text{K}}} \right) \right]^{1/2}, \quad (3.12)$$

which accounts for a slower collision rate due to lower temperatures. The trap frequencies affect the collision rate implicitly via the density distributions. In table 3.2, collision rates per atom are listed for different atom traps with and without gravity. In general, higher trap frequencies lead to an increased collision rate. Furthermore, they reduce the relative gravitational sag which enhances the spatial overlap of the ensembles.

Having two ensembles with a temperature difference $\Delta T = T_{\text{K}} - T_{\text{Rb}}$, the interspecies thermalization rate $1/\tau$ is defined by

$$\frac{1}{\tau} = -\frac{1}{\Delta T} \frac{d\Delta T}{dt}. \quad (3.13)$$

An expression for $\frac{d\Delta T}{dt}$ can be obtained by considering the energy budget of the ensembles allowing them to exchange their energy by elastic collisions. The energy change of each ensemble is given by the ideal gas equation

$$\begin{aligned} dE_{\text{Rb}} &= \Delta E_{\text{Rb} \rightarrow \text{K}} \Gamma_{\text{coll}} dt = \frac{3}{2} N_{\text{Rb}} k_B dT_{\text{Rb}} \quad \text{and} \\ dE_{\text{K}} &= -\Delta E_{\text{Rb} \rightarrow \text{K}} \Gamma_{\text{coll}} dt = \frac{3}{2} N_{\text{K}} k_B dT_{\text{K}}. \end{aligned} \quad (3.14)$$

Here, $\Delta E_{\text{Rb} \rightarrow \text{K}}$ denotes the average energy exchange after an elastic collision and is given by [Mos01]

$$\Delta E_{\text{Rb} \rightarrow \text{K}} = \xi k_B \Delta T. \quad (3.15)$$

The dimensionless prefactor ξ is defined by

$$\xi = \frac{4m_{\text{Rb}}m_{\text{K}}}{(m_{\text{Rb}} + m_{\text{K}})^2}, \quad (3.16)$$

and follows from plain kinematics and accounts for different masses of the scattering particles. For equal masses, it is $\xi = 1$ and thus the average energy exchange per collision is maximized. In the case of ^{87}Rb and ^{41}K , the energy exchange is reduced by a factor of 0.87. Addition of eqn. (3.14) as well as using eqn. (3.15) and eqn. (3.11) leads to the

Table 3.2: Relative gravitational sag and calculated collision rates per atom $\Gamma_{\text{coll}}/(N_{\text{Rb}}N_{\text{K}})$ for different magnetic traps and a typical crossed optical dipole trap (ODT). Currents used for simulation: Science-Z: 2 A, Base-Z: 5.12 A, x-coil: -0.5 A. $T = 300$ nK.

Trap	$(\omega_{x'}, \omega_{y'}, \omega_{z'})_{\text{Rb}}$ in $2\pi \cdot \text{Hz}$	Δ_g in μm	$\Gamma_{\text{coll}}/(N_{\text{Rb}}N_{\text{K}})$ (gravity), in s^{-1}	$\Gamma_{\text{coll}}/(N_{\text{Rb}}N_{\text{K}})$ (microgravity), in s^{-1}
$I(y) = -0.9$ A	(24.4, 136, 134)	7.1	$1.5 \cdot 10^{-4}$	$2.1 \cdot 10^{-4}$
$I(y) = -1.1$ A	(25.5, 211, 211)	2.9	$4.7 \cdot 10^{-4}$	$5.3 \cdot 10^{-4}$
$I(y) = -1.36$ A	(25.3, 345, 347)	1.1	$1.4 \cdot 10^{-3}$	$1.4 \cdot 10^{-3}$
ODT	(50, 50, 50)	52.6	$5.4 \cdot 10^{-6}$	$5.9 \cdot 10^{-5}$

thermalization rate

$$\frac{1}{\tau} = \frac{2}{3}\xi \left(\frac{N_{\text{Rb}} + N_{\text{K}}}{N_{\text{Rb}}N_{\text{K}}} \right) \sigma_{\text{KRb}} \left[\frac{8k_B}{\pi} \left(\frac{T_{\text{Rb}}}{m_{\text{Rb}}} + \frac{T_{\text{K}}}{m_{\text{K}}} \right) \right]^{1/2} \int d^3r n_{\text{K}}(\mathbf{r}) n_{\text{Rb}}(\mathbf{r}). \quad (3.17)$$

Notably, it is proportional to the total particle number¹ $N_{\text{Rb}} + N_{\text{K}}$ which emphasizes the beneficial effect of high atom numbers. Simulations of τ for different magnetic trap configurations in comparison with a typical crossed optical dipole trap (ODT) including the resulting gravitational sags are shown in 3.13 (solid lines). For these calculations, the

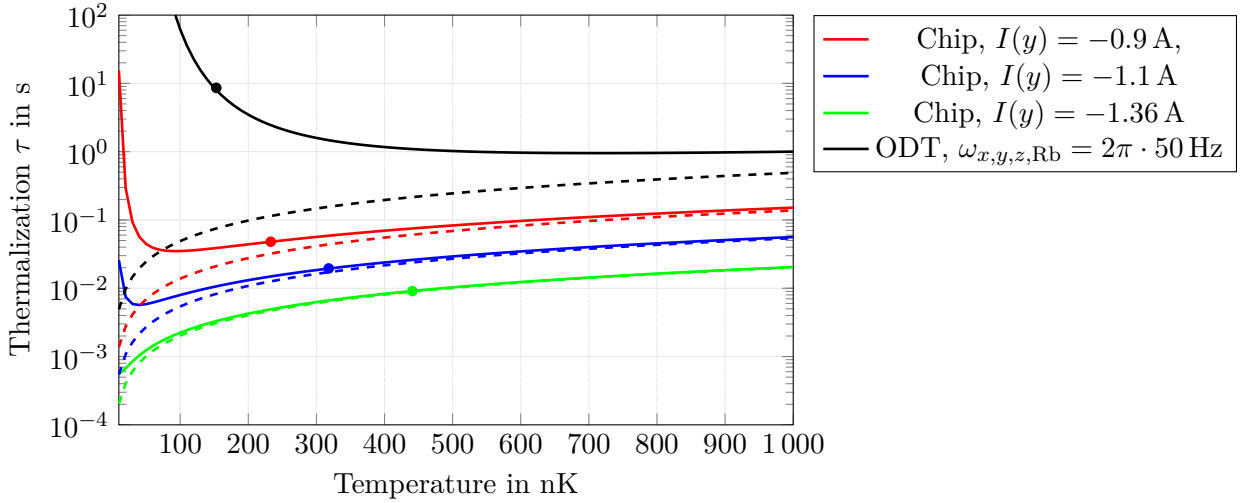


Figure 3.13: Timescale of interspecies thermalization τ for different traps and ensemble temperatures. Respective trap frequencies are listed in table 3.2. Colored solid lines represent different harmonic traps using the atom chip. Black solid line shows the simulation for a typical crossed optical dipole trap (cf. [Bur18]). The corresponding dashed lines show the thermalization rates without gravity. The circles indicate the onset of Bose-Einstein condensation according to eqn. (3.2). $N_{\text{Rb}} = N_{\text{K}} = 10^5$ for each simulation.

¹ The factor $N_{\text{Rb}}N_{\text{K}}$ cancels with the normalization factor contained in $n_{\text{K}}(\mathbf{r})n_{\text{Rb}}(\mathbf{r})$.

overlap integral has been solved numerically after computation of the potential energy curves and trap frequencies with a gauged magnetic field simulation [Mül19]. It is clearly visible that higher trap frequencies lead to a faster thermalization between the ensembles. For very low temperatures at or below the critical temperature, the thermalization time diverges due to a vanishing overlap of the thermal clouds. For lower trap frequencies as for the ODT, the loss of thermal contact occurs at higher temperatures around 300 nK. In microgravity (dashed lines), the thermalization time does not diverge but is enhanced due to a better spatial overlap. It should be noted, however, that the here discussed model allows for energy exchange via elastic collisions but does not account for repulsive interatomic interactions which might lead to further separation of the ensembles beyond the thermal radius for $T < T_c$. Also the particle number of the thermal fraction is kept constant in this simulation, which differs from the ideal experimental situation where $N_K = \text{const.}$ and $N_{\text{Rb}} = N_{\text{Rb}}(T)$.

To compare the thermalization between the two ensembles experimentally, the temperatures of ^{41}K and ^{87}Rb ensembles are both measured at different final frequencies of the evaporation ramp f_0 in the above simulated magnetic traps. If $T_K = T_{\text{Rb}}$, both ensembles are in thermal equilibrium. A decreasing T_K but $T_{\text{Rb}} < T_K$ indicates a loss of thermal equilibrium due to an increased thermalization timescale τ . Results are shown in fig. 3.14. For high trapping frequencies (green and blue dots), ^{41}K temperatures are only slightly above ^{87}Rb temperatures, indicating a fast thermalization in accordance with the simulations. For a weak trap (red dots), thermalization occurs on a longer timescale due to the low trap frequencies. For a more quantitative analysis, the thermalization rate is directly experimentally accessible via species selective parametric excitation of the trapping frequencies and subsequent thermalization [Mod01].

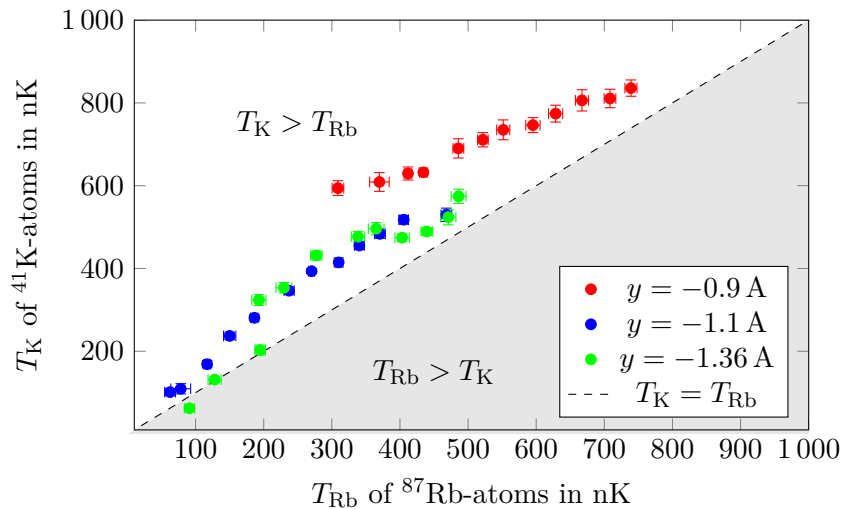


Figure 3.14: Temperature of ^{41}K versus ^{87}Rb at the end of evaporation ramps in different magnetic traps (cf. table 3.2 for trap frequencies). The shaded area represents the domain where $T_{\text{Rb}} > T_K$ which is not accessible in sympathetic cooling. The dashed line indicates thermal equilibrium between both ensembles.

Due to the loss of overlap at the final stages of sympathetic cooling, it is barely possible to generate pure ^{41}K BECs while being comparably easy for ^{87}Rb . Thus, most experiments on ground follow the approach to evaporate both species simultaneously in an optical dipole trap (ODT) at the final stage of BEC generation thus overcoming the need of thermal contact between the ensembles. In microgravity, due to the absence of the gravitational sag, the situation changes in favor of a sympathetic cooling approach. Due to the enhanced thermalization rate at final evaporation stages, it is expected to generate higher condensate fractions for ^{41}K using solely sympathetic cooling in a magnetic trap which is an advantage of a zero-g environment. Still, in presence of gravity, atom chips offer unmatched interspecies thermalization rates due to the high trapping frequencies. This allows the generation of dual-species BECs after less than 2.2 s of evaporation which outperforms most other approaches in terms of repetition rate¹.

3.4 Summary and perspectives

Microgravity campaign

During the sounding rocket flights MAIUS-2 and -3, experiments with ultracold mixtures leading to a WEP test are planned. The here discussed generation of ultracold ^{41}K and ^{87}Rb lay the foundations for the experiments in both missions. The mission MAIUS-2 will focus on the generation and analysis of quantum mixtures in microgravity while MAIUS-3 builds upon this to perform differential atom interferometry. The available experimental time in microgravity is determined by the total mass of 340 kg of the scientific payload and is limited to 324 s with the given rocket engine. This demands to focus on a few core studies which do not rely on time-consuming optimization schemes.

It will be one of the main objectives of MAIUS-2 to generate quantum mixtures with different mixing ratios, as shown in fig. 3.9. The experimental sequence to generate quantum mixtures in microgravity will differ only slightly compared to the ground-based experiments. Spatial mode match between optical molasses and initial magnetic trap was achieved in the first mission MAIUS-1 for ^{87}Rb without further adjustments compared to ground-based parameters [Bec18]. Also for ^{41}K , no additional adaptations are expected. The three-layer magnetic shield limits the influence of different amplitudes or orientations of the experiment with respect to earth's magnetic field. Assuming a pessimistic shielding factor of 100 [Kub16] and a maximum change of the external magnetic field of 1.0 G, the frequencies of the depumper and evaporation microwave would be shifted by at most 14 kHz or 21 kHz, respectively. Thus, no further adjustments of the evaporation ramp due to shifts of external magnetic fields will be needed, as supported by the radiofrequency evaporation during the MAIUS-1 flight [Bec18]. However, to account for magnetic field changes due to position shifts by interspecies repulsion and a differing BEC ground state (see chapter 4.6) within the magnetic trap, the target frequency of the last evaporation ramp has to be examined experimentally during the flight in a range of about 100 kHz around the ground based value.

¹ ^{41}K - ^{87}Rb BEC preparation times using conventional magnetic traps are reported as 50 s [Mod01]. The hybrid approach [Bur18] reports 20 s.

The here pursued combined microwave evaporation and depumping scheme does not allow a transfer of atoms into non-magnetic states. This naturally circumvents the accumulation of thermal atoms in a halo-like cloud centered around the evaporation trap which has been observed in previous microgravity experiments using radio frequency evaporation [Ave20] or optical dipole traps [Vog20].

A determination of thermalization rates requires many experimental runs [Mod01] which makes it unsuitable for a sounding rocket flight with limited experimental time. However, higher condensed ^{41}K atom numbers or condensate fractions compared to experiments on ground would indicate such an effect. This can be probed by scanning the duration of the last evaporation ramp - a higher thermalization rate would shift the optimum to shorter ramps compared to experiments with gravity.

Conclusion

The newly commissioned apparatus has proven to be an efficient tool for fast generation of quantum degenerate mixtures of ^{41}K and ^{87}Rb . The experimental sequence starts with simultaneous loading of both species in a 3D-MOT which reaches its maximum atom number after 0.75 s for ^{87}Rb . Adding extra loading time allows for a tuning of the simultaneously trapped ^{41}K atoms. Followed by conventional MOT decompression, molasses and optical pumping stages, it is possible to load up to $1.5 \cdot 10^8$ ^{87}Rb atoms into a chip magnetic trap with geometric mean trapping frequencies of $\bar{\omega} = 2\pi \cdot 267$ Hz. By applying a microwave knife in combination with a depumper microwave, almost pure ^{87}Rb -BECs containing $3 \cdot 10^5$ atoms are generated.

An adjustable fraction of ^{41}K -atoms can be added into the magnetic trap by applying a modified dark molasses laser cooling scheme to reach sub-Doppler temperatures of 78 μK , followed by optical pumping.

By sympathetic cooling, the apparatus allows the generation of tunable ^{41}K - ^{87}Rb BEC-mixtures with up to $6 \cdot 10^4$ condensed ^{41}K atoms within 3.4 s which sets a new landmark in the fast generation of mixed BECs and quantum degenerate ^{41}K . The high repetition rate relies on the combination of short 3D-MOT loading time of 1.2 s and rapid intra- and interspecies thermalization rates during sympathetic cooling. Compared to approaches utilizing optical dipole traps in the final stages of evaporation instead of an atom chip [Bur18; Mod01], the repetition rate of BEC generation could be enhanced by a factor of more than five. Since the evaporation ramps were optimized for the production of pure and large ^{87}Rb condensates, a further gain in repetition rate is still conceivable. By implementing recent developed molasses cooling schemes for ^{41}K based on D1-transition, the loading of the ^{41}K magnetic trap can be improved, which in case allows shorter MOT loading times. This, in combination with an optimization of the duration of the microwave evaporation, will bring repetition rates of dual-species BEC generation into sight of the Hz regime.

The influence of the gravitational sag to interspecies collisions during sympathetic cooling has been analyzed in detail. For the here used high frequency harmonic traps, a thermalization time below 10 ms at a temperature of 500 nK is derived and demonstrates sufficient thermal contact at the onset of BEC generation on ground as well as in microgravity. For lower trapping frequencies, the thermal contact between the thermal clouds in the presence

of gravity is lost at the point of BEC generation, accompanied by a divergence of the thermalization time.

CHAPTER 4

Dynamics of single and mixed BECs

Analogously to the laser in coherent optics, BECs present ideal sources for matter wave interferometry on long timescales due to their macroscopic coherence length, small size and slow expansion rates.

By employing beam splitter or mirror pulses based on Raman [Lev09] or Bragg double diffraction [Ahl16], it is essential to prepare the input state with a narrow momentum distribution well below the photon-recoil in order to maximize the diffraction efficiency. Following [Har20], for pulse durations of 25 μs , the residual expansion rate has to be below $\sigma_v = 600 \mu\text{m/s}$ to yield a diffraction efficiency above 90% for a single beam splitter pulse. The use of double diffraction techniques for thermal ensembles is not feasible due to strong limitations of beam splitter and mirror efficiencies.

Having a minimal ballistic expansion of the ensemble between the interferometer pulses also reduces the impact of wavefront distortions which is one of the most prominent systematic errors in current cold-atom gravimeters [Kar18; Lou11].

Any acceleration a of the atoms along the interferometry beams results in a phase change of $\Delta\phi = k_{\text{eff}}aT^2 + \mathcal{O}(T^3)$ at the interferometer output, with the effective wave vector k_{eff} and the free fall time between the light pulses T . Thus, the sensitivity of an acceleration measurement can be enhanced by increasing T which is limited by the size of the ballistically expanding ensemble with respect to the interferometer beam size. Having a slowly expanding ensemble allows to increase T and thus to measure (differential) accelerations with unprecedented sensitivity [Ase20].

By employing magnetic lensing techniques [Amm97] with BECs, residual expansion rates down to $\sigma_v = (116.9 \pm 13.9) \mu\text{m/s}$ were demonstrated in the drop tower experiment QUANTUS-2 [Rud16]. To put this into comparison with typical expansion rates of thermal ensembles in modern atom interferometers [Bar16; Bid13; Hau13], a molasses-cooled ensemble of ^{87}Rb at a temperature of 4 μK would result in an expansion rate of $\sigma_v \approx 20 \text{ mm/s}$ which is a factor of 170 higher.

To successfully transfer the techniques of magnetic lensing to the MAIUS-B experiment, detailed knowledge of its magnetic traps regarding position, trap frequencies and switching behavior is required. Additionally, the expansion dynamics of free falling BECs follow from the frequencies of the release trap. An important tool to predict trap positions and frequencies is the atom chip magnetic field simulation which has been gauged to calculate trap frequencies with a relative uncertainty below 3.5% [Mül19].

In sections 4.2 and 4.4, the expansion of free falling BECs of ^{41}K and ^{87}Rb is discussed. The experimental results are compared with numerical simulations based on a scaling

approach [Cas96] and will show the impact of magnetic field transients during release. The first application of magnetic lensing for ^{41}K is presented in the outlook.

During the course of the expansion measurements, collective oscillations of ^{87}Rb and damping due to interactions with ^{41}K atoms have been observed (section 4.3).

In sections 4.5 and 4.6, we focus on a magnetic-gradient free trap release which allows to study the dynamics of two-component BECs and the influence of gravity on trapped mixtures.

The simulations presented in this chapter were realized in collaboration with Annie Pichery and the theory group of Naceur Gaaloul.

4.1 Free expansion of ^{41}K and ^{87}Rb BECs

The free expansion of a BEC suddenly released from a harmonic potential with trap frequencies ω_j can be modeled within the Thomas-Fermi approximation by the temporal evolution of three scaling factors $\lambda_j(t)$ (for $j=1,2,3$) [Cas96]. The scaling factors describe the trajectory of the Thomas-Fermi radii $R_j(t)$ of the released BEC by

$$R_j(t) = \lambda_j(t)R_j(0) \quad (j = 1,2,3). \quad (4.1)$$

The time evolution of the scaling factors for a BEC initially at rest is given by the set of differential equations

$$\ddot{\lambda}_j = \frac{\omega_j^2(0)}{\lambda_j\lambda_1\lambda_2\lambda_3} - \omega_j^2(t)\lambda_j, \quad \dot{\lambda}_j(0) = 0, \quad \lambda_j(0) = 1 \quad (j = 1,2,3). \quad (4.2)$$

These equations allow for general time-dependent harmonic potentials $\omega_j(t)$. In the most simple approach, the harmonic potential is described by a step function due the fast switching times of the atom chip traps. The validity of this approximation for our experiments is discussed in chapter 4.2. In an ideal setting, the atoms are at rest before release, which defines the initial conditions $\lambda_j(0) = 1$ and $\dot{\lambda}_j(0) = 0$. This simplification does not hold for the analysis of atoms released from an excited trap (cf. section 4.3). As revealed by eqn. (4.2), the evolution of the scaling factors does not depend on the interatomic interaction but only on the trap frequencies. The interatomic repulsion enters via the Thomas-Fermi radius of the trapped BEC $R_j(0)$, given by

$$R_j(0) = a_{\text{ho}} \left(\frac{15Na}{a_{\text{ho}}} \right)^{1/5} \frac{\bar{\omega}}{\omega_j(0)}. \quad (4.3)$$

Here, $\bar{\omega}$ is the geometric mean trap frequency, N the atom number, a the scattering length and a_{ho} the harmonic oscillator size given by $a_{\text{ho}} = \sqrt{\hbar/(m\bar{\omega})}$. The scattering lengths a for ^{87}Rb and ^{41}K are given by the triplet scattering lengths listed in table 3.1 as the atoms are prepared in their stretched magnetic substate $|F = 2, m_F = 2\rangle$.

Since the Thomas-Fermi radii $R_j(t)$ are given in the trap coordinate system $\{x,y,z\}$, they have to be projected into the coordinate system of the absorption detection $\{x',y'\}$ to compare with the observables $R_{x'}(t)$ and $R_{y'}(t)$. This is done by a two-fold transformation using rotational matrices. First, the trap coordinate system is rotated into the chip

coordinate system by the rotation M_1 . Subsequently, it is transformed into the coordinate system of the absorption detection by the rotation M_2 . The matrix M_1 is given by the three eigenvectors of the release trap $\mathbf{e}_{x,y,z}$ which are computed by the magnetic field simulation after diagonalization of the trapping potential,

$$M_1 = (\mathbf{e}_x \quad \mathbf{e}_y \quad \mathbf{e}_z). \quad (4.4)$$

For traps close to the chip with high aspect ratio, M_1 can be approximated by a rotation around the z-axis by the tilt angle Θ and residual rotations can be neglected:

$$M_1 = \begin{pmatrix} \cos \Theta & \sin \Theta & 0 \\ -\sin \Theta & \cos \Theta & 0 \\ 0 & 0 & 1 \end{pmatrix}. \quad (4.5)$$

The transformation M_2 into the camera coordinate system is given by

$$M_2 = \begin{pmatrix} 0 & 0 & 1 \\ -\sin \phi & \cos \phi & 0 \\ -\cos \phi & -\sin \phi & 0 \end{pmatrix} \quad (4.6)$$

with the angle $\phi = 46.1^\circ$ ¹ between the detection beam and the x-axis (cf. fig. 2.8). Thus, the x-axis of the images coincides with the z-axis of the chip coordinate system. The y-axis of the images mixes the x- and y-direction. The complete transformation is given by

$$T = M_2 \cdot M_1 \stackrel{\text{only z-rotation}}{\approx} \begin{pmatrix} 0 & 0 & 1 \\ -\sin(\phi + \Theta) & \cos(\phi + \Theta) & 0 \\ -\cos(\phi + \Theta) & -\sin(\phi + \Theta) & 0 \end{pmatrix} \quad (4.7)$$

for traps with high aspect ratio. Any vector \mathbf{r} in the chip coordinate system thus transforms into the camera coordinate system by $\mathbf{r}' = T\mathbf{r}$. Since the Thomas-Fermi radius is proportional to the variance $\Delta r_j^2 := \langle r_j^2 \rangle - \langle r_j \rangle^2$ of the BEC wave function by $R_j = \sqrt{7}\Delta r_j$ [Cor20], we find the transformed Thomas-Fermi radii $R_{x',y'}$ by evaluating the variances

$$\begin{aligned} R_{x'}^2 &= 7\Delta x'^2 = 7\Delta z^2 = R_z^2 \\ R_{y'}^2 &= 7\Delta y'^2 = 7(\langle Y'^2 \rangle - \langle Y' \rangle^2) \\ &= 7(\sin^2(\phi + \Theta)\Delta x^2 + \cos^2(\phi + \Theta)\Delta y^2 - \sin(2\phi + 2\Theta)\Delta xy) \\ &= \sin^2(\phi + \Theta)R_x^2 + \cos^2(\phi + \Theta)R_y^2. \end{aligned} \quad (4.8)$$

Here, we used that $\Delta xy = 0$ since the coordinates are independent. For weak traps, one cannot apply the approximation eqn. (4.5) and has to evaluate T with the exact rotation eqn. (4.4). As a rule of thumb, for elongated traps with a frequency ratio above 5 one can

¹ By pushing the atoms with a resonant detection beam and following the fluorescence of the accelerated ensemble with the front camera, the precise deviation from 45° has been evaluated experimentally.

safely apply the approximate transformations (4.8).

To simulate the BEC expansion, the scaling equations (4.2) are solved numerically and the resulting Thomas-Fermi radii are projected onto the camera coordinate system. In fig. 4.1, (left) the free expansions of ^{41}K and ^{87}Rb are shown in comparison for a weak magnetic trap in microgravity and typical atom numbers. Due to the higher trap frequencies of ^{41}K compared to ^{87}Rb , the Thomas-Fermi radii of the ^{41}K BEC are always larger than the respective radii of the ^{87}Rb BEC at the same time of flight. Even for weak magnetic traps, the Thomas-Fermi radii of both isotopes grow to macroscopic values in the millimeter range after some hundred milliseconds of expansion. This underlines the necessity of magnetic lensing once longer times of flight are accessible due to microgravity.

Using eqn. (4.3), we find the relation between the initial Thomas-Fermi radii of both isotopes within the magnetic trap

$$\frac{R_{j,\text{K}}(0)}{R_{j,\text{Rb}}(0)} = \left(\frac{a_{\text{K-K}}m_{\text{Rb}}}{a_{\text{Rb-Rb}}m_{\text{K}}} \right)^{1/5} \approx 1.054 \quad (j = 1,2,3). \quad (4.9)$$

Due to the smaller scattering length of ^{41}K , the mass imbalance of the isotopes is partly reversed and the Thomas-Fermi radii of the trapped condensates are only slightly different. This is reflected by the similar initial Thomas-Fermi radii shown in fig. 4.1 (right panel).

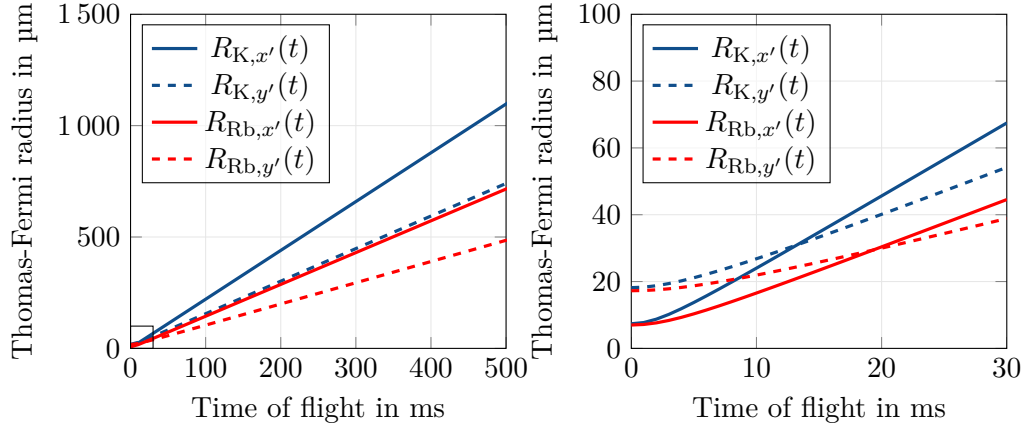


Figure 4.1: Left panel: Simulated Thomas-Fermi radii of ^{41}K (blue) and ^{87}Rb (red), released from a magnetic trap with trap frequencies $\omega_{\text{Rb}} = 2\pi(12,38,35)$ Hz and $\omega_{\text{K}} = 2\pi(18,55,51)$ Hz. $N_{\text{Rb}} = N_{\text{K}} = 5 \cdot 10^4$ atoms. Solid lines show the x' -projection and dashed lines the y' -projection onto the absorption detection coordinate system. Right panel: Thomas-Fermi radii for small times of flight directly after release. Zoomed area is indicated by rectangle in left panel. Currents used for the magnetic trap simulation are $(I_x, I_y, I_z, I_{\text{SC}}, I_{\text{BC}}) = (-0.5, -0.45, 0.0, 2.0, 5.12)$ A, $g = 0$.

4.2 Free expansion of ^{41}K

To measure the temporal evolution of the Thomas-Fermi radii of free falling ^{41}K BECs, ultracold ensembles are prepared in a magnetic trap following the sympathetic cooling approach presented in section 3.3. After evaporation of all ^{87}Rb atoms, an ensemble of $N = (2.9 \pm 0.1) \cdot 10^4$ condensed ^{41}K atoms is left with a thermal background of $N_{\text{th}} = (7.4 \pm 1.9) \cdot 10^4$. Errors denote the standard deviation of atom numbers for many repetitions. From there, the atoms are released into free fall by switching off the currents through the Base and Science chip structures followed by tuning the x- and y-coil to generate the magnetic fields along the detection axis for imaging. After different time of flights, the atoms are detected by absorption imaging. The observed Thomas-Fermi radii are shown in fig. 4.2 (blue dots and diamonds). The dotted gray line shows the simulated expansion behavior based on the scaling eqn. (4.2), assuming an immediate switch-off and $N = 2.9 \cdot 10^4$ atoms. To understand the observed inconsistencies between simulation and experiment, several systematic effects are considered in the following.

Camera resolution

For small times of flight, the size of the ensemble is in the order of the optical resolution of the detection setup. According to the ex-situ characterization it is limited to $\sigma = 17.7_{-2.0}^{+0} \mu\text{m}$ at the edge of the field of view (cf. section 2.1.3). This is included in the simulation by introducing a heuristic correction to the calculated Thomas-Fermi radii by quadratic

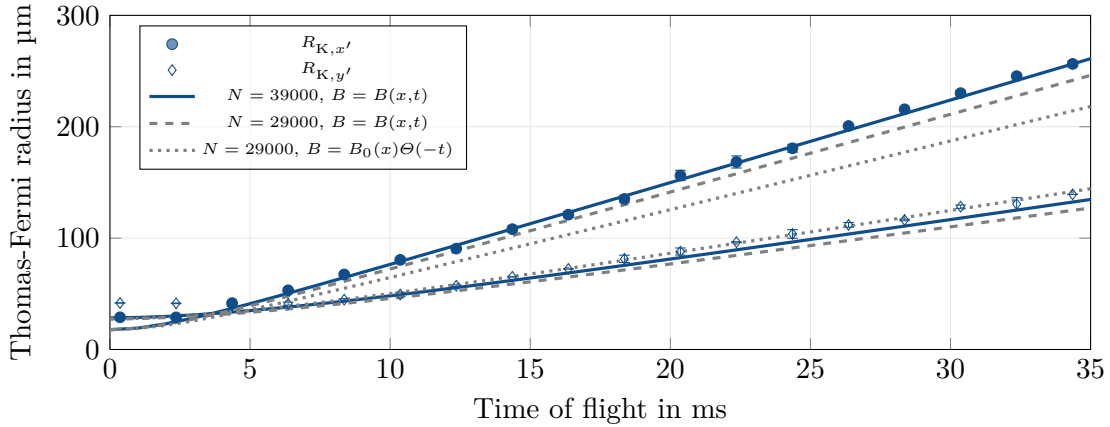


Figure 4.2: Temporal evolution of Thomas-Fermi radii of ^{41}K over two consecutive experimental runs. Solid dots show the expansion along the x' -direction of the camera coordinate system, open diamonds the projection of the ensemble onto the y' -direction of the CCD sensor. Three different models based on eqn. (4.2) are shown: Dotted gray line shows the solution for an immediate switch-off of the magnetic field. Dashed gray line illustrates the impact of an exponential magnetic field transient during release with a time constant of $\tau = 140 \mu\text{s}$. Solid blue line shows the simulation for an additionally 34% higher atom number than suggested by the absorption detection.

addition:

$$R_{x',y',\text{corr}} = \sqrt{R_{x',y'}^2 + \sigma^2}. \quad (4.10)$$

This correction is taken into account by the simulated curves shown in fig. 4.2 which are bounded below by the optical resolution. It only has a considerable impact for small times of flight up to a few milliseconds but does not explain the observed systematic underestimation of $R_{x',y'}$ for longer expansions.

Magnetic field transients

Due to the bulk copper block of the Mesoscopic atom chip and the conducting vacuum chamber, magnetic fields at the position of the atoms might change slower than expected from external current transient measurements [Pop18]. Rapid magnetic field changes lead to eddy currents according to Faraday's law of induction which induce magnetic fields that decelerate the change of the total magnetic field. This effect might lead to unintended changes of the trapping frequencies of the atoms. According to eqn. (4.2), any time dependence of the trapping frequencies $\omega_j(t)$ lead to a different evolution of the Thomas-Fermi radii. To quantify the impact of this effect, the timescale of the magnetic field decay during switch-off has to be known. Subsequently, the temporal dynamics of the trapping potential $\omega_j(t)$ can be estimated by the magnetic field simulation and eqn. (4.2) can be reevaluated with more realistic switch-off dynamics $\omega_j(t)$.

By time-resolved microwave spectroscopy of the released atoms during the switch-off of the chip structures, the timescale of the magnetic field decay can be measured or at least limited from above. Due to the linear Zeeman effect, the microwave transition frequency $\nu(t)$ between the ground states $|F = 2, m_F = 2\rangle \leftrightarrow |F = 1, m_F = 1\rangle$ of ^{41}K or ^{87}Rb is shifted by an external magnetic field $|B(t)|$ by

$$\Delta\nu(t) = \frac{1}{2\pi\hbar} (g_F m_F - g_{F'} m_{F'}) \mu_B |B(t)| = 2.1 \text{ MHz} \frac{|B(t)|}{1 \text{ G}}. \quad (4.11)$$

Here, $g_F = 1/2$ and $g_{F'} = -1/2$ denote the Landé g -factors of the initial and final state, and m_F and $m_{F'}$ the respective magnetic quantum numbers. To measure the magnetic field decay, the frequencies of the microwave transition of ^{87}Rb atoms during release are measured at different times, as shown in fig. 4.3. Owing to the fast change of the resonance frequency while having a low microwave power, only spectra above 0.6 ms after release could be recorded. The transient magnetic field between the trapping bias field B_{IPT} and the bias field in free space B_0 is approximated by an exponential fit of the form

$$B(t) = B_{\text{IPT}} + (B_0 - B_{\text{IPT}}) \cdot (1 - \exp(-t/\tau)). \quad (4.12)$$

The fit suggests a time constant of $\tau = (140 \pm 6) \mu\text{s}$. This is significantly higher than the time constant of the current transient which can be measured externally by a current probe with high dynamic range and results in $\tau_{\text{ext}} = 48 \mu\text{s}$.

Starting from here, the time constant τ is included into the magnetic field simulation to model the switch-off of the currents through the chip wires. The time dependence of

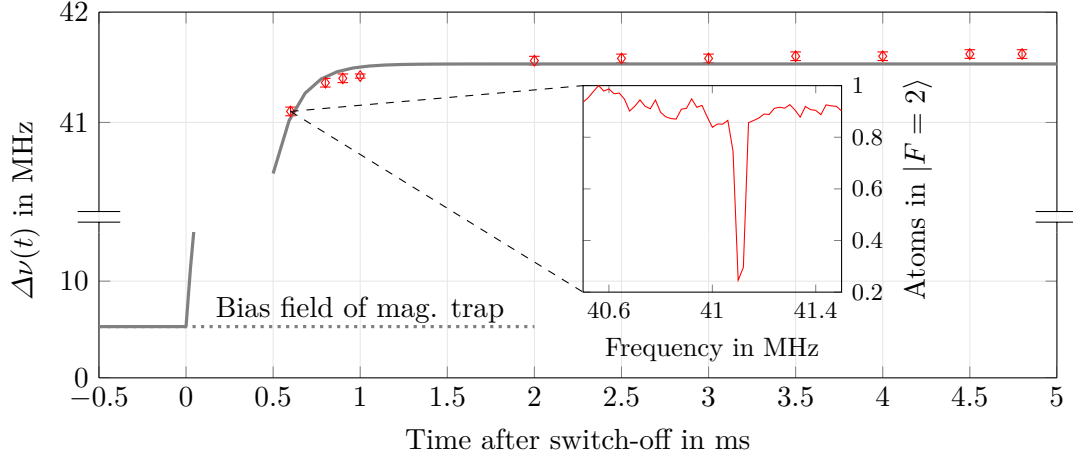


Figure 4.3: Time-resolved microwave spectroscopy of the transient magnetic field after release using a ^{87}Rb BEC as a field probe. Each point shows the Zeeman shift of the microwave transition $|F = 2, m_F = 2\rangle \leftrightarrow |F = 1, m_F = 1\rangle$. The inset shows an exemplary measurement spectrum. Solid line shows an exponential fit according to equation (4.12) and results in a time constant of $\tau = (140 \pm 6) \mu\text{s}$. Dotted line indicates the Zeeman shift given by the bias field of the Ioffe-Pritchard trap before release.

the squared trapping frequencies on the position of the atoms is shown in fig. 4.4. The counterintuitive negative values of ω_z^2 are explained as follows: Since the minimum position of the magnetic trap moves towards the atom chip during switch-off, the potential at the initial trap position becomes a concave function in z -direction (cf. fig. 3.3). The curvature of a potential is directly related to the square of the trap frequency, thus negative values are observed in the case of ω_z^2 . By solving the scaling eqn. (4.2) with the determined time-dependent trapping frequencies $\omega_{x,y,z}^2(t)$, the corrected model can be compared with the simplified model assuming an immediate switch-off. The resulting simulated expansion curves are shown in fig. 4.2 (dashed gray line) and dismantle most of the observed deviations

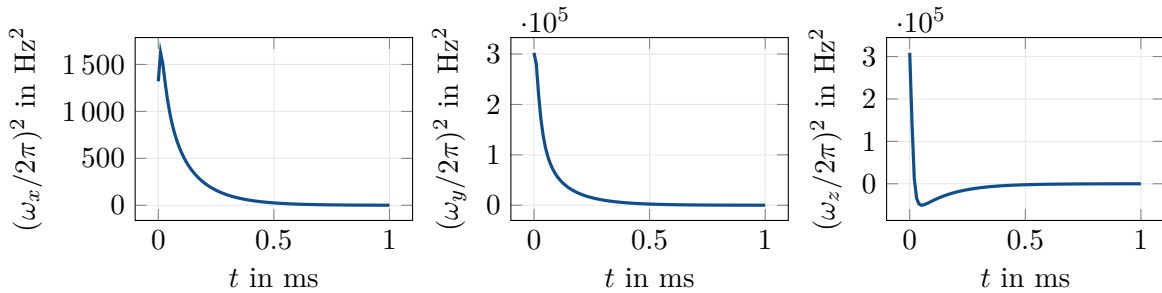


Figure 4.4: Simulated temporal change of trapping frequencies at the position of the initial trap after release for ^{41}K atoms. Initial currents $(I_x, I_y, I_z, I_{\text{SC}}, I_{\text{BC}}) = (-0.5, -1.41, 0.0, 2.0, 5.12)$ A. After release, the currents I_{SC} and I_{BC} drop to 0.0 A with the experimentally determined time constant $\tau = 140 \mu\text{s}$.

from experimental data.

Particle number

For simplicity, the atom numbers of ^{41}K are estimated by using the same assumptions for the optical transitions as for the ^{87}Rb atoms, most notably that of a closed two-level system [Rei07]. However, in case of ^{41}K , this is only a coarse approximation due to the narrow hyperfine splitting of ^{41}K (cf. fig. 2.12). During the detection pulse of $t = 18 \mu\text{s}$, atoms escape the detection transition by populating the state $P_{3/2} |F' = 2\rangle$ from where they might decay into the dark state $S_{1/2} |F = 1\rangle$. This effect could lead to a considerable underestimation of the detected atom numbers of ^{41}K and has not been quantified yet. To back up the atom numbers of ^{41}K with a more sophisticated model, one has to go through an in depth evaluation of the steady state solution of the optical Bloch equations for the ^{41}K multilevel system which presents a challenging numerical issue on its own. Experimentally, a reduction of fluorescence light should be observable for the duration of the detection pulse. From there, one could deduce the magnitude of this effect. For an optimal fit between theory and experiment, the predicted expansion curve for an atom number increased by 34% is shown in fig. 4.2 (blue line) and reproduces the observed data.

4.3 Collective excitations

In fig. 4.5 (left), the temporal evolution of the Thomas-Fermi radii of a ^{87}Rb BEC with $N = 2 \cdot 10^5$ condensed atoms is shown for two different cases: Solid lines represent the data set for an immediate trap switch-off after the evaporation has finished. Dashed lines show the expansion data if the BEC is hold for $t_{\text{hold}} = 0.6 \text{ ms}$ in the magnetic trap before it is switched off. The dependency of the Thomas-Fermi radii on t_{hold} suggests that the condensate is not in its motional ground state after evaporation. Indeed, varying t_{hold} for a fixed time of flight and measuring the Thomas-Fermi radii reveals a spectrum of excited collective modes. In fig. 4.5 (right), the discrete Fourier transform of the evolution of the Thomas-Fermi radii in y' -direction (the projection of the x - y -plane in the chip coordinate system onto the absorption camera) is shown.

Collective excitations of dilute Bose gases have been studied theoretically [Str96] and have been observed for various trap geometries and atomic species [Bis10; Edw96; For03; Jin96; Mar00a; Mew96; Str16]. In the conceptionally similar atom chip apparatus QUANTUS-2, quadrupole mode excitations were analyzed in detail [Cor18; Ste18] and are exploited for magnetic lensing to perform a three-dimensional collimation of ultracold ^{87}Rb ensembles [Dep21].

In a cylindrical trap elongated in x -direction with longitudinal and radial trap frequencies f_x and f_{\perp} , the lowest excitation frequencies f_Q and f_M depend on the trap aspect ratio $\lambda = f_x/f_{\perp}$ and are given as [Str96]

$$f_{Q,M}^2 = f_{\perp}^2 \left(2 + \frac{3}{2}\lambda^2 \pm \frac{1}{2}\sqrt{9\lambda^4 - 16\lambda^2 + 16} \right). \quad (4.13)$$

The plus-sign refers to the quadrupole mode f_Q where the radial and longitudinal axis of the BEC oscillate out of phase. The minus-sign determines the frequency of the monopole mode f_M , also referred to as the breathing mode where radial and axial components of the

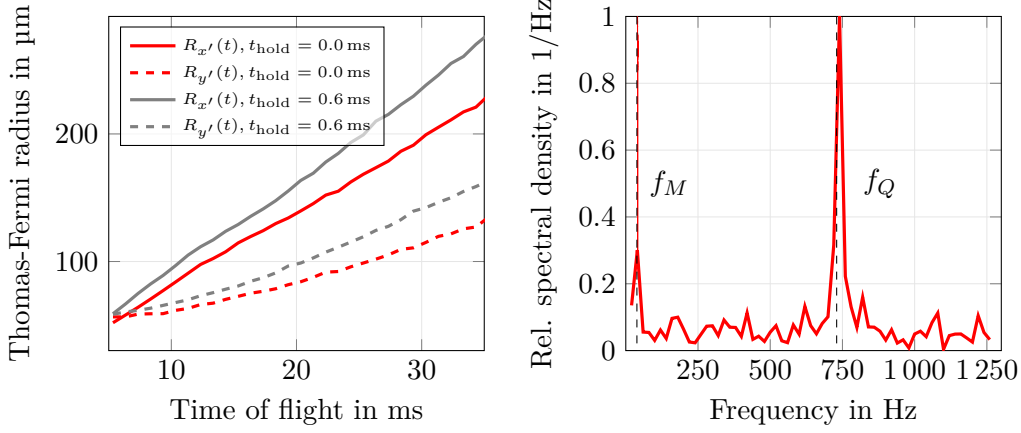


Figure 4.5: Left panel: Expansion curves of ^{87}Rb BECs with $N = 2 \cdot 10^5$ atoms released after two different holding times t_{hold} in the magnetic trap. Right panel: Discrete Fourier transform of $R_{y'}(t)$ for a fixed time of flight of 25 ms. The holding time t_{hold} is varied in the range from 0 to 50 ms, resulting in a frequency resolution of ± 10 Hz. Black dashed lines indicate the expected positions of the quadrupole (Q) and monopole (M) excitation modes at $f_Q = 730$ Hz and $f_M = 38.5$ Hz.

BEC oscillate in phase. In the here conducted experiments it is $\lambda \approx 0.0667$, which gives predicted excitation frequencies of $f_Q \approx 2.001f_{\perp}$ and $f_M \approx 0.105f_{\perp}$. The predictions which are based on experimentally extracted f_{\perp} are denoted as dashed lines in the excitation spectrum in fig. 4.5 and are in excellent agreement with the observed data.

The excitation sources of these collective modes were identified as the two decompression ramps during evaporative cooling (cf. ramps 4 and 6 in fig. 3.6). As shown in fig. 4.6, by omitting the second decompression ramp, the oscillation amplitude of the BEC after a time of flight of 25 ms due to the quadrupole mode was reduced by a factor of 3.9. The residual excitations are most probably excited during the first decompression ramp. With sigmoidal current ramps, these excitations are likely to be reduced further.

For ^{41}K BECs, no excitations were observed after repeating the same measurement as for ^{87}Rb . This behavior can be understood as mutual damping of motional excitations within thermal clouds of ^{41}K and ^{87}Rb after the decompression ramp. Since their trap frequencies differ by a factor of $\sqrt{87/41}$, any excitations would lead to a fast dephasing followed by damping due to the large positive scattering lengths. This damping effect also leads to a reduction of collective modes in the ^{87}Rb fraction, which is shown by the purple dots. Here, the ^{87}Rb ensemble is accompanied by a thermal ensemble of ^{41}K during evaporation. This offers a new method to suppress inadvertent excitations. Whether the mutual damping of excited two-component ensembles leads to an additional heating contribution has to be investigated in further studies. It is also conceivable that this heating might lead to higher thermal fractions of the mixed condensates.

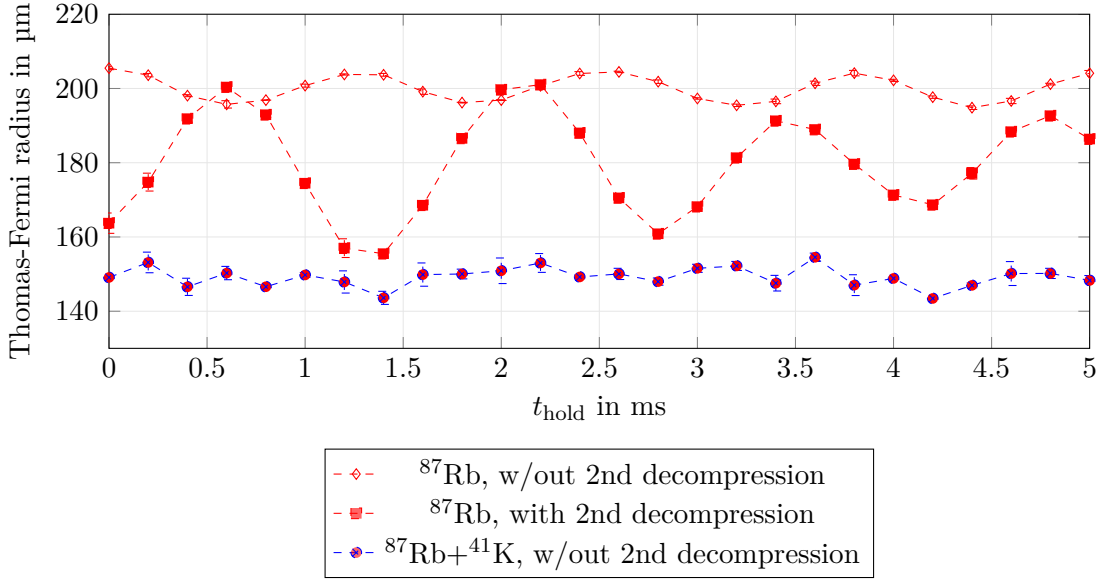


Figure 4.6: Thomas-Fermi radius $R_{y'}$ of ^{87}Rb BECs in dependence of the holding time t_{hold} in the magnetic trap before release after a time of flight of 25 ms. Red squares show the quadrupole mode oscillations of single species ^{87}Rb with the evaporation sequence shown in fig. 3.6. Red diamonds demonstrate a reduced oscillation amplitude, if the second decompression ramp is omitted. Purple dots show the remaining variation of $R_{y'}$, if ^{41}K is co-trapped during evaporation.

4.4 Free expansion of ^{87}Rb

With a method of mitigating collective excitations of ^{87}Rb at hand, the temporal evolution of the Thomas-Fermi radii of partially condensed ^{87}Rb ensembles is recorded. In the measurement shown in fig. 4.7, the amount of co-trapped ^{41}K atoms is adjusted by fixing the duration of the MOT to 1000 ms for ^{41}K and 500 ms for ^{87}Rb . This ensures that there is no observable BEC of ^{41}K altering the expansion behavior of ^{87}Rb . Still it is enough to prevent any collective excitations which has experimentally been verified by a variation of t_{hold} . The number of condensed ^{87}Rb atoms is estimated to $N_{\text{BEC}} = (0.98 \pm 0.04) \cdot 10^5$ atoms which is determined by a two-dimensional Thomas-Fermi fit above a Bose-enhanced Gaussian thermal background [Szc09] of $N_{\text{th}} = (1.89 \pm 0.04) \cdot 10^5$. For small time of flights, it is not possible to distinguish between thermal background and condensed fraction and most atoms are fitted mistakenly into the condensed fraction. Consequently, the Thomas-Fermi radii are overestimated for small and dense ensembles. Using the in-situ size of a thermal ensemble $r_{1,2,3} = \sqrt{2k_B T / m} \frac{1}{\omega_{1,2,3}}$ with temperature T [Ket99] and the conversion between the Thomas-Fermi radius and corresponding Gaussian width $R_{1,2,3} = \sqrt{7} r_{1,2,3}$ [Cor20], the magnitude of this error can be estimated. The solid black line indicates the resulting Thomas-Fermi radius for a thermal cloud of $T = 400$ nK mistakenly fitted by a Thomas-Fermi function in y' -direction.

Similar to section 4.2, three different simulated expansion curves are presented. The dotted gray line shows the theoretical prediction by assuming an immediate trap switch-off. This

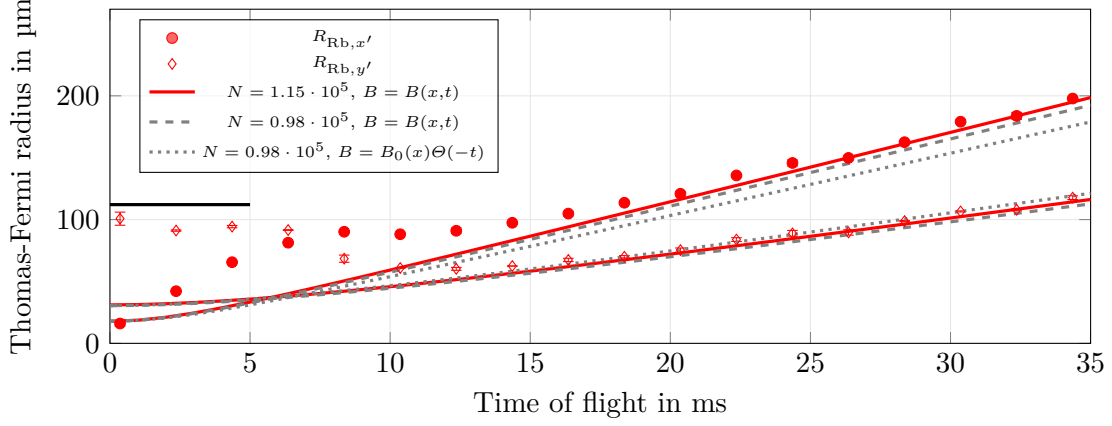


Figure 4.7: Temporal evolution of Thomas-Fermi radii of ^{87}Rb over two consecutive experimental runs. Solid dots show the expansion along the z -direction in the chip coordinate system, open diamonds the projection of the xy -plane onto the CCD sensor. Three different models based on equation (4.2) are shown: Dotted gray line shows the solution for an immediate switch-off of the magnetic field. Dashed gray line illustrates the simulated expansion with a magnetic field relaxation time constant of $\tau = 140 \mu\text{s}$. After increasing the atom number by 17%, the model reproduces the experimental data. Measured Thomas-Fermi radii below 20 ms are overestimated due to a faulty underestimation of the thermal fraction in the bimodal density distribution. Solid black line indicates the expected Thomas-Fermi radius from the fit of an in-situ thermal cloud of 400 nK projected onto the y' -axis.

leads to a severe underestimation of the Thomas-Fermi radii in x' -direction. By including the dynamic magnetic field relaxation of the trap frequencies based on the measurements in fig. 4.3, most of the mismatch is resolved. When the condensed particle number is increased by 17% (red solid curve), the experimental data is recovered which hints to a slight underestimation of ^{87}Rb atom numbers as well.

By using far red-detuned detection light, it is possible to determine the size of the ensemble for short times of flight. Yet, it is even possible to detect the in-situ size. For a pure ^{87}Rb condensate with $N_{\text{BEC}} = 3 \cdot 10^5$ condensed atoms, this method gives in-situ Thomas-Fermi radii of $R_{x'} = (16.5 \pm 0.4) \mu\text{m}$ and $R_{y'} = (36.0 \pm 0.8) \mu\text{m}$ which is close to the predicted values of $R_{x'} = 17.9 \mu\text{m}$ and $R_{y'} = 35.6 \mu\text{m}$. The measured values represent the average over 26 consecutive pictures with different t_{hold} to filter out the effect of collective excitations. Their oscillation amplitude is too small for being resolved by in-situ measurements, albeit present in the evaluated data. For higher contrast, the in-situ image data is smoothed with a Gaussian filter using a kernel of $\sigma = 1 \text{ px}$. Without filtering, high frequency diffraction patterns of the imaging beam complicate the analysis of atom shadows in the vicinity of the atom chip.

4.5 Gradient-free magnetic trap release of mixtures

To study mixture physics, it is of high importance to minimize differential forces during trap release. Due to the different mass of ^{41}K and ^{87}Rb while sharing the same magnetic moment, ^{41}K atoms always react more sensitive to magnetic field gradients compared to

^{87}Rb . In terms of kinematics, each species follows the center-of-mass trajectory $\mathbf{r}(t)$, given by the differential equation

$$\ddot{\mathbf{r}}(t) = -\frac{1}{m} \nabla (\boldsymbol{\mu} \cdot \mathbf{B}(\mathbf{r}, t)), \quad (4.14)$$

which results in different trajectories for both masses m for non-vanishing gradients of $\mathbf{B}(\mathbf{r}, t)$. Two possibilities to minimize magnetic field gradients during trap release can be considered. The first one is based on an adiabatic opening of the trap while keeping the magnetic field minimum at the same position. This can be achieved by simultaneously reducing the currents through the y-coil and the chip structures. In gravity, this method fails at the point where the heavy ^{87}Rb spills out of the trap while the lighter ^{41}K can still be held captive against gravity. To study the kinematics of mixtures on ground, we exploit an alternative method which relies on a variable time delay between the switch-off of the chip structures and the y-coil. The time constant of the y-coil $\tau_y = L/R \approx 1.6$ ms is much higher compared to the atom chip structures ($\tau = 140$ μs) due to its high inductance L and low resistance R . If the chip is switched off at times t_{off} after the switch-off of the y-coils, the time-dependency of the magnetic field gradient at the position of the atoms can be varied. To measure the differential accelerations during release given by eqn. (4.14), the z-positions of both isotopes after a preferably long time of flight for various t_{off} are imaged. The results of this measurement are shown in fig. 4.8. Each measurement has been done with a pure ensemble of either ^{41}K or ^{87}Rb to eliminate mutual interactions from affecting the trajectory. At $t_{\text{off}} = 77.4$ μs , both ensembles share the same center-of-mass z-position (x'-direction on the CCD) after a time of flight of 20 ms which demonstrates that a trap release without additional forces due to magnetic field gradients is possible on ground. The exact value of t_{off} might vary for magnetic traps in microgravity or for different atom chip orientations with respect to gravity due to slightly shifted trap minima.

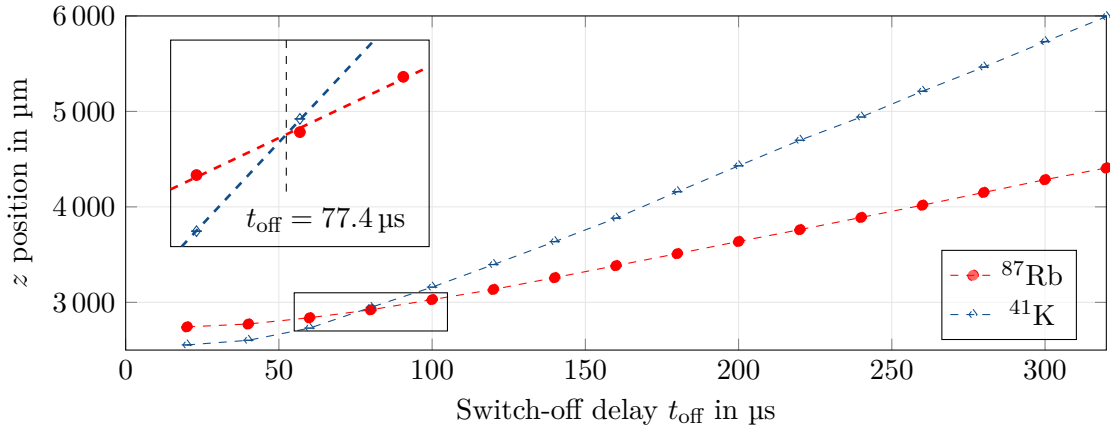


Figure 4.8: z-position of either ^{87}Rb (red) or ^{41}K (blue) BECs after time of flight of 20 ms in dependence of a switch-off delay t_{off} between y-coil and chip structures. The inset shows the intersection of both curves which are locally approximated by linear fits. A delay of $t_{\text{off}} = 77.4$ μs allows for a trap release without magnetic gradients.

The y' -position of the ensembles is unaffected by t_{off} and varies less than $5 \mu\text{m}$ over the examined parameter range. For technical reasons¹ we set the parameter to $t_{\text{off}} = 80 \mu\text{s}$ for the following measurements.

4.6 Influence of gravity on immiscible BECs in cylindrical traps

In absorption images of mixed ^{41}K - ^{87}Rb BECs (cf. fig. 3.9, right panel), the effect of their mutual interaction is clearly visible by the deformation of the respective density distributions which does not reflect the symmetry of the trapping potential. Similar observations for quantum degenerate mixtures with large positive interspecies scattering lengths a_{ij} have been made in other experiments using ^{41}K - ^{87}Rb [Bur18], ^{39}K - ^{87}Rb [Wac15], ^{87}Rb - ^{133}Cs [McC11], ^{87}Rb - ^{23}Na [Wan15], ^{87}Rb - ^{87}Rb [Pap08] or ^{166}Er - ^{164}Dy [Tra18]. For quantum gas mixtures, the criterion for their miscibility is determined by their ratio of interspecies to intraspecies interactions Δ , given by $\Delta = \frac{g_{\text{Rb-K}}}{\sqrt{g_{\text{Rb-Rb}}g_{\text{K-K}}}}$ with the coupling constants $g_{ij} = 2\pi\hbar^2 a_{ij} \frac{m_i+m_j}{m_i m_j}$, assuming $a_{ij} > 0$. If the interspecies interaction dominates, it is $\Delta > 1$ and the mixture is in the immiscible regime. For $\Delta < 1$, the interaction within each species dominates and the condensates are in the miscible regime where they overlap to some extent [Rib02]. In our case, it is $\Delta \approx 2.3$ which makes up an immiscible two-component BEC. The ground state of this mixture in microgravity has been calculated for an isotropic trap [Cor20] and shows a ^{87}Rb BEC nested into a spherical shell of ^{41}K . In our experiments, however, the situation is more complex due to the gravitational sag and cylindrical traps which break the spherical symmetry of an isotropic trap in microgravity. Due to the rotatable mounting of the base plate in the experimental rack the whole vacuum chamber can be rotated around the x-axis (cf. rotational axis in fig. 2.1). This gives the possibility to study the influence of gravity on trapped BEC mixtures. Since the x-axis nearly coincides with the weak trapping axis, gravity always points along one of the strong trapping axes along radial direction. Thus, for any rotation angle α along the x-axis, it is possible to keep the atoms trapped. In fig. 4.9, mixed condensates are shown for different rotation angles α between the direction of gravity and z-axis of the chip coordinate system. The ^{41}K and ^{87}Rb ensembles are detected separately in two consecutive experimental runs, colored and overlaid afterwards. Due to instabilities in the z-coil current which became apparent later, the center position of each ensemble in x' -direction in this measurement series was subject to shot-to-shot variations with a standard deviation in the range of $50 \mu\text{m}$ after a free expansion of 25 ms. In future experiments we plan to include the detection of both ensembles in a single experimental run by using either fast frame transfer on the CCD chip [Har08; Sch18] or by exchanging the camera with a CMOS based sensor featuring frame rates up to the kHz regime. However, the following conclusions can already be drawn from the absorption pictures:

- The relative gravitational sag between both isotopes along z-direction given by eqn. (3.9) in the release trap with $\omega_z = 2\pi \cdot 347 \text{ Hz}$ (for ^{87}Rb) is only $1.1 \mu\text{m}$. This is

¹ Each sequence step has to be a multiple of $20 \mu\text{s}$ at the time of writing this thesis. This can ultimately be reduced to steps of $4 \mu\text{s}$ which is the update rate of the DDS cards. Smaller time steps would entail a dephasing of DDS signals to other output channels.

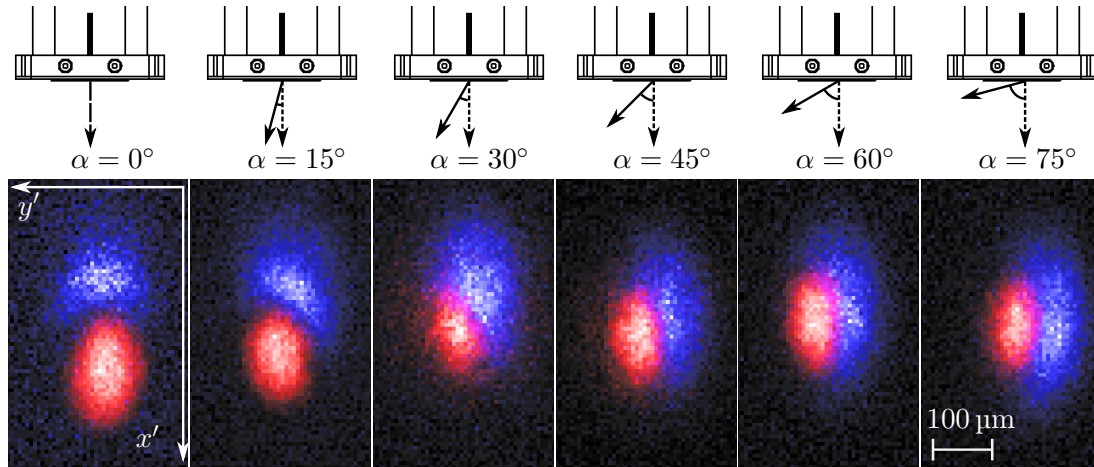


Figure 4.9: False-color image of two-component ^{41}K (blue) and ^{87}Rb (red) condensates after free expansion of 25 ms for different atom chip orientations with respect to gravity. Direction of gravity is indicated with the solid black arrow which is tilted by α with respect to the z -axis. For better visibility, both ensembles are normalized before the images are overlapped. Atom numbers vary between $N_{\text{Rb}} \approx (0.8 - 1.3) \cdot 10^5$, $N_{\text{K}} \approx (3.5 - 6.0) \cdot 10^4$.

much less than the observed separation of the two ensembles after free expansion. We contribute this additional separation to the mutual repulsion of the ensembles directly after release.

- The trapped ^{87}Rb atoms are pulled stronger towards the direction of gravity due to their higher mass. This orientation is maintained during free expansion.

In collaboration with the theory group of Naceur Gaaloul we strive to model the observations with a full simulation of the strongly interacting mixture including gravity and realistic trap properties. Fig. 4.10 shows the numerical solution of coupled Gross-Pitaevskii equations for the ground state of a ^{41}K - ^{87}Rb quantum mixture in a cylindrical trap with eigenfrequencies of $\omega_{x,y,z,\text{Rb}} = 2\pi \cdot (25.5, 202, 202)$ Hz. The trap configuration corresponds to the currents $(I_x, I_y, I_z, I_{\text{SC}}, I_{\text{BC}}) = (-0.5, -1.08, 0.0, 2.0, 5.12)$ A in our experiment. The graphs show the normalized densities of the BEC wavefunctions integrated along y -direction $|\Psi_{\text{K,Rb}}(x,z)|^2 = \int dy |\Psi_{\text{K,Rb}}(x,y,z)|^2$ for ^{41}K (blue) and ^{87}Rb (red) with gravity pointing along z -direction (upper graph) and in microgravity (lower graph). The trap potentials for both isotopes and gravity configuration are calculated with the gauged magnetic field simulation and subsequently fed into the coupled Gross-Pitaevskii equations. These are solved numerically by the split-operator method [Fei82] to find the ground state of the system.

We observe fundamentally different ground states for both situations:

- In gravity, $|\Psi_{\text{Rb}}(x,z)|^2$ is shifted downwards by $3.28 \mu\text{m}$ compared to the ^{41}K atoms. This corresponds to the expected relative gravitational sag (cf. eqn. (3.9)) of the trapping potentials and is not increased further due to their mutual repulsion. The

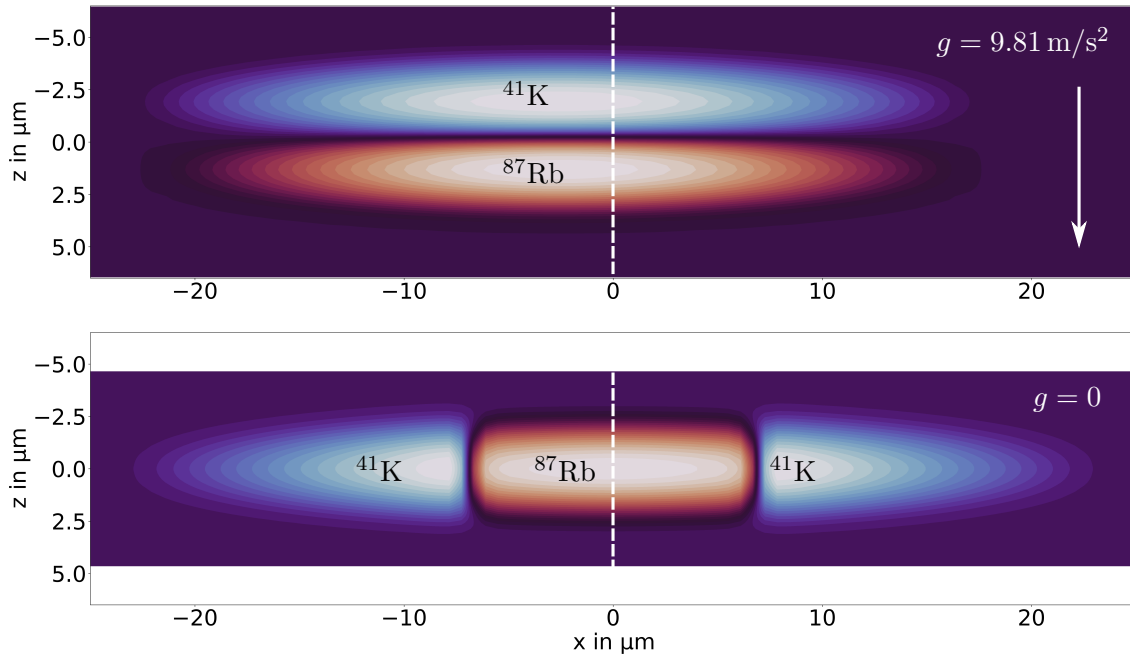


Figure 4.10: Ground states of ^{41}K (blue) and ^{87}Rb (red) in a cylindrical trap with frequencies $\omega_{x,y,z,\text{Rb}} = 2\pi \cdot (25.5, 202, 202)$ Hz in gravity (upper graph) and microgravity (lower graph). Simulated grids contain (64,64) and (128,64) points, respectively. $N_{\text{K}} = N_{\text{Rb}} = 3.5 \cdot 10^4$ atoms, $a_{\text{KRb}} = 165.3a_0$. Simulations by Annie Pichery.

shift of the center-of-mass positions in negative x-direction is due to a slight tilt of the longitudinal trapping axis with respect to gravity.

- In microgravity, both wavefunctions arrange axially symmetric along the weak longitudinal trapping axis. Still, there is no overlap between them which reflects their immiscible nature. In striking contrast to the isotropic trap configuration [Cor20], there is no shell structure visible but a bipartite separation of the ^{41}K -BEC wavefunction with the ^{87}Rb -BEC in the center. This can be understood in terms of energy minimization: For the ^{41}K atoms, it is more favorable to arrange along the weak trapping axis compared to the strong radial directions.

Future simulations will investigate the expansion dynamics of the immiscible state in elongated traps and allow predictions for our experiments in microgravity. Also, the stability characteristics of the bipartite mixture are of interest to estimate the influence of experimental imperfections. The partition of the ^{41}K -BEC might lead to previously unobserved interference effects which will be explored in further studies.

4.7 Summary and perspectives

Microgravity campaign

The insights presented in this chapter will find application in the sounding rocket missions MAIUS-2 and -3. The discussed influence of transient magnetic fields during switch-off of

atom chip currents has to be taken into account in proposed magnetic lens protocols and release traps as well as in post-flight data analysis.

One of the unique possibilities of the planned sounding rocket missions is the investigation of interacting quantum mixtures in their undisturbed ground state. MAIUS-B allows to prepare strongly interacting quantum mixtures of ^{41}K and ^{87}Rb in cylindrical traps with controllable frequency aspect ratio [Her13] leading to a partition (see fig. 4.10) ^{41}K BECs or even shell-like structures for lower aspect ratios [Cor20; Sun18]. In the campaigns MAIUS-2 and -3, mixtures will be generated for traps with different frequency aspect ratios and observed after free expansion. These experiments are prepared and backed up by further numerical studies to explore mixture ground states for varying aspect ratios. Also, the expansion dynamics and robustness of the quantum mixture to experimental imperfections are currently under investigation.

To access long expansion times of mixed or single species ensembles offered by microgravity, a trap release without magnetic field gradients is important (cf. fig. 4.8). Such force-free release is also needed to interpret relative center-of-mass positions for interacting mixtures but on the other hand requires an optimization of switch-off delays between y-coil and chip structures for each release trap. Due to the limited microgravity time, compromises between experimental performance, accuracy and the number of considered release traps have to be made here.

The mutual damping of collective excitations should also be present in microgravity. Indeed, due to the enhanced two-body collision rates of ultracold mixtures in microgravity (see tab. 3.2), damping effects are expected to increase accordingly. They could ease the requirements and enhance the robustness of a two-species magnetic transport by damping residual excitations in the target trap. To examine this yet unobserved effect in microgravity, the collective excitations of a simultaneously transported mixture into a distant and weak trap have to be analyzed and compared with a single species transport of ^{87}Rb , analogously to the measurement presented in fig. 4.6. As discussed in sec. 5.1, protocols for a fast two-species transport have not been proposed yet [Cor18] pointing out the need of further experimental and theoretical research on this topic.

Conclusion

The free expansion of single BECs of ^{41}K and ^{87}Rb released from a magnetic trap has been analyzed in detail, experimentally and theoretically. To simulate the expansion curves, we evaluated the scaling approach for both isotopes with their respective trap frequencies, scattering characteristics and atom numbers. Assuming an immediate switch-off of the magnetic fields results in a systematic underestimation of the Thomas-Fermi radius along z-direction (x' -direction in the detection coordinate system) which coincides with the high frequency radial trapping direction. By microwave spectroscopy, we were able to directly measure the actual time constant of the magnetic field decay at the position of the atoms. Reevaluating the scaling approach with this dynamic switch-off explains the observed disagreement between the simplified scaling theory and experiment. Furthermore, the results point towards an underestimation of the detected atom numbers, especially for ^{41}K . We observed collective excitations in the release trap for single BECs of ^{87}Rb and could identify the frequencies of the monopole and quadrupole modes in excellent agreement

with the predicted values. An excitation source was found in the decompression ramps during microwave evaporation. When ^{41}K is added to the trap, the collective oscillations damp out and are not detectable anymore. This is interpreted as the result of dephasing and mutual interactions of both species which lead to a fast damping of excitations.

We investigated the possibility of a trap switch-off without inducing additional forces due to magnetic field gradients to the ensembles. By adding a time delay between the switch-off of the y-coil and the chip structures we have found a convenient method to eliminate differential accelerations between both isotopes during release. This allowed us to observe the influence of their mutual interaction during expansion. Finally, we were able to change the direction of gravity with respect to the atom chip and observe its influence on the mixture.

CHAPTER 5

Summary and Outlook

With the successful production of a quantum mixture of ^{41}K and ^{87}Rb on a compact atom chip device capable of sounding rocket flights, the ground has been prepared for differential matter wave interferometry with ultracold atoms in space. The apparatus commissioned in the scope of this thesis extends the established combination of a high-flux 2D-MOT and fast BEC generation with an atom chip to a second species, ^{41}K . Its performance regarding condensed atom numbers is on par with state-of-the-art mixture experiments and its repetition rate makes it especially attractive for microgravity platforms with limited cycle time.

With the in-depth analysis of the BEC expansion of ^{41}K and ^{87}Rb , the simple scaling approach has been extended to include transient magnetic fields during atom release. This extension presents a valuable tool to reliably predict the spatial and momentum evolution of the ensembles. For mixtures, it has been shown that collective excitations of the ensembles are efficiently damped out by their mutual interaction. Knowing that the mixture is in its ground state of motion simplifies the follow-on steps for preparing the interferometry input state.

In this chapter, the follow-on steps needed for matter wave interferometry at long time scales are briefly discussed for the mixture case, namely transport, collimation and internal state preparation. Finally, first beam splitters using Raman double diffraction with ^{87}Rb are presented as an outlook. The chapter closes with a summary of the results of this thesis.

5.1 Transport

The fast generation of ultracold mixtures of ^{41}K - ^{87}Rb described in this thesis relies on high thermalization rates which are only present in steep magnetic traps close to the atom chip's surface. The distance between the condensed ensembles to the conducting z-structure Science chip is initially only about $315\ \mu\text{m}$. Using this configuration for atom interferometry would introduce several technical issues. Among these are:

- The expansion of the ensembles during the interferometry sequence limits the maximum pulse separation time T . Parts of the ensemble expanding out of the interferometry region or reaching the chip surface are obviously not available for phase read out. Keeping the distance to the chip surface high allows for longer expansion times of the atomic ensembles.
- The interferometry beams are applied at a distance of $2.5\ \text{mm}$ parallel to the chip surface and have a waist of $2.7\ \text{mm}$ at $1/e^2$ level [Mis20]. To minimize the influence

of dipole forces due to intensity gradients the pulses have to be applied to ensembles which are centered at the interferometry beam axis. Additionally, parts of the incoming beam are diffracted on the atom chip surface which leads to an intensity modulation with increasing frequency for higher distances to the atom chip [Lac20].

For these reasons, the atoms have to be moved away from the atom chip. In the discussed setup under presence of gravity, this is naturally achieved by a free fall along z-direction. However, in microgravity the transport has to be initiated by a controlled movement of the trap position away from the chip. For single species atom chip experiments, different transport strategies based on current ramps of the y-coils are conceivable. A nearly adiabatic ramp which slowly transports the ensemble is not practical due to continuous heating stemming from fluctuations of the chip currents: Technical and fundamental current noise in the conducting chip wires resonant to the trapping frequencies leads to heating of the ensembles. The heating rate caused by technical current noise scales according to $\propto d^{-2}$ with the ensemble distance d to the chip wire [Bar21; Fol02].

The transferred heat can be minimized by using non-linear transport ramps based on shortcut-to-adiabaticity protocols which allow a fast and robust magnetic transport over a distance of more than a millimeter during 75 ms [Cor18]. They strongly suppress residual trap oscillations compared to other ramps of the same duration. By employing transport ramps based on optical control theory, it is even possible to recover the ensemble ground state in the target trap [Amr19].

Up to now, only limited research has been conducted for appropriate two-species transport protocols. Due to their different mass, the trap frequencies for both species are naturally different which complicates the prediction of a common transport ramp. Optimal control theory-based solutions should however exist. Experimentally, a further possible solution is given by the (non-adiabatic) transport of a thermal mixture into an optical dipole trap (ODT) at the desired target position followed by optical evaporation to prepare the ultracold mixture in its ground state. As shown in fig. 3.13, the thermalization timescale for an ODT in microgravity is more than two orders of magnitude shorter at the onset of quantum degeneracy compared to ground-based operation. Any excited collective modes in the ODT will presumably be damped out by interspecies interactions, as shown in section 4.3. This approach naturally allows for efficient two-species delta-kick collimation which also involves an ODT.

5.2 Delta-kick collimation

Techniques of exploiting optical or magnetic potentials to collimate expanding atomic ensembles are widely used in matter wave experiments [Amm97; Chu86]. Devices with atom chips benefit from the fast switching of magnetic potentials and have demonstrated unmatched expansion rates down to the pico-Kelvin level in microgravity campaigns [Dep21; Mün13]. Optical potentials typically offer the most rapid switching times by using acousto-optical modulators. By using versatile switching devices like acousto-optical deflectors, also the position and shape of the potentials can be tuned by painting time-averaged optical potentials [Alb20a]. Both schemes are also successfully applied in combination [Kov15]. Simultaneous collimation of two different atomic species has been demonstrated solely for

isotopes of the same element yet, like ^{85}Rb - ^{87}Rb [Ase20]. Since the trapping frequency of a species is related to its mass via $\omega \propto m^{-1/2}$, it is generally not possible to collimate two different isotopes with a single lens. Additionally, interspecies interactions come into play and lead to deformations of the trapped and released wave packets.

The most promising route to overcome these challenges for mixtures of ^{41}K - ^{87}Rb is opened by transferring it into an ODT after magnetic transport. This allows to arbitrarily modify the magnetic background field and tune the interspecies scattering lengths to $a_{\text{K,Rb}} = 0$ by exploiting the zero crossing of a Feshbach resonance around $B = 72 \text{ G}$ [Sim08; Tha08]. To access the resonance, both ensembles have to be prepared in the lowest Zeeman state $|1,1\rangle$ by microwave state preparation (see also 5.3). As the interspecies interactions are tuned to zero, the two-species ground state is given by two overlapping single BECs. After using two consecutive optical lenses conceptually similar to an achromatic doublet, both species can be collimated to three-dimensional temperature equivalents of 15 pK , as predicted by simulations of coupled Gross-Pitaevskii equations [Cor20].

It is possible to extend the physics package of MAIUS-B by a single beam optical dipole trap with minor modifications. Also a crossed optical dipole trap, as required by the theoretical studies, is conceivable. Since the optical alignment and mode match between magnetic transport and optical trap is non-trivial and requires potentially many optimization steps, this would ideally be suited for campaigns on microgravity platforms such as drop towers or the recently commissioned Einstein elevator [Lot20].

During ground-based measurements with limited free fall times, we successfully demonstrated single magnetic lenses for ^{87}Rb and for the first time also for ^{41}K . For this lens, the atoms are initially released into free fall for 3 ms . During this time, the y-coils are switched to a current of $I_y = -0.6 \text{ A}$ to generate the offset field needed for magnetic lensing with the z-structure of the Base chip. After the ensembles have moved to the new position and

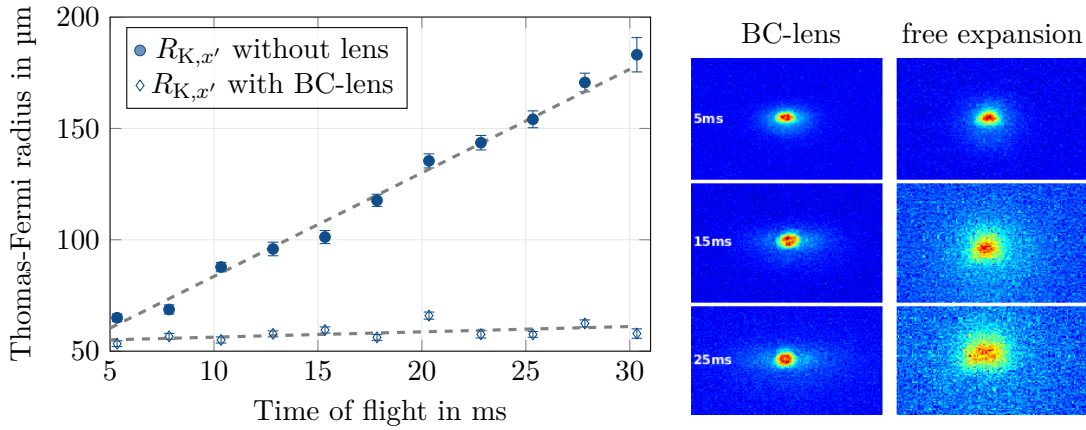


Figure 5.1: Left: Evolution of Thomas-Fermi radius in z-direction for a collimated and non-collimated BEC of ^{41}K . Dashed lines are linear fits to obtain the momentum widths of the ensembles. $\Delta p_z = (0.366 \pm 0.014)\hbar k$ for non-collimated, $\Delta p_z = (0.019 \pm 0.009)\hbar k$ for collimated ensemble. Right: Absorption images at different times of flight in comparison. $N_{\text{BEC}} = 1.8 \cdot 10^4$, $N_{\text{thermal}} = 4.4 \cdot 10^4$.

the Thomas-Fermi radii expanded accordingly, the Base chip is switched on with a current of $I_{BC} = 6.0$ A for a lens duration of $t_{\text{lens}} = 0.18$ ms for ^{41}K ($t_{\text{lens}} = 0.40$ ms for ^{87}Rb). This creates a cylindrical lens at the condensate position which collimates the momentum in y- and z-direction. In fig. 5.1, an expansion curve of magnetically collimated ^{41}K BECs is shown in comparison to the non-collimated case. The momentum width in z-direction is reduced by a factor of almost 20 to $\Delta p_z = (0.019 \pm 0.009)\hbar k$ in units of the photon recoil at 767.7 nm.

5.3 State preparation

Atoms with non-zero magnetic moment experience an energy shift of their internal states due to the Zeeman effect. Magnetic field gradients shift the accumulated phase in both interferometer arms and add up to a differential phase which alters the output state of the interferometer. Additionally, the resonance frequencies of Raman transitions change according to the Zeeman shift. It is therefore favorable to transfer all atoms into a non-magnetic state before interferometry. For the alkalines ^{41}K and ^{87}Rb , that is either $|F = 1, m_F = 0\rangle$ or $|F = 2, m_F = 0\rangle$. For atom chip experiments working with a single species, this is conveniently done by an adiabatic rapid passage (ARP) using radiofrequency fields [Abe17; Lac20; Ste18] and a quantization magnetic field. During an ARP, the atoms are dressed with radiofrequency or microwave fields, which frequencies are adiabatically ramped over the target state resonance [Cam84]. After the frequency ramp, ideally all atoms are transferred into the target state. This approach is stable against external perturbations shifting the resonance frequency or instabilities of the field intensity and is thus more robust than a direct transfer using resonant π -transitions.

For mixtures, it is necessary to manipulate the internal states of both species separately. Since the Zeeman shifts of ^{87}Rb and ^{41}K are equal, this is not possible with radiofrequency fields. We circumvent this issue by using microwave ARPs resonant to the $|F = 2\rangle \leftrightarrow |F = 1\rangle$ transitions of ^{41}K around 254 MHz and ^{87}Rb around 6834 MHz. The first ARP thus transfers the atoms from $|F = 2, m_F = 2\rangle \rightarrow |F = 1, m_F = 1\rangle$, followed by a second ARP which transfers them into the non-magnetic target state $|F = 1, m_F = 1\rangle \rightarrow |F = 2, m_F = 0\rangle$.

Using this scheme, we have demonstrated transfer efficiencies of 91.8% for both ARPs for ^{87}Rb [Mis20] by using the microwave source shown in fig. 3.5. This is comparable to the optimized transfer efficiency of a radiofrequency ARP [Ste18]. The transfer in our setup is optimal for distances up to 2 mm from the microwave structure on the Base chip and a microwave power of 20 dBm. For larger distances, either the microwave power or the duration of the ARP have to be increased to maintain the high performance.

5.4 Interferometry

One of the major goals of MAIUS-B is to perform atom interferometry on ^{87}Rb and ^{41}K using double diffraction based on stimulated two-photon Raman transitions [Lev09]. A schematic of this diffraction process is depicted in fig. 5.2. Two incident laser beams with frequencies ω_1 and ω_2 and parallel polarization pass a $\lambda/4$ -plate and are retroreflected by a mirror which serves as an inertial phase reference. The polarizations of the reflected beams are rotated by 90° with respect to the incoming beams. The beams are tilted by 6°

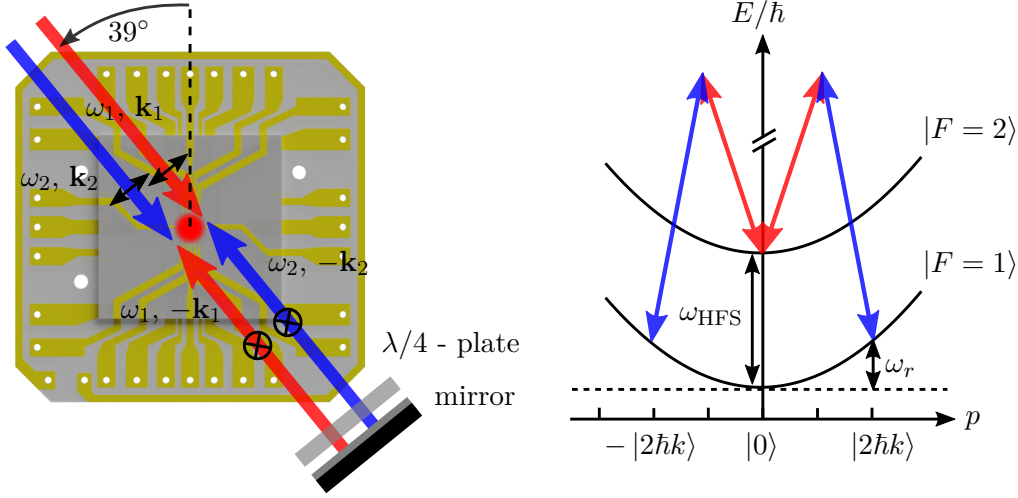


Figure 5.2: Left: Beam configuration used in the MAIUS-B apparatus. The incoming beams have frequencies of $\omega_{1,2}$, wave vectors $\mathbf{k}_{1,2}$ and parallel polarization. They are retroreflected on a mirror and pass a quarter-wave plate twice which rotates the polarization by a total of 90° . The beams are rotated by 6° to the diagonal axis in order to prevent the formation of standing waves between the vacuum viewports. Right: Double diffraction based on symmetric two-photon Raman transitions. The parabolas indicate the dispersion relation of the atomic states $|F = 2\rangle$ and $|F = 1\rangle$, separated by the hyperfine splitting ω_{HFS} . Two-photon diffraction shifts the energy by the recoil frequency ω_r .

from the diagonal axis to prevent the formation of standing waves due to reflections on the vacuum viewports¹. The frequencies ω_1 and ω_2 are tuned to fulfill the condition for Raman diffraction (fig. 5.2 right)

$$\Delta\omega := \omega_2 - \omega_1 = \omega_{\text{HFS}} - \omega_r + \omega_{\text{AC}}, \quad (5.1)$$

where ω_{HFS} denotes the hyperfine splitting of the ^{87}Rb or ^{41}K ground states and ω_{AC} the differential two-photon light shift of the atomic states due to the off-resonant light field. The recoil shift ω_r accounts for the momentum gain of the coupled states due to absorption and emission of photons with momenta $\hbar\mathbf{k} = \hbar|\mathbf{k}_{1,2}|$:

$$\omega_r = \frac{2\hbar k^2}{m} \quad (5.2)$$

with atomic mass m . Since the atoms are at rest with respect to the reflecting mirror, this diffraction scheme couples the initial state $|F = 2, p = 0\rangle$ symmetrically with the states $|F = 1, p = \pm 2\hbar k\rangle$ and the atoms undergo Rabi oscillations with Rabi frequency Ω_{eff} . In the Mach-Zehnder configuration of an atom interferometer based on Raman double diffraction, the atoms are initially prepared in the state $|F = 2, p = 0\rangle$. From here, they

¹ The faces for sealing of the viewports on the vacuum chamber are not skewed for opposite windows.

are transferred to the state $|F = 1, p = \pm 2\hbar k\rangle$ by a beam splitting pulse with duration $\tau_s = \pi/(\sqrt{2}\Omega_{\text{eff}})$. After a free evolution time T , a mirror pulse with duration $\tau_m = 2\tau_s$ redirects the wave packets without changing the internal state. Once the wave packets overlap after an additional time T , the interferometer is closed by applying another τ_s -pulse. Similar to interferometers based on Raman single diffraction [Kas91], the output ports of the interferometer are read out by detecting the ratio of internal states via state selective fluorescence imaging [Sch14b]. By varying the pulse separation T , the phase-shift between the output ports is given by $\Delta\Phi = 2(\mathbf{k}_1 - \mathbf{k}_2) \cdot [\mathbf{a} - 2\mathbf{v} \times \boldsymbol{\Omega}] T^2$ to lowest order in T and depends on the acceleration \mathbf{a} , the rotation rate $\boldsymbol{\Omega}$ and velocity \mathbf{v} of atoms in the laboratory frame [Can06]. The prefactor of 2 accounts for the enhanced interferometer space-time area of the symmetric configuration.

Due to its symmetric structure, this interferometer is inert against systematic effects like magnetic field fluctuations or two-photon light shifts. Also, phase fluctuations of the light fields cancel out due to the retroreflected configuration [Lev09].

In contrast to Bragg double diffraction [Ahl16; Gie13], the use of Raman transitions in the interferometer allows to keep track of imperfect beam splitters and mirrors by blowing away non-diffracted atoms in-between the pulses. This simplifies the analysis of the interferometer output phase since the non-diffracted parts would otherwise enter the detected output port. On a technical level, the implementation of Bragg diffraction is less challenging since the frequency difference of the two light fields for the Bragg transitions are in the range of 1 MHz and can easily be generated from a single laser. To ensure the demands on the phase stability of the Raman lasers while maintaining the compatibility to the flight system, a full digital phase lock has been developed [Pap17].

Using the MAIUS-B ground testbed we succeeded in implementing a beam splitter based on Raman double diffraction for ultracold ^{87}Rb atoms (see fig. 5.3). In future work, we will

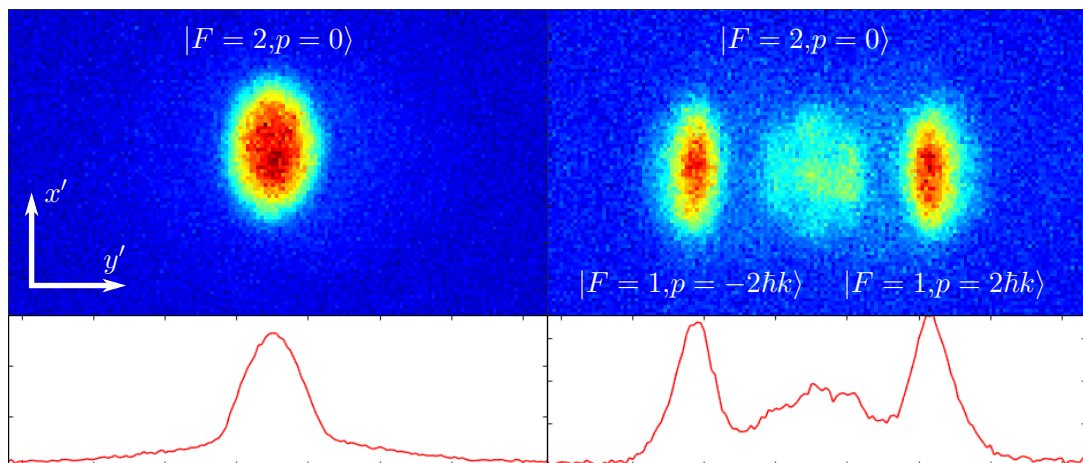


Figure 5.3: Absorption image of Raman double diffraction beam splitter with a non-collimated BEC of ^{87}Rb . $N = 1.1 \cdot 10^5$, $N_{\text{th}} = 1.1 \cdot 10^5$. Duration of $\pi/2$ box pulse is 160 μs . To detect the diffracted parts, a short pulse with repumper light is applied before imaging. Diffraction efficiency is 67%.

complete the interferometry sequence and demonstrate its functionality by implementing a quantum tiltmeter [Ahl16]. Ultimately, we plan to implement a correlated phase read out with ^{41}K and ^{87}Rb to be able to perform a UFF test [Var09].

5.5 Conclusion

Transferring the demands of a two species BEC atom interferometer into a compact apparatus which withstands the harsh conditions during a sounding rocket flight is an arduous task and presents a significant technological leap on the limits of what is feasible. This thesis deals with the setup and commissioning of the physics package with a home-built laser and electronics system resulting in the generation of quantum degenerate mixtures of ^{41}K and ^{87}Rb with record-breaking repetition rates.

By the addition of a second atomic species, the new system represents a significant advancement compared to established atom chip experiments QUANTUS-2 and MAIUS-A. The apparatus is based on the time-proven two-chamber design with a new source chamber for simultaneous operation of a ^{41}K and ^{87}Rb 2D-MOT. The oven based atom source enables higher MOT loading rates compared to other two-species chip experiments using ^{40}K - ^{87}Rb [Aub05; Ext06] or $^{39/41}\text{K}$ - ^{87}Rb [Ell18] which are based on dispenser sources.

After loading of the atoms into the magnetic trap, ^{87}Rb is evaporated by using a two-frequency microwave knife and ^{41}K sympathetically cooled to quantum degeneracy. The complete evaporation process lasts about 2.2 s and is able to generate BEC mixtures of ^{41}K and ^{87}Rb with tunable number ratios and up to $6 \cdot 10^4$ ^{41}K or $3 \cdot 10^5$ ^{87}Rb atoms in single-species operation. Together with the fast MOT loading rate, this enables the generation of a BEC mixture every 3.4 s which is, to the best of our knowledge, the fastest reported repetition rate for any quantum degenerate two-species experiment.

Sympathetic cooling relies on the spatial overlap of the thermal clouds of both species which itself depends on the ensemble temperature, trap frequencies and the differential gravitational sag. Based on our simulations of thermalization rates, we expect enhanced sympathetic cooling in microgravity especially for ultralow temperatures on the onset of quantum degeneracy. This is due to the absence of the gravitational sag which improves the spatial overlap of both ensembles and supports the efficient generation of BEC mixtures in microgravity.

The free expansion of single BECs of ^{41}K and ^{87}Rb has been analyzed in detail and revealed novel insights into the release dynamics of chip experiments and the mutual influence of mixtures on collective excitations: To correctly match the expansion of the released BECs, the time-dependency of the magnetic field decay on the position of the atoms has to be taken into account. This knowledge will help to predict and model the BEC expansion in microgravity and helps to transfer atom dynamics simulations to our experiment. Additionally, collective excitations were identified to further complicate the analysis of ^{87}Rb BECs expansion in single-species operation. In contrast, collective excitations of mixed ^{41}K and ^{87}Rb are strongly suppressed due to their mutual interaction. This gives novel perspectives for a two-species magnetic transport and eases the requirements on the purity of the target state.

We studied the free expansion of strongly interacting mixtures of ^{41}K and ^{87}Rb BECs for different orientations of gravity which will give helpful insights for mixture simulations and

demonstrates the versatility of the apparatus.

The sounding rocket missions MAIUS-2 and -3 build upon the findings of this thesis and will transfer some of the here discussed key experiments into microgravity. Among these are the fast generation of quantum mixtures of ^{41}K and ^{87}Rb with different mixing ratios and an analysis of their ground states and expansion dynamics in weightlessness. A magnetic transport of the mixture to the center of the interferometry beams and subsequent state preparation into the non-magnetic state allow for matter wave interferometry. By extracting the differential phase of the two-species atom interferometer [Bar15; Bar16] a first quantum test of the WEP in space is conceivable within the framework of MAIUS-3.

Bibliography

- [Aas15] AASI, J. et al.: ‘Advanced LIGO’. *Classical and Quantum Gravity* (Mar. 2015), vol. 32(7): p. 074001 (cit. on p. 1).
- [Abb16] ABBOTT, B. P. et al.: ‘Observation of Gravitational Waves from a Binary Black Hole Merger’. *Physical Review Letters* (Feb. 2016), vol. 116(6) (cit. on p. 1).
- [Abe17] ABEND, SVEN: ‘Atom-chip gravimeter with Bose-Einstein condensates’. PhD thesis. Gottfried Wilhelm Leibniz Universität Hannover, 2017 (cit. on p. 80).
- [Ada18] ADAMSON, PHIL, SWAPAN CHATTOPADHYAY, JONATHON COLEMAN, PETER GRAHAM, STEVEGEER, RONI HARNIK, STEVE HAHN, JASON HOGAN, MARK KASEVICH, TIM KOVACHY, JEREMIAH MITCHELL, ROB PLUNKETT, SURJEET RAJENDRAN, LINDA VALERIO, and ARVYDAS VASONIS: ‘PROPOSAL: P-1101. Matter-wave Atomic Gradiometer Interferometric Sensor(MAGIS-100)’. (2018), vol. (cit. on p. 2).
- [Agu14] AGUILERA, D. N. et al.: ‘STE-QUEST—test of the universality of free fall using cold atom interferometry’. *Classical and Quantum Gravity* (May 2014), vol. 31(11): p. 115010 (cit. on pp. 3, 4).
- [Ahl16] AHLERS, H. et al.: ‘Double Bragg Interferometry’. *Physical Review Letters* (2016), vol. 116(173601) (cit. on pp. 59, 82, 83).
- [Alb20a] ALBERS, HENNING: ‘Time-averaged optical potentials for creating and shaping Bose-Einstein condensates’. PhD thesis. Gottfried Wilhelm Leibniz Universität Hannover, 2020 (cit. on p. 78).
- [Alb20b] ALBERS, HENNING, ALEXANDER HERBST, LOGAN L. RICHARDSON, HENDRIK HEINE, DIPANKAR NATH, JONAS HARTWIG, CHRISTIAN SCHUBERT, CHRISTIAN VOGT, MARIAN WOLTMANN, CLAUS LÄMMERZAHN, SVEN HERRMANN, WOLFGANG ERTMER, ERNST M. RASEL, and DENNIS SCHLIPPERT: ‘Quantum test of the Universality of Free Fall using rubidium and potassium’. *The European Physical Journal D* (July 2020), vol. 74(7) (cit. on p. 2).
- [Amm97] AMMANN, HUBERT and NELSON CHRISTENSEN: ‘Delta Kick Cooling: A New Method for Cooling Atoms’. *Physical Review Letters* (Mar. 1997), vol. 78(11): pp. 2088–2091 (cit. on pp. 2, 59, 78).
- [Amr19] AMRI, S., R. CORGIER, D. SUGNY, E. M. RASEL, N. GAALLOUL, and E. CHARRON: ‘Optimal control of the transport of Bose-Einstein condensates with atom chips’. *Scientific Reports* (Mar. 2019), vol. 9(1) (cit. on pp. 5, 78).

- [And97] ANDREWS, M. R., C. G. TOWNSEND, H.-J. MIESNER, D. S. DURFEE, D. M. KURN, and W. KETTERLE: ‘Observation of Interference Between Two Bose Condensates’. *Science* (1997), vol. 275(5300) (cit. on p. 32).
- [Ase20] ASENBAUM, PETER, CHRIS OVERSTREET, MINJEONG KIM, JOSEPH CURTI, and MARK A. KASEVICH: ‘Atom-interferometric test of the equivalence principle at the 10^{-12} level’. (May 23, 2020), vol. (cit. on pp. 2, 59, 79).
- [Ase17] ASENBAUM, PETER, CHRIS OVERSTREET, TIM KOVACHY, DANIEL D. BROWN, JASON M. HOGAN, and MARK A. KASEVICH: ‘Phase Shift in an Atom Interferometer due to Spacetime Curvature across its Wave Function’. *Physical Review Letters* (May 2017), vol. 118(18) (cit. on p. 1).
- [Aub05] AUBIN, S., M. H. T. EXTAVOUR, S. MYRSKOG, L. J. LEBLANC, J. ESTÈVE, S. SINGH, P. SCRUTTON, D. MCKAY, R. MCKENZIE, I. D. LEROUX, A. STUMMER, and J. H. THYWISS: ‘Trapping Fermionic K-40 and Bosonic Rb-87 on a Chip’. *Journal of Low Temperature Physics* (Sept. 2005), vol. 140(5-6): pp. 377–396 (cit. on p. 83).
- [Ave20] AVELINE, DAVID C., JASON R. WILLIAMS, ETHAN R. ELLIOTT, CHELSEA DUTENHOFFER, JAMES R. KELLOGG, JAMES M. KOHEL, NORMAN E. LAY, KAMAL OUDRHIRI, ROBERT F. SHOTWELL, NAN YU, and ROBERT J. THOMPSON: ‘Observation of Bose–Einstein condensates in an Earth-orbiting research lab’. *Nature* (June 2020), vol. 582(7811): pp. 193–197 (cit. on pp. 2, 40, 56).
- [Bag87] BAGNATO, VANDERLEI, DAVID E. PRITCHARD, and DANIEL KLEPPNER: ‘Bose-Einstein condensation in an external potential’. *Physical Review A* (May 1987), vol. 35(10): pp. 4354–4358 (cit. on p. 43).
- [Bai06] BAILLARD, X., A. GAUGUET, S. BIZE, P. LEMONDE, PH. LAURENT, A. CLAIRON, and P. ROSENBUSCH: ‘Interference-filter-stabilized external-cavity diode lasers’. *Optics Communications* (2006), vol. 266(2): pp. 609–613 (cit. on p. 21).
- [Bar15] BARRETT, B., L. ANTONI-MICOLLIER, L. CHICHET, B. BATTELIER, P. A. GOMINET, A. BERTOLDI, P. BOUYER, and A. LANDRAGIN: ‘Correlative methods for dual-species quantum tests of the weak equivalence principle’. *New Journal of Physics* (Aug. 2015), vol. 17(8): p. 085010 (cit. on pp. 5, 84).
- [Bar16] BARRETT, BRYNLE, LAURA ANTONI-MICOLLIER, LAURE CHICHET, BAPTISTE BATTELIER, THOMAS LÉVÈQUE, ARNAUD LANDRAGIN, and PHILIPPE BOUYER: ‘Dual matter-wave inertial sensors in weightlessness’. *Nature Communications* (Dec. 2016), vol. 7(1) (cit. on pp. 4, 5, 59, 84).
- [Bar21] BARTOSCH, WOLFGANG: ‘The electronic and experimental setup of the MAIUS-2 and MAIUS-3 sounding rocket missions (in preparation)’. PhD thesis. Gottfried Wilhelm Leibniz Universität Hannover, 2021 (cit. on pp. 9, 28, 31, 41, 78).
- [Bat19] BATTELIER, BAPTISTE et al.: ‘Exploring the Foundations of the Universe with Space Tests of the Equivalence Principle’. (Aug. 30, 2019), vol. (cit. on pp. 3, 5).

- [Bec09] BECKER, DENNIS: ‘Realisierung eines kompakten und frequenzstabilen Diodenlasersystems für die Lasermanipulation von Kalium’. Bachelor thesis. Gottfried Wilhelm Leibniz Universität Hannover, 2009 (cit. on p. 20).
- [Bec18] BECKER, DENNIS et al.: ‘Space-borne Bose–Einstein condensation for precision interferometry’. *Nature* (Oct. 2018), vol. 562(7727): pp. 391–395 (cit. on pp. 4, 55).
- [Ber15] BERG, P., S. ABEND, G. TACKMANN, C. SCHUBERT, E. GIESE, W. P. SCHLEICH, F. A. NARDUCCI, W. ERTMER, and E. M. RASEL: ‘Composite-Light-Pulse Technique for High-Precision Atom Interferometry’. *Physical Review Letters* (Feb. 2015), vol. 114(6) (cit. on p. 1).
- [Bid13] BIDEL, YANNICK, OLIVIER CARRAZ, RENÉE CHARRIÈRE, MALO CADORET, NASSIM ZAHZAM, and ALEXANDRE BRESSON: ‘Compact cold atom gravimeter for field applications’. *Applied Physics Letters* (Apr. 2013), vol. 102(14): p. 144107 (cit. on pp. 1, 59).
- [Bis10] BISMUT, G., B. PASQUIOU, E. MARÉCHAL, P. PEDRI, L. VERNAC, O. GORCEIX, and B. LABURTHE-TOLRA: ‘Collective Excitations of a Dipolar Bose-Einstein Condensate’. *Physical Review Letters* (July 2010), vol. 105(4) (cit. on p. 66).
- [Bjo83] BJORKLUND, G. C., M. D. LEVENSON, W. LENTH, and C. ORTIZ: ‘Frequency modulation (FM) spectroscopy’. *Applied Physics B* (1983), vol. 32(145-152) (cit. on p. 21).
- [Bla01] BLASER, J. P.: ‘Can the equivalence principle be tested with freely orbiting masses?’ *Classical and Quantum Gravity* (June 2001), vol. 18(13): pp. 2509–2514 (cit. on p. 3).
- [Blo01] BLOCH, IMMANUEL, MARKUS GREINER, OLAF MANDEL, THEODOR W. HÄNSCH, and TILMAN ESSLINGER: ‘Sympathetic cooling of Rb-85 and Rb-87’. *Physical Review A* (July 2001), vol. 64(2) (cit. on p. 45).
- [Bol14] BOLPASI, V., N. K. EFREMIDIS, M. J. MORRISSEY, P. C. CONDYLIS, D. SAHAGUN, M. BAKER, and W. von KLITZING: ‘An ultra-bright atom laser’. *New Journal of Physics* (2014), vol. 16(033036) (cit. on p. 15).
- [Bon12] BONVALOT, S., G. BALMINO, A. BRIAIS, M. KUHN, A. PEYREFITTE, N. VALES, R. BIANCALE, G. GABALDA, F. REINQUIN, and M. SARRAILH: *World Gravity Map*. Ed. by BGI-CGMW-CNES-IRD. 2012 (cit. on p. 19).
- [Bri06] BRINK, D. M. and C. V. SUKUMAR: ‘Majorana spin-flip transitions in a magnetic trap’. *Physical Review A* (Sept. 2006), vol. 74(3) (cit. on p. 38).
- [Bur18] BURCHIANTI, A., C. D’ERRICO, S. ROSI, A. SIMONI, M. MODUGNO, C. FORT, and F. MINARDI: ‘Dual-species Bose-Einstein condensate of K-41 and Rb-87 in a hybrid trap’. *Physical Review A* (Dec. 2018), vol. 98(6) (cit. on pp. 5, 35, 46, 48–50, 53, 55, 56, 71).

- [Bur97] BURT, E. A., R. W. GHRIST, C. J. MYATT, M. J. HOLLAND, E. A. CORNELL, and C. E. WIEMAN: ‘Coherence, Correlations, and Collisions: What One Learns about Bose-Einstein Condensates from Their Decay’. *Physical Review Letters* (July 1997), vol. 79(3): pp. 337–340 (cit. on p. 42).
- [Cam84] CAMPARO, J. C. and R. P. FRUEHOLZ: ‘A dressed atom interpretation of adiabatic rapid passage’. *Journal of Physics B: Atomic and Molecular Physics* (Oct. 1984), vol. 17(20): pp. 4169–4178 (cit. on p. 80).
- [Cam10] CAMPBELL, ROBERT L. D., ROBERT P. SMITH, NAAMAN TAMMUZ, SCOTT BEATTIE, STUART MOULDER, and ZORAN HADZIBABIC: ‘Efficient production of large K-39 Bose-Einstein condensates’. *Physical Review A* (Dec. 2010), vol. 82(6) (cit. on p. 40).
- [Can06] CANUEL, B., F. LEDUC, D. HOLLEVILLE, A. GAUGUET, J. FILS, A. VIRDIS, A. CLAIRON, N. DIMARCO, CH. J. BORDÉ, A. LANDRAGIN, and P. BOUYER: ‘Six-Axis Inertial Sensor Using Cold-Atom Interferometry’. *Physical Review Letters* (July 2006), vol. 97(1) (cit. on p. 82).
- [Cas96] CASTIN, Y. and R. DUM: ‘Bose-Einstein Condensates in Time Dependent Traps’. *Physical Review Letters* (Dec. 1996), vol. 77(27): pp. 5315–5319 (cit. on p. 60).
- [Cha06] CHAUDHURI, SAPTARISHI, SANJUKTA ROY, and C. S. UNNIKRISHNAN: ‘Realization of an intense cold Rb atomic beam based on a two-dimensional magneto-optical trap: Experiments and comparison with simulations’. *Physical Review A* (2006), vol. 74(023406) (cit. on pp. 12, 13).
- [Che16] CHEN, HAO-ZE, XING-CAN YAO, YU-PING WU, XIANG-PEI LIU, XIAO-QIONG WANG, YU-XUAN WANG, YU-AO CHEN, and JIAN-WEI PAN: ‘Production of large K-41 Bose-Einstein condensates using D1 gray molasses’. *Physical Review A* (Sept. 2016), vol. 94(3) (cit. on pp. 44, 45).
- [Chu86] CHU, S., J. E. BJORKHOLM, A. ASHKIN, J. P. GORDON, and L. W. HOLLBERG: ‘Proposal for optically cooling atoms to temperatures of the order of $10E-6$ K’. *Optics Letters* (Feb. 1986), vol. 11(2): p. 73 (cit. on p. 78).
- [Coo94] COOPER, C. J., G. HILLENBRAND, J. RINK, C. G. TOWNSEND, K. ZETIE, and C. J. FOOT: ‘The Temperature of Atoms in a Magneto-optical Trap’. *Europhysics Letters (EPL)* (Nov. 1994), vol. 28(6): pp. 397–402 (cit. on p. 37).
- [Cor18] CORGIER, R., S. AMRI, W. HERR, H. AHLERS, J. RUDOLPH, D. GUÉRY-ODELIN, E. M. RASEL, E. CHARRON, and N. GAALOUL: ‘Fast manipulation of Bose-Einstein condensates with an atom chip’. *New Journal of Physics* (May 2018), vol. 20(5): p. 055002 (cit. on pp. 5, 66, 74, 78).
- [Cor20] CORGIER, ROBIN, SINA LORIANI, HOLGER AHLERS, KATERINE POSSO-TRUJILLO, CHRISTIAN SCHUBERT, ERNST M. RASEL, ERIC CHARRON, and NACEUR GAALOUL: ‘Interacting quantum mixtures for precision atom interferometry’. (July 9, 2020), vol. (cit. on pp. 5, 46, 61, 68, 71, 73, 74, 79).

- [Cor02] CORNELL, E. A. and C. E. WIEMAN: ‘Nobel Lecture: Bose-Einstein condensation in a dilute gas, the first 70 years and some recent experiments’. *Reviews of Modern Physics* (Aug. 2002), vol. 74(3): pp. 875–893 (cit. on p. 3).
- [Cro09] CRONIN, ALEXANDER D., JÖRG SCHMIEDMAYER, and DAVID E. PRITCHARD: ‘Optics and interferometry with atoms and molecules’. *Reviews of Modern Physics* (July 2009), vol. 81(3): pp. 1051–1129 (cit. on p. 1).
- [DAm17] D’AMICO, G., G. ROSI, S. ZHAN, L. CACCIAPUOTI, M. FATTORI, and G. M. TINO: ‘Canceling the Gravity Gradient Phase Shift in Atom Interferometry’. *Physical Review Letters* (Dec. 2017), vol. 119(25) (cit. on p. 3).
- [Dam02] DAMOUR, T., F. PIAZZA, and G. VENEZIANO: ‘Violations of the equivalence principle in a dilaton-runaway scenario’. *Physical Review D* (Aug. 2002), vol. 66(4) (cit. on p. 1).
- [Dam12] DAMOUR, THIBAUT: ‘Theoretical aspects of the equivalence principle’. *Classical and Quantum Gravity* (Aug. 2012), vol. 29(18): p. 184001 (cit. on p. 5).
- [Dav95] DAVIS, K. B., M. O. MEWES, and W. KETTERLE: ‘An analytical model for evaporative cooling of atoms’. *Applied Physics B Laser and Optics* (1995), vol. 60(2-3): pp. 155–159 (cit. on p. 45).
- [Del01] DELANNOY, G., S. G. MURDOCH, V. BOYER, V. JOSSE, P. BOUYER, and A. ASPECT: ‘Understanding the production of dual Bose-Einstein condensation with sympathetic cooling’. *Physical Review A* (Apr. 2001), vol. 63(5) (cit. on p. 47).
- [Dep21] DEPPNER, C., W. HERR, E. M. RASEL, M. CORNELIUS, S. HERRMANN, C. LÄMMERZAHN, P. STROMBERGER, A. WENZLAWSKI, and P. WINDPASSINGER: ‘Collective-mode enhanced matter-wave optics’. *To be published* (2021), vol. (cit. on pp. 4, 66, 78).
- [Dic13] DICKERSON, SUSANNAH M., JASON M. HOGAN, ALEX SUGARBAKER, DAVID M. S. JOHNSON, and MARK A. KASEVICH: ‘Multi-axis Inertial Sensing with Long-Time Point Source Atom Interferometry’. *Phys. Rev. Lett.* (2013), vol. 111(083001) (cit. on p. 32).
- [Din16] DINKELAKER, ALINE, MAX SCHIEMANGK, VLADIMIR SCHKOLNIK, ANDREW KENYON, MARKUS KRUTZIK, and ACHIM PETERS: ‘KALEXUS - a Potassium Laser System with Autonomous Frequency Stabilization on a Sounding Rocket’. *Frontiers in Optics 2016*. OSA, 2016 (cit. on p. 5).
- [Dup15] DUPONT-NIVET, M., M. CASIULIS, T. LAUDAT, C. I. WESTBROOK, and S. SCHWARTZ: ‘Microwave-stimulated Raman adiabatic passage in a Bose-Einstein condensate on an atom chip’. *Physical Review A* (2015), vol. 91(053420) (cit. on pp. 15, 33).
- [Dut16] DUTTA, I., D. SAVOIE, B. FANG, B. VENON, C. L. GARRIDO ALZAR, R. GEIGER, and A. LANDRAGIN: ‘Continuous Cold-Atom Inertial Sensor with 1 nrad/sec Rotation Stability’. *Physical Review Letters* (May 2016), vol. 116(18) (cit. on p. 1).

- [Dva02] DVALI, GIA and MATIAS ZALDARRIAGA: ‘Changing alpha with Time: Implications for Fifth-Force-Type Experiments and Quintessence’. *Physical Review Letters* (Feb. 2002), vol. 88(9) (cit. on p. 1).
- [Edw96] EDWARDS, MARK, P. A. RUPRECHT, K. BURNETT, R. J. DODD, and CHARLES W. CLARK: ‘Collective Excitations of Atomic Bose-Einstein Condensates’. *Physical Review Letters* (Aug. 1996), vol. 77(9): pp. 1671–1674 (cit. on p. 66).
- [Ell18] ELLIOTT, ETHAN R., MARKUS C. KRUTZIK, JASON R. WILLIAMS, ROBERT J. THOMPSON, and DAVID C. AVELINE: ‘NASA’s Cold Atom Lab (CAL): system development and ground test status’. *npj Microgravity* (Aug. 2018), vol. 4(1) (cit. on pp. 4, 35, 40, 41, 83).
- [Els21] ELSÉN, MICHAEL: ‘Investigations of Ultra-High Vacuum Systems for Space Missions with Cold Atoms Experiments (in preparation)’. PhD thesis. Universität Bremen, 2021 (cit. on pp. 8, 33).
- [Els20] ELSÉN, MICHAEL et al.: ‘A Dual-Species Atom Interferometer Payload for Operation on Sounding Rockets’. *In Preparation* (2020), vol. (cit. on pp. 32, 33).
- [Ext06] EXTAVOUR, M. H. T., L. J. LEBLANC, T. SCHUMM, B. CIESLAK, S. MYRSKOG, A. STUMMER, S. AUBIN, and J. H. THYWISSEN: ‘Dual-Species Quantum Degeneracy of K-40 and Rb-87 on an Atom Chip’. *AIP Conference Proceedings*. AIP, 2006 (cit. on p. 83).
- [Fal08] FALKE, STEPHAN, HORST KNÖCKEL, JAN FRIEBE, MATTHIAS RIEDMANN, EBERHARD TIEMANN, and CHRISTIAN LISDAT: ‘Potassium ground-state scattering parameters and Born-Oppenheimer potentials from molecular spectroscopy’. *Physical Review A* (July 2008), vol. 78(1) (cit. on p. 45).
- [Fan18] FANCHER, C. T., A. J. PYLE, A. P. ROTUNNO, and S. AUBIN: ‘Microwave ac Zeeman force for ultracold atoms’. *Physical Review A* (2018), vol. 97(043430) (cit. on p. 15).
- [Fei82] FEIT, M. D., J. A. FLECK, and A. STEIGER: ‘Solution of the Schrödinger equation by a spectral method’. *Journal of Computational Physics* (Sept. 1982), vol. 47(3): pp. 412–433 (cit. on p. 72).
- [Fer06] FERLAINO, FRANCESCA, CHIARA D’ERRICO, GIACOMO ROATI, MATTEO ZACCANTI, MASSIMO INGUSCIO, GIOVANNI MODUGNO, and ANDREA SIMONI: ‘Feshbach spectroscopy of a K-Rb atomic mixture’. *Physical Review A* (Apr. 2006), vol. 73(4) (cit. on p. 45).
- [Fer02] FERRARI, G., M. INGUSCIO, W. JASTRZEBSKI, G. MODUGNO, G. ROATI, and A. SIMONI: ‘Collisional Properties of Ultracold K-Rb Mixtures’. *Physical Review Letters* (July 2002), vol. 89(5) (cit. on p. 49).
- [Fol02] FOLMAN, RON, PETER KRÜGER, JÖRG SCHMIEDMAYER, JOHANNES DENSCHLAG, and CARSTEN HENKEL: ‘Microscopic Atom Optics: From Wires to an Atom Chip’. *Advances In Atomic, Molecular, and Optical Physics*. Elsevier, 2002: pp. 263–356 (cit. on pp. 9, 78).

- [For03] FORT, C., F. S. CATALIOTTI, L. FALLANI, F. FERLAINO, P. MADDALONI, and M. INGUSCIO: ‘Collective Excitations of a Trapped Bose-Einstein Condensate in the Presence of a 1D Optical Lattice’. *Physical Review Letters* (Apr. 2003), vol. 90(14) (cit. on p. 66).
- [For07] FORTÁGH, JÓZSEF and CLAUS ZIMMERMANN: ‘Magnetic microtraps for ultracold atoms’. *Reviews of Modern Physics* (Feb. 2007), vol. 79(1): pp. 235–289 (cit. on p. 3).
- [Fre18] FREITAG, STEFFEN: ‘Eine graue Melassekühlung von K-39 und K-41 in MAIUS-B’. Bachelor thesis. Gottfried Wilhelm Leibniz Universität Hannover, 2018 (cit. on p. 45).
- [Fry17] FRYE, KAI: ‘A compact laser system for the manipulation of potassium atoms and a magnetic conveyor belt for rubidium atoms’. Master thesis. Gottfried Wilhelm Leibniz Universität Hannover, 2017 (cit. on p. 20).
- [Fry19] FRYE, KAI et al.: ‘The Bose-Einstein Condensate and Cold Atom Laboratory’. (Dec. 10, 2019), vol. (cit. on p. 4).
- [Gei13] GEISEL, I., K. CORDES, J. MAHNKE, S. JÖLLENBECK, J. OSTERMANN, J. ARLT, and W. ERTMER and C. KLEMP: ‘Evolutionary optimization of an experimental apparatus’. *Appl. Phys. Lett.* (2013), vol. 102(214105) (cit. on p. 31).
- [Gie13] GIESE, E., A. ROURA, G. TACKMANN, E. M. RASEL, and W. P. SCHLEICH: ‘Double Bragg diffraction: A tool for atom optics’. *Physical Review A* (2013), vol. 88(053608) (cit. on pp. 3, 82).
- [Gio96] GIORGINI, S., L. P. PITAEVSKII, and S. STRINGARI: ‘Condensate fraction and critical temperature of a trapped interacting Bose gas’. *Physical Review A* (Dec. 1996), vol. 54(6): R4633–R4636 (cit. on p. 43).
- [Gol02] GOLDWIN, J., S. B. PAPP, B. DEMARCO, and D. S. JIN: ‘Two-species magneto-optical trap with K-40 and Rb-87’. *Physical Review A* (Jan. 2002), vol. 65(2) (cit. on p. 36).
- [Gou08] GOUËT, J. LE, T. E. MEHLSTÄUBLER, J. KIM, S. MERLET, A. CLAIRON, A. LANDRAGIN, and F. PEREIRA DOS SANTOS: ‘Limits to the sensitivity of a low noise compact atomic gravimeter’. *Applied Physics B* (June 2008), vol. 92(2): pp. 133–144 (cit. on p. 2).
- [Gro16] GROSSE, JENS: ‘Thermal and Mechanical Design and Simulation for the first High Precision Quantum Optics Experiment on a Sounding Rocket’. PhD thesis. Universität Bremen, 2016 (cit. on p. 9).
- [Haa07] HAAS, M., V. LEUNG, D. FRESE, D. HAUBRICH, S. JOHN, C. WEBER, A. RAUSCHENBEUTEL, and D. MESCHEDER: ‘Species-selective microwave cooling of a mixture of rubidium and caesium atoms’. *New Journal of Physics* (May 2007), vol. 9(5): pp. 147–147 (cit. on pp. 40, 41).

- [Hän01] HÄNSEL, W., P. HOMMELHOFF, T. W. HÄNSCH, and J. REICHEL: ‘Bose–Einstein condensation on a microelectronic chip’. *Nature* (2001), vol. 413(498-501) (cit. on p. 35).
- [Har16] HARDMAN, K. S., P. J. EVERITT, G. D. McDONALD, P. MANJU, P. B. WIGLEY, M. A. SOORIYABANDARA, C. C. N. KUHN, J. E. DEBS, J. D. CLOSE, and N. P. ROBINS: ‘Simultaneous Precision Gravimetry and Magnetic Gradiometry with a Bose-Einstein Condensate: A High Precision, Quantum Sensor’. *Physical Review Letters* (Sept. 2016), vol. 117(13) (cit. on p. 1).
- [Har08] HARRIS, M. L., P. TIERNEY, and S. L. CORNISH: ‘Magnetic trapping of a cold Rb–Cs atomic mixture’. *Journal of Physics B: Atomic, Molecular and Optical Physics* (Feb. 2008), vol. 41(5): p. 059803 (cit. on p. 71).
- [Har20] HARTMANN, SABRINA, JENS JENEWEIN, ENNO GIESE, SVEN ABEND, ALBERT ROURA, ERNST M. RASEL, and WOLFGANG P. SCHLEICH: ‘Regimes of atomic diffraction: Raman versus Bragg diffraction in retroreflective geometries’. *Physical Review A* (May 2020), vol. 101(5) (cit. on p. 59).
- [Har15] HARTWIG, J., S. ABEND, C. SCHUBERT, D. SCHLIPPERT, H. AHLERS, K. POSSO-TRUJILLO, N. GAALLOUL, W. ERTMER, and E. M. RASEL: ‘Testing the universality of free fall with rubidium and ytterbium in a very large baseline atom interferometer’. *New Journal of Physics* (Mar. 2015), vol. 17(3): p. 035011 (cit. on p. 5).
- [Has17] HASLINGER, PHILIPP, MATT JAFFE, VICTORIA XU, OSIP SCHWARTZ, MATTHIAS SONNLEITNER, MONIKA RITSCH-MARTE, HELMUT RITSCH, and HOLGER MÜLLER: ‘Attractive force on atoms due to blackbody radiation’. *Nature Physics* (Dec. 2017), vol. 14(3): pp. 257–260 (cit. on p. 1).
- [Hau01] HAUGAN, MARK P. and C. LÄMMERZAHN: ‘Principles of Equivalence: Their Role in Gravitation Physics and Experiments That Test Them’. *Gyros, Clocks, Interferometers...: Testing Relativistic Gravity in Space*. Springer Berlin Heidelberg, 2001: pp. 195–212 (cit. on p. 1).
- [Hau13] HAUTH, M., C. FREIER, V. SCHKOLNIK, A. SENGER, M. SCHMIDT, and A. PETERS: ‘First gravity measurements using the mobile atom interferometer GAIN’. *Applied Physics B* (Apr. 2013), vol. 113(1): pp. 49–55 (cit. on pp. 1, 2, 59).
- [Hec14] HECHENBLAIKNER, GERALD, MARC-PETER HESS, MARIANNA VITELLI, and JAN BECK: ‘STE-QUEST mission and system design’. *Experimental Astronomy* (Mar. 2014), vol. 37(3): pp. 481–501 (cit. on p. 3).
- [Her17] HERBST, ALEXANDER: ‘A laser system for testing the MAIUS-B payload’. Master thesis. Gottfried Wilhelm Leibniz Universität Hannover, 2017 (cit. on pp. 20, 21).

- [Her13] HERR, WALDEMAR: ‘Eine kompakte Quelle quantenentarteter Gase hohen Flusses für die Atominterferometrie unter Schwerelosigkeit’. PhD thesis. Gottfried Wilhelm Leibniz Universität Hannover, 2013 (cit. on pp. 14, 35, 37, 41, 74).
- [Het15] HETZEL, MAREIKE: ‘Aufbau und Charakterisierung von Lichtquellen und Optik für die Laserkühlung von Kalium’. Bachelor thesis. Gottfried Wilhelm Leibniz Universität Hannover, 2015 (cit. on p. 20).
- [Hof06] HOFFERBERTH, S., I. LESANOVSKY, B. FISCHER, J. VERDU, and J. SCHMIED-MAYER: ‘Radio-frequency dressed state potentials for neutral atoms’. *Nature Physics* (2006), vol. 2(710-716) (cit. on p. 15).
- [Hog08] HOGAN, JASON M., DAVID M. S. JOHNSON, and MARK A. KASEVICH: *Light-pulse atom interferometry*. 2008 (cit. on p. 32).
- [Hol10] HOLMGREN, WILLIAM F., MELISSA C. REVELLE, VINCENT P. A. LONIJ, and ALEXANDER D. CRONIN: ‘Absolute and ratio measurements of the polarizability of Na, K, and Rb with an atom interferometer’. *Physical Review A* (May 2010), vol. 81(5) (cit. on p. 1).
- [Jin96] JIN, D. S., J. R. ENSHER, M. R. MATTHEWS, C. E. WIEMAN, and E. A. CORNELL: ‘Collective Excitations of a Bose-Einstein Condensate in a Dilute Gas’. *Physical Review Letters* (July 1996), vol. 77(3): pp. 420–423 (cit. on p. 66).
- [Kar18] KARCHER, R., A. IMANALIEV, S. MERLET, and F. PEREIRA DOS SANTOS: ‘Improving the accuracy of atom interferometers with ultracold sources’. *New Journal of Physics* (Nov. 2018), vol. 20(11): p. 113041 (cit. on p. 59).
- [Kas91] KASEVICH, MARK and STEVEN CHU: ‘Atomic interferometry using stimulated Raman transitions’. *Physical Review Letters* (July 1991), vol. 67(2): pp. 181–184 (cit. on pp. 2, 82).
- [Ket96] KETTERLE, W. and N. J. VAN DRUTEN: ‘Evaporative Cooling of Trapped Atoms’. *Advances In Atomic, Molecular, and Optical Physics*. Elsevier, 1996: pp. 181–236 (cit. on p. 40).
- [Ket99] KETTERLE, W., D. S. DURFEE, and D. M. STAMPER-KURN: ‘Making, probing and understanding Bose-Einstein condensates’. (Apr. 2, 1999), vol. (cit. on p. 68).
- [Ket02] KETTERLE, WOLFGANG: ‘Nobel lecture: When atoms behave as waves: Bose-Einstein condensation and the atom laser’. *Reviews of Modern Physics* (Nov. 2002), vol. 74(4): pp. 1131–1151 (cit. on p. 3).
- [Kis09] KISHIMOTO, T., J. KOBAYASHI, K. NODA, K. AIKAWA, M. UEDA, and S. INOUE: ‘Direct evaporative cooling of K-41 into a Bose-Einstein condensate’. *Physical Review A* (Mar. 2009), vol. 79(3) (cit. on pp. 36, 44).
- [Kle10] KLEINE BÜNING, G., J. WILL, W. ERTMER, C. KLEMPT, and J. ARLT: ‘A slow gravity compensated atom laser’. *Applied Physics B* (May 2010), vol. 100(1): pp. 117–123 (cit. on p. 2).

- [Kle07a] KLEMPPT, C., T. HENNINGER, O. TOPIC, J. WILL, W. ERTMER, E. TIEMANN, and J. ARLT: ‘K-40-Rb-87 Feshbach resonances: Modeling the interatomic potential’. *Physical Review A* (Aug. 2007), vol. 76(2) (cit. on p. 5).
- [Kle06] KLEMPPT, C., T. van ZOEST, T. HENNINGER, O. TOPIC, E. M. RASEL, W. ERTMER, and J. ARLT: ‘Ultraviolet light-induced atom desorption for large rubidium and potassium magneto-optical traps’. *Physical Review A* (2006), vol. 73(013410) (cit. on p. 13).
- [Kle07b] KLEMPPT, CARSTEN: ‘Wechselwirkung in Bose-Fermi-Quantengasen’. PhD thesis. Gottfried Wilhelm Leibniz Universität Hannover, 2007 (cit. on p. 40).
- [Kov15] KOVACHY, TIM, JASON M. HOGAN, ALEX SUGARBAKER, SUSANNAH M. DICKERSON, CHRISTINE A. DONNELLY, CHRIS OVERSTREET, and MARK A. KASEVICH: ‘Matter Wave Lensing to Picokelvin Temperatures’. *Physical Review Letters* (Apr. 2015), vol. 114(14) (cit. on p. 78).
- [Kub16] KUBELKA-LANGE, ANDRÉ, SVEN HERRMANN, JENS GROSSE, CLAUS LÄMMERZAHN, ERNST M. RASEL, and CLAUS BRAXMAIER: ‘A three-layer magnetic shielding for the MAIUS-1 mission on a sounding rocket’. *Rev. Sci. Instrum.* (2016), vol. 87(6): p. 063101 (cit. on pp. 7, 55).
- [Kür20] KÜRBIS, CH., A. BAWAMIA, M. KRÜGER, R. SMOL, A. PETERS, A. WICHT, and G. TRÄNKLE: ‘Extended cavity diode laser master-oscillator-power-amplifier for operation of an iodine frequency reference on a sounding rocket’. *Appl. Opt.* (2020), vol. 59(253-262) (cit. on pp. 20, 33).
- [Lac20] LACHMANN, MAIKE: ‘Materiewelleninterferenzen im Weltraum’. PhD thesis. Gottfried Wilhelm Leibniz Universität Hannover, 2020 (cit. on pp. 78, 80).
- [Lac21] LACHMANN, MAIKE D. et al.: ‘Ultracold atom interferometry in space’. *Nature Communications* (Feb. 2021), vol. 12(1) (cit. on p. 4).
- [Lan11] LANDINI, M., S. ROY, L. CARCAGNI, D. TRYPOGEOGOS, M. FATTORI, M. INGUSCIO, and G. MODUGNO: ‘Sub-Doppler laser cooling of potassium atoms’. *Physical Review A* (Oct. 2011), vol. 84(4) (cit. on p. 37).
- [Lea03] LEANHARDT, A. E.: ‘Cooling Bose-Einstein Condensates Below 500 Picokelvin’. *Science* (Sept. 2003), vol. 301(5639): pp. 1513–1515 (cit. on p. 2).
- [Len97] LENEFF, ALAN, TROY D. HAMMOND, EDWARD T. SMITH, MICHAEL S. CHAPMAN, RICHARD A. RUBENSTEIN, and DAVID E. PRITCHARD: ‘Rotation Sensing with an Atom Interferometer’. *Phys. Rev. Lett.* (1997), vol. 78(760) (cit. on p. 32).
- [Lev09] LEVEQUE, T., A. GAUGUET, F. MICHAUD, F. PEREIRA DOS SANTOS, and A. LANDRAGIN: ‘Enhancing the Area of a Raman Atom Interferometer Using a Versatile Double-Diffraction Technique’. *Physical Review Letters* (2009), vol. 103(080405) (cit. on pp. 3, 59, 80, 82).

- [Lor20] LORIANI, SINA, CHRISTIAN SCHUBERT, DENNIS SCHLIPPERT, WOLFGANG ERTMER, FRANCK PEREIRA DOS SANTOS, ERNST MARIA RASEL, NACEUR GAALOUL, and PETER WOLF: ‘Resolution of the Co-Location Problem in Satellite Quantum Tests of the Universality of Free Fall’. (June 15, 2020), vol. (cit. on p. 3).
- [Lot20] LOTZ, CHRISTOPH, TOBIAS FROBÖSE, ALEXANDER WANNER, LUDGER OVERMEYER, and WOLFGANG ERTMER: ‘Einstein-Elevator: A New Facility for Research from μg to 5 g’. *Gravitational and Space Research* (July 2020), vol. 5(2): pp. 11–27 (cit. on p. 79).
- [Lou11] LOUCHET-CHAUVET, ANNE, TRISTAN FARAH, QUENTIN BODART, ANDRÉ CLAIRON, ARNAUD LANDRAGIN, SÉBASTIEN MERLET, and FRANCK PEREIRA DOS SANTOS: ‘The influence of transverse motion within an atomic gravimeter’. *New Journal of Physics* (June 2011), vol. 13(6): p. 065025 (cit. on p. 59).
- [Mar00a] MARAGÒ, O. M., S. A. HOPKINS, J. ARLT, E. HODBY, G. HECHENBLAIKNER, and C. J. FOOT: ‘Observation of the Scissors Mode and Evidence for Superfluidity of a Trapped Bose-Einstein Condensed Gas’. *Physical Review Letters* (Mar. 2000), vol. 84(10): pp. 2056–2059 (cit. on p. 66).
- [Mar00b] MARCASSA, L. G., G. D. TELLES, S. R. MUNIZ, and V. S. BAGNATO: ‘Collisional losses in a K-Rb cold mixture’. *Physical Review A* (Dec. 2000), vol. 63(1) (cit. on p. 36).
- [Mar02] MARTE, A., T. VOLZ, J. SCHUSTER, S. DÜRR, G. REMPE, E. G. M. van KEMPEN, and B. J. VERHAAR: ‘Feshbach Resonances in Rubidium 87: Precision Measurement and Analysis’. *Physical Review Letters* (Dec. 2002), vol. 89(28) (cit. on p. 45).
- [Mar07] MARZOK, C., B. DEH, PH. W. COURTEILLE, and C. ZIMMERMANN: ‘Ultracold thermalization of Li-7 and Rb-87’. *Physical Review A* (Nov. 2007), vol. 76(5) (cit. on p. 40).
- [McC11] MCCARRON, D. J., H. W. CHO, D. L. JENKIN, M. P. KÖPPINGER, and S. L. CORNISH: ‘Dual-species Bose-Einstein condensate of Rb-87 and Cs-133’. *Physical Review A* (July 2011), vol. 84(1) (cit. on p. 71).
- [McG02] MCGUIRK, J. M., G. T. FOSTER, J. B. FIXLER, M. J. SNADDEN, and M. A. KASEVICH: ‘Sensitive absolute-gravity gradiometry using atom interferometry’. *Physical Review A* (Feb. 2002), vol. 65(3) (cit. on p. 2).
- [Mew96] MEWES, M.-O., M. R. ANDREWS, N. J. van DRUTEN, D. M. KURN, D. S. DURFEE, C. G. TOWNSEND, and W. KETTERLE: ‘Collective Excitations of a Bose-Einstein Condensate in a Magnetic Trap’. *Physical Review Letters* (Aug. 1996), vol. 77(6): pp. 988–991 (cit. on p. 66).
- [Mie96] MIES, FREDERICK H., CARL J. WILLIAMS, PAUL S. JULIENNE, and MORRIS KRAUSS: ‘Estimating Bounds on Collisional Relaxation Rates of Spin-Polarized Rb-87 Atoms at Ultracold Temperatures’. *J. Res. Natl. Inst. Stand. Technol.* (1996), vol. (cit. on p. 41).

- [Mih19] MIHM, MORITZ, JEAN PIERRE MARBURGER, ANDRÉ WENZLAWSKI, ORTWIN HELLMIG, OLIVER ANTON, KLAUS DÖRINGSHOFF, MARKUS KRUTZIK, ACHIM PETERS, PATRICK WINDPASSINGER, and the MAIUS TEAM: ‘ZERODUR based optical systems for quantum gas experiments in space’. *Acta Astronautica* (2019), vol. 159(166-169) (cit. on pp. 20, 33).
- [Mis20] MISSLISCH, MAGDALENA: ‘Zustandspräparation von Rb-87 und Entwurf eines Interferometriesetups für die Höhenforschungsraketenmissionen MAIUS-2/3’. Bachelor thesis. Gottfried Wilhelm Leibniz Universität Hannover, 2020 (cit. on pp. 15, 77, 80).
- [Mod01] MODUGNO, G.: ‘Bose-Einstein Condensation of Potassium Atoms by Sympathetic Cooling’. *Science* (Oct. 2001), vol. 294(5545): pp. 1320–1322 (cit. on pp. 35, 40, 54–56).
- [Mos01] MOSK, A., S. KRAFT, M. MUDRICH, K. SINGER, W. WOHLLEBEN, R. GRIMM, and M. WEIDEMÜLLER: ‘Mixture of ultracold lithium and cesium atoms in an optical dipole trap’. *Applied Physics B* (Dec. 2001), vol. 73(8): pp. 791–799 (cit. on p. 52).
- [Mül19] MÜLLER, GABRIEL: ‘Atom chip traps simulations for microgravity and space atom optics experiments’. Bachelor thesis. Gottfried Wilhelm Leibniz Universität Hannover, 2019 (cit. on pp. 54, 59).
- [Mün13] MÜNTINGA, H. et al.: ‘Interferometry with Bose-Einstein Condensates in Microgravity’. *Physical Review Letters* (Feb. 2013), vol. 110(9) (cit. on pp. 3, 78).
- [Mya97] MYATT, C. J., E. A. BURT, R. W. GHRIST, E. A. CORNELL, and C. E. WIEMAN: ‘Production of Two Overlapping Bose-Einstein Condensates by Sympathetic Cooling’. *Physical Review Letters* (Jan. 1997), vol. 78(4): pp. 586–589 (cit. on p. 45).
- [Nar98] NARASCHEWSKI, M. and D. M. STAMPER-KURN: ‘Analytical description of a trapped semi-ideal Bose gas at finite temperature’. *Physical Review A* (Sept. 1998), vol. 58(3): pp. 2423–2426 (cit. on pp. 43, 44).
- [Nat13] NATH, DIPANKAR, R. KOLLENGODE EASWARAN, G. RAJALAKSHMI, and C. S. UNNIKRISHNAN: ‘Quantum-interference-enhanced deep sub-Doppler cooling of K-39 atoms in gray molasses’. *Physical Review A* (Nov. 2013), vol. 88(5) (cit. on p. 45).
- [Ott01] OTT, H., J. FORTAGH, G. SCHLOTTERBECK, A. GROSSMANN, and C. ZIMMERMANN: ‘Bose-Einstein Condensation in a Surface Microtrap’. *Physical Review Letters* (Nov. 2001), vol. 87(23) (cit. on p. 35).
- [Ove18] OVERSTREET, CHRIS, PETER ASENBAUM, TIM KOVACHY, REMY NOTERMANS, JASON M. HOGAN, and MARK A. KASEVICH: ‘Effective Inertial Frame in an Atom Interferometric Test of the Equivalence Principle’. *Physical Review Letters* (May 2018), vol. 120(18) (cit. on p. 3).

- [Pap17] PAPA-KONSTANTINOU, ALEXANDROS: ‘Development of an all-digital FPGA-based laser phaselock’. Master thesis. Gottfried Wilhelm Leibniz Universität Hannover, 2017 (cit. on pp. 22, 82).
- [Pap08] PAPP, S. B., J. M. PINO, and C. E. WIEMAN: ‘Tunable Miscibility in a Dual-Species Bose-Einstein Condensate’. *Physical Review Letters* (July 2008), vol. 101(4) (cit. on p. 71).
- [Par18] PARKER, RICHARD H., CHENGHUI YU, WEICHENG ZHONG, BRIAN ESTEY, and HOLGER MÜLLER: ‘Measurement of the fine-structure constant as a test of the Standard Model’. *Science* (Apr. 2018), vol. 360(6385): pp. 191–195 (cit. on p. 1).
- [Pet01] PETERS, A., K. Y. CHUNG, and S. CHU: ‘High-precision gravity measurements using atom interferometry’. *Metrologia* (Feb. 2001), vol. 38(1): pp. 25–61 (cit. on p. 1).
- [Pet08] PETHICK, C. J. and H. SMITH: *Bose–Einstein Condensation in Dilute Gases*. Cambridge University Press, 2008 (cit. on p. 42).
- [Phi98] PHILLIPS, WILLIAM D.: ‘Nobel Lecture: Laser cooling and trapping of neutral atoms’. *Reviews of Modern Physics* (July 1998), vol. 70(3): pp. 721–741 (cit. on p. 21).
- [Pop18] POPP, MANUEL ANDRÉ: ‘Compact, low-noise current drivers for Quantum Sensors with Atom Chips’. PhD thesis. Gottfried Wilhelm Leibniz Universität Hannover, 2018 (cit. on pp. 26, 28, 33, 64).
- [Ras06] RASMUSSEN, C. E. and C. K. I. WILLIAMS: *Gaussian processes for Machine Learning*. MIT Press, 2006 (cit. on p. 31).
- [Rei99] REICHEL, J., W. HÄNSEL, and T. W. HÄNSCH: ‘Atomic Micromanipulation with Magnetic Surface Traps’. *Physical Review Letters* (1999), vol. 83(17) (cit. on p. 16).
- [Rei11] REICHEL, JAKOB and VLADAN VULETIC: *Atom chips*. WILEY-VCH Verlag GmbH & Co. KGaA, 2011 (cit. on p. 50).
- [Rei07] REINAUDI, G., T. LAHAYE, Z. WANG, and D. GUÉRY-ODELIN: ‘Strong saturation absorption imaging of dense clouds of ultracold atoms’. *Optics Letters* (Oct. 2007), vol. 32(21): p. 3143 (cit. on pp. 17, 66).
- [Rib02] RIBOLI, FRANCESCO and MICHELE MODUGNO: ‘Topology of the ground state of two interacting Bose-Einstein condensates’. *Physical Review A* (June 2002), vol. 65(6) (cit. on p. 71).
- [Ric19a] RICHARDSON, L. L. et al.: ‘Optomechanical resonator-enhanced atom interferometry’. (Feb. 7, 2019), vol. (cit. on p. 2).
- [Ric19b] RICHARDSON, LOGAN LATHAM: *Inertial noise post-correction in atom interferometers measuring the local gravitational acceleration*. en. 2019 (cit. on p. 2).

- [Ros15] ROSI, G., L. CACCIAPUOTI, F. SORRENTINO, M. MENCHETTI, M. PREVEDELLI, and G. M. TINO: ‘Measurement of the Gravity-Field Curvature by Atom Interferometry’. *Physical Review Letters* (Jan. 2015), vol. 114(1) (cit. on p. 1).
- [Ros14] ROSI, G., F. SORRENTINO, L. CACCIAPUOTI, M. PREVEDELLI, and G. M. TINO: ‘Precision measurement of the Newtonian gravitational constant using cold atoms’. *Nature* (June 2014), vol. 510(7506): pp. 518–521 (cit. on p. 1).
- [Rou17] ROURA, ALBERT: ‘Circumventing Heisenberg’s Uncertainty Principle in Atom Interferometry Tests of the Equivalence Principle’. *Physical Review Letters* (Apr. 2017), vol. 118(16) (cit. on p. 3).
- [Rou08] ROUX, C., A. EMMERT, A. LUPASCU, T. NIRRENGARTEN, G. NOGUES, M. BRUNE, J.-M. RAIMOND, and S. HAROCHE: ‘Bose-Einstein condensation on a superconducting atom chip’. *EPL (Europhysics Letters)* (Feb. 2008), vol. 81(5): p. 56004 (cit. on p. 35).
- [Rud16] RUDOLPH, JAN: ‘Matter-Wave Optics with Bose-Einstein Condensates in Microgravity’. PhD thesis. Gottfried Wilhelm Leibniz Universität Hannover, 2016 (cit. on pp. 35, 59).
- [Rud15] RUDOLPH, JAN, WALDEMAR HERR, CHRISTOPH GRZESCHIK, TAMMO STERNKE, ALEXANDER GROTE, MANUEL POPP, DENNIS BECKER, HAUKE MÜNTINGA, HOLGER AHLERS, ACHIM PETERS, CLAUS LÄMMERZAHN, KLAUS SENGSTOCK, NACEUR GAALOUL, WOLFGANG ERTMER, and ERNST M. RASEL: ‘A high-flux BEC source for mobile atom interferometers’. *New J. Phys.* (2015), vol. 17(065001) (cit. on pp. 3, 35).
- [Saf18] SAFRONOVA, M. S., D. BUDKER, D. DEMILLE, DEREK F. JACKSON KIMBALL, A. DEREVIANKO, and CHARLES W. CLARK: ‘Search for new physics with atoms and molecules’. *Reviews of Modern Physics* (June 2018), vol. 90(2) (cit. on p. 1).
- [Sah19] SAHELGOZIN, MARAL: ‘Design and construction of a transportable quantum gravimeter and realization of an atom-chip magnetic trap’. PhD thesis. Gottfried Wilhelm Leibniz Universität Hannover, 2019 (cit. on pp. 16, 35).
- [Sal13] SALOMON, G., L. FOUCHÉ, P. WANG, A. ASPECT, P. BOUYER, and T. BOURDEL: ‘Gray-molasses cooling of K-39 to a high phase-space density’. *EPL (Europhysics Letters)* (Dec. 2013), vol. 104(6): p. 63002 (cit. on p. 45).
- [Sch16] SCHKOLNIK, V., O. HELLMIG, A. WENZLAWSKI, J. GROSSE, A. KOHFELDT, K. DÖRINGSHOFF, A. WICHT, P. WINDPASSINGER, K. SENGSTOCK, C. BRAXMAIER, M. KRUTZIK, and A. PETERS: ‘A compact and robust diode laser system for atom interferometry on a sounding rocket’. *Applied Physics B* (July 2016), vol. 122(8) (cit. on p. 5).
- [Sch10] SCHKOLNIK, VLADIMIR: ‘Realisierung eines kompakten und schmalbandigen Diodenlasersystems zur Kühlung und Manipulation von Rubidium’. Diploma thesis. Gottfried Wilhelm Leibniz Universität Hannover, 2010 (cit. on p. 20).

- [Sch14a] SCHLIPPERT, D., J. HARTWIG, H. ALBERS, L. L. RICHARDSON, C. SCHUBERT, A. ROURA, W. P. SCHLEICH, W. ERTMER, and E. M. RASEL: ‘Quantum Test of the Universality of Free Fall’. *Physical Review Letters* (May 2014), vol. 112(20) (cit. on pp. 2, 5).
- [Sch14b] SCHLIPPERT, DENNIS: ‘Quantum tests of the universality of free fall’. PhD thesis. Gottfried Wilhelm Leibniz Universität Hannover, 2014 (cit. on p. 82).
- [Sch01] SCHRECK, F., G. FERRARI, K. L. CORWIN, J. CUBIZOLLES, L. KHAYKOVICH, M.-O. MEWES, and C. SALOMON: ‘Sympathetic cooling of bosonic and fermionic lithium gases towards quantum degeneracy’. *Physical Review A* (June 2001), vol. 64(1) (cit. on p. 45).
- [Sch18] SCHULZE, TORBEN ALEXANDER: ‘Quantum degenerate mixtures of ^{23}Na - ^{39}K and coherent transfer paths in NaK molecules’. PhD thesis. Gottfried Wilhelm Leibniz Universität Hannover, 2018 (cit. on p. 71).
- [Sei14] SEIDEL, STEPHAN TOBIAS: ‘Eine Quelle für die Interferometrie mit Bose-Einstein-Kondensaten auf Höhenforschungsraketen’. PhD thesis. Gottfried Wilhelm Leibniz Universität Hannover, 2014 (cit. on pp. 7, 9, 12, 35, 41).
- [Sil05] SILBER, C., S. GÜNTHER, C. MARZOK, B. DEH, PH. W. COURTEILLE, and C. ZIMMERMANN: ‘Quantum-Degenerate Mixture of Fermionic Lithium and Bosonic Rubidium Gases’. *Physical Review Letters* (Oct. 2005), vol. 95(17) (cit. on p. 41).
- [Sim08] SIMONI, ANDREA, MATTEO ZACCANTI, CHIARA D’ERRICO, MARCO FATTORI, GIACOMO ROATI, MASSIMO INGUSCIO, and GIOVANNI MODUGNO: ‘Near-threshold model for ultracold KRb dimers from interisotope Feshbach spectroscopy’. *Physical Review A* (May 2008), vol. 77(5) (cit. on pp. 50, 79).
- [Ste01] STECK, DANIEL A.: ‘Rubidium 87 D Line Data.’ Available online at <http://steck.us/alkalidata>. 2001 (cit. on p. 25).
- [Ste10] STECK, DANIEL A.: ‘Rubidium 85 D Line Data’. Available online at <http://steck.us/alkalidata>. 2010 (cit. on p. 25).
- [Ste09] STERN, G., B. BATTELIER, R. GEIGER, G. VAROQUAUX, A. VILLING, F. MORON, O. CARRAZ, N. ZAHZAM, Y. BIDEL, W. CHAIBI, F. PEREIRA DOS SANTOS, A. BRESSON, A. LANDRAGIN, and P. BOUYER: ‘Light-pulse atom interferometry in microgravity’. *The European Physical Journal D* (May 2009), vol. 53(3): pp. 353–357 (cit. on p. 3).
- [Ste18] STERNKE, TAMMO: ‘An ultracold high-flux source for matter-wave interferometry in microgravity’. PhD thesis. Carl von Ossietzky Universität Oldenburg, 2018 (cit. on pp. 66, 80).
- [Str16] STRAATSMAN, C. J. E., V. E. COLUSSI, M. J. DAVIS, D. S. LOBSER, M. J. HOLLAND, D. Z. ANDERSON, H. J. LEWANDOWSKI, and E. A. CORNELL: ‘Collapse and revival of the monopole mode of a degenerate Bose gas in an isotropic harmonic trap’. *Physical Review A* (Oct. 2016), vol. 94(4) (cit. on p. 66).

- [Str96] STRINGARI, S.: ‘Collective Excitations of a Trapped Bose-Condensed Gas’. *Physical Review Letters* (Sept. 1996), vol. 77(12): pp. 2360–2363 (cit. on p. 66).
- [Sun18] SUN, KUEI, KARMELA PADAVIĆ, FRANCES YANG, SMITHA VISHVESHWARA, and COURTNEY LANNERT: ‘Static and dynamic properties of shell-shaped condensates’. *Physical Review A* (July 2018), vol. 98(1) (cit. on p. 74).
- [Szc09] SZCZEPKOWSKI, J., R. GARTMAN, M. WITKOWSKI, L. TRACEWSKI, M. ZAWADA, and W. GAWLIK: ‘Analysis and calibration of absorptive images of Bose–Einstein condensate at nonzero temperatures’. *Review of Scientific Instruments* (May 2009), vol. 80(5): p. 053103 (cit. on pp. 44, 68).
- [Tac12] TACKMANN, G., P. BERG, C. SCHUBERT, S. ABEND, M. GILOWSKI, W. ERTMER, and E. M. RASEL: ‘Self-alignment of a compact large-area atomic Sagnac interferometer’. *New Journal of Physics* (Jan. 2012), vol. 14(1): p. 015002 (cit. on p. 1).
- [Tha08] THALHAMMER, G., G. BARONTINI, L. DE SARLO, J. CATANI, F. MINARDI, and M. INGUSCIO: ‘Double Species Bose-Einstein Condensate with Tunable Interspecies Interactions’. *Physical Review Letters* (May 2008), vol. 100(21) (cit. on pp. 5, 16, 79).
- [Tie19] TIECKE, TOBIAS: ‘Properties of Potassium’. 2019 (cit. on pp. 22, 37).
- [Tin14] TINO, G. M.: *Atom interferometry : proceedings of the International School of Physics "Enrico Fermi", course 188, Varenna on Lake Como, Villa Monastero, 15-20 July 2013*. Amsterdam, Netherlands: IOS Press, 2014 (cit. on p. 1).
- [Tor15] TORRALBO-CAMPO, LARA, GRAHAM D. BRUCE, GIUSEPPE SMIRNE, and DONATELLA CASSETTARI: ‘Light-induced atomic desorption in a compact system for ultracold atoms’. *Scientific Reports* (2015), vol. 5(14729) (cit. on p. 13).
- [Tou17] TOUBOUL, PIERRE et al.: ‘MICROSCOPE Mission: First Results of a Space Test of the Equivalence Principle’. *Physical Review Letters* (Dec. 2017), vol. 119(231101) (cit. on pp. 1, 3).
- [Tra18] TRAUTMANN, A., P. ILZHÖFER, G. DURASTANTE, C. POLITI, M. SOHMEN, M. J. MARK, and F. FERLAINO: ‘Dipolar Quantum Mixtures of Erbium and Dysprosium Atoms’. *Physical Review Letters* (Nov. 2018), vol. 121(21) (cit. on p. 71).
- [Tru18] TRUJILLO, KATERINE POSSO: ‘Theoretical study of the preparation of quantum degenerate mixtures for precision atom interferometry’. PhD thesis. Gottfried Wilhelm Leibniz Universität Hannover, 2018 (cit. on p. 5).
- [Tru01] TRUSCOTT, A. G.: ‘Observation of Fermi Pressure in a Gas of Trapped Atoms’. *Science* (Mar. 2001), vol. 291(5513): pp. 2570–2572 (cit. on p. 45).

- [Var09] VAROQUAUX, G., R. A. NYMAN, R. GEIGER, P. CHEINET, A. LANDRAGIN, and P. BOUYER: ‘How to estimate the differential acceleration in a two-species atom interferometer to test the equivalence principle’. *New Journal of Physics* (Nov. 2009), vol. 11(11): p. 113010 (cit. on pp. 2, 83).
- [Vog20] VOGT, CHRISTIAN, MARIAN WOLTMANN, SVEN HERRMANN, CLAUS LÄMMERZAHN, HENNING ALBERS, DENNIS SCHLIPPERT, and ERNST M. RASEL: ‘Evaporative cooling from an optical dipole trap in microgravity’. *Physical Review A* (Jan. 2020), vol. 101(1) (cit. on pp. 40, 56).
- [Wac15] WACKER, L., N. B. JØRGENSEN, D. BIRKMOSE, R. HORCHANI, W. ERTMER, C. KLEMP, N. WINTER, J. SHERSON, and J. J. ARLT: ‘Tunable dual-species Bose-Einstein condensates of K-39 and Rb-87’. *Physical Review A* (Nov. 2015), vol. 92(5) (cit. on pp. 49, 71).
- [Wan15] WANG, FUDONG, XIAOKE LI, DEZHI XIONG, and DAJUN WANG: ‘A double species Na-23 and Rb-87 Bose-Einstein condensate with tunable miscibility via an interspecies Feshbach resonance’. *Journal of Physics B: Atomic, Molecular and Optical Physics* (Nov. 2015), vol. 49(1): p. 015302 (cit. on p. 71).
- [Wan11] WANG, PENG-JUN, DE-ZHI XIONG, ZHENG-KUN FU, and JING ZHANG: ‘Experimental investigation of evaporative cooling mixture of bosonic Rb-87 and fermionic K-40 atoms with microwave and radio frequency radiation’. *Chinese Physics B* (Jan. 2011), vol. 20(1): p. 016701 (cit. on pp. 40, 41).
- [Wep18] WEPS, BENJAMIN, DANIEL LÜDTKE, TOBIAS FRANZ, OLAF MAIBAUM, THIJS WENDRICH, HAUKE MÜNTINGA, and ANDREAS GERNDT: ‘A model-driven software architecture for ultra-cold gas experiments in space’. *Proc. of the International Astronautical Congress, IAC*. International Astronautical Federation, IAF, 2018 (cit. on p. 31).
- [Wet03] WETTERICH, CHRISTOF: ‘Probing quintessence with time variation of couplings’. *Journal of Cosmology and Astroparticle Physics* (Oct. 2003), vol. 2003(10): pp. 002–002 (cit. on p. 1).
- [Wig16] WIGLEY, P. B., P. J. EVERITT, A. van den HENGEL, J. W. BASTIAN, M. A. SOORIYABANDARA, G. D. McDONALD, K. S. HARDMAN, C. D. QUINLIVAN, P. MANJU, C. C. N. KUHN, I. R. PETERSEN, A. N. LUITEN, J. J. HOPE, N. P. ROBINS, and M. R. HUSH: ‘Fast machine-learning online optimization of ultra-cold-atom experiments’. *Scientific Reports* (2016), vol. 6(25890) (cit. on pp. 31, 42).
- [Wil04] WILDERMUTH, S., P. KRÜGER, C. BECKER, M. BRAJDIC, S. HAUPT, A. KASPER, R. FOLMAN, and J. SCHMIEDMAYER: ‘Optimized magneto-optical trap for experiments with ultracold atoms near surfaces’. *Physical Review A* (2004), vol. 69(030901 (R)) (cit. on p. 14).

- [Wu17] WU, YU-PING, XING-CAN YAO, HAO-ZE CHEN, XIANG-PEI LIU, XIAO-QIONG WANG, YU-AO CHEN, and JIAN-WEI PAN: ‘A quantum degenerate Bose - Fermi mixture of K-41 and Li-6’. *Journal of Physics B: Atomic, Molecular and Optical Physics* (Apr. 2017), vol. 50(9): p. 094001 (cit. on p. 45).
- [Xio10] XIONG, DEZHI, PENGJUN WANG, HAIXIA CHEN, and JING ZHANG: ‘Evaporative cooling rubidium atoms with microwave radiation’. *Chinese Optics Letters* (2010), vol. 8(4): pp. 351–353 (cit. on p. 41).
- [Zha19] ZHAN, MING-SHENG et al.: ‘ZAIGA: Zhaoshan long-baseline atom interferometer gravitation antenna’. *International Journal of Modern Physics D* (July 2019), vol. 29(04): p. 1940005 (cit. on p. 2).
- [Zho19] ZHOU, LIN et al.: ‘United test of the equivalence principle at 10^{-10} level using mass and internal energy specified atoms’. (Apr. 15, 2019), vol. (cit. on p. 2).
- [Zoe10] ZOEST, T. van et al.: ‘Bose-Einstein Condensation in Microgravity’. *Science* (June 2010), vol. 328(5985): pp. 1540–1543 (cit. on p. 3).

List of Figures

1.1	Overview of microgravity experiments	4
2.1	CAD drawing of vacuum chamber	8
2.2	Vacuum pressure during vibrational test	10
2.3	CAD drawing of experimental chamber	11
2.4	CAD drawing of alkali ovens	12
2.5	Measurement of vapor pressure during heating and vibrational tests	13
2.6	Design of atom chip	14
2.7	Photograph of atom chip	15
2.8	Absorption detection setup	17
2.9	Calibration of second lens for absorption detection	18
2.10	Magnification of absorption detection	19
2.11	Overview of ground-based laser system	20
2.12	Level structure of ^{39}K and ^{41}K	22
2.13	Overview of potassium laser system	23
2.14	Level structure of ^{87}Rb and ^{85}Rb	25
2.15	Overview of rubidium laser system	26
2.16	Overview of electronics system	27
2.17	Setup for current driver characterization	29
2.18	Calibration of current drivers	30
2.19	Overview of whole scientific payload	32
3.1	Loading of single and mixed ^{41}K and ^{87}Rb MOTs	36
3.2	Loading of magnetic traps	37
3.3	Trapping potentials for ^{41}K and ^{87}Rb	39
3.4	Two-frequency microwave evaporation	40
3.5	Setup of microwave source	41
3.6	Evaporation ramp and phase space density	43
3.7	BEC phase transition of ^{87}Rb	44
3.8	Sympathetic cooling of ^{41}K	46
3.9	BEC mixtures with tunable particle numbers	47
3.10	^{41}K BECs for different ^{87}Rb atom numbers	48
3.11	Lifetime of ^{41}K , ^{87}Rb and mixture	49
3.12	Gravitational sag for ^{41}K and ^{87}Rb	51
3.13	Simulation of thermalization	53
3.14	Sympathetic cooling in different traps	54

4.1	Simulated Thomas-Fermi radii of ^{41}K and ^{87}Rb	62
4.2	Measurement of ^{41}K BEC expansion	63
4.3	Microwave spectroscopy of chip magnetic field decay	65
4.4	TrapFrequencyTransient	65
4.5	Collective excitations of ^{87}Rb	67
4.6	Collective excitations for ^{87}Rb for different ramps and mixtures	68
4.7	Measurement of ^{87}Rb BEC expansion	69
4.8	Gradient free switch-off of magnetic trap	70
4.9	Time-of-flight series with BEC mixtures	72
4.10	Simulation of ground states of an interacting ^{41}K - ^{87}Rb quantum mixture in g and μg	73
5.1	Delta-kick collimation of ^{41}K	79
5.2	Interferometry configuration, Raman double diffraction.	81
5.3	Beam splitter in MAIUS-B.	82

List of Tables

2.1	Random vibration test profiles with power spectral density (PSD) and root mean square (RMS) values along lateral and longitudinal axes.	9
2.2	Technical characteristics of bias coils.	16
3.1	Singlet (a_s) and triplet (a_t) zero-energy s-wave scattering length of ^{41}K and ^{87}Rb	45
3.2	Relative gravitational sag and calculated collision rates per atom $\Gamma_{\text{coll}}/(N_{\text{Rb}}N_{\text{K}})$ for different traps.	53

Publikationsliste

- *Coulomb crystallization of highly charged ions*
L. Schmöger, O. Versolato, M. Schwarz, M. Kohnen, A. Windberger, B. Piest, S. Feuchtenbeiner, J. Pedregosa-Gutierrez, T. Leopold, P. Micke, A. K. Hansen, T. M. Baumann, M. Drewsen, J. Ullrich, P. O. Schmidt, and J. R. Crespo López-Urrutia
Science **347**, 6227, 1233-1236 (2015).
- *Deceleration, precooling, and multi-pass stopping of highly charged ions in Be+ Coulomb crystals*
L. Schmöger, M. Schwarz, T. M. Baumann, O. Versolato, B. Piest, T. Pfeifer, J. Ullrich, P. O. Schmidt and J. R. Crespo López-Urrutia
Review of Scientific Instruments **86**, 10: 103111 (2015).
- *A dual-species atom interferometer payload for operation on sounding rockets*
M. Elsen, B. Piest, O. Anton, W. Bartosch, D. Becker, J. Böhm, S. Boles, K. Döringshoff, J. Grosse, O. Hellmig, C. Kürbis, M. Koch, M. D. Lachmann, M. Mihm, H. Müntinga, A. M. Nepal, T. Oberschule, A. Papakonstantinou, J. Perovske, A. Prat, J. Sommer, C. Spindeldreier, M. Warner, T. Wendrich, A. Wenzlawski, H. Blume, C. Braxmaier, M. Krutzik, C. Lämmerzahl, D. Lüdtke, A. Peters, K. Sengstock, A. Wicht, P. Windpassinger and E. M. Rasel
(in preparation)
- *Red and blue magneto-optical trapping with liquid crystal variable retarders*
B. Piest, V. Vollenkemper, J. Böhm, A. Herbst and E. M. Rasel
(in preparation)

Proceedings

- *MAIUS-B: A system for two-species atom interferometry in space*
B. Piest, M. D. Lachmann, O. Anton, W. Bartosch, D. Becker, J. Böhm, K. Döringshoff, M. Elsen, J. Grosse, C. kürbis, M. Mihm, M. Popp, T. Wendrich, A. Wenzlawski, C. Braxmaier, W. Ertmer, M. Krutzik, C. Lämmerzahl, A. Peters, A. Wicht, P. Windpassinger and E. M. Rasel
Proceedings of the 24th ESA Symposium on European Rockets and Balloon Programmes and related research, Essen (2019)
- *Final design of the MAIUS-2/3 payload - An atom interferometer on a sounding rocket*
M. Elsen, J. Grosse, T. Wendrich, W. Bartosch, M. D. Lachmann, D. Becker, B. Piest, K. Döringshoff, E. M. Rasel and C. Braxmaier
Proceedings of the 69th International Astronautical Congress, IAC, Bremen (2018)

Curriculum Vitae

Personalien

Name Baptist Piest
geboren am 19.09.1989 in Braunschweig
ledig, deutsch

Schulbildung

2008 Abitur am Gymnasium Martino-Katharineum in Braunschweig

Soziale Arbeit

2008-2009 Freiwilligendienst in Kumasi, Ghana

Studium

2009-2013 Bachelor-Studium Physik, Ruprecht-Karls-Universität Heidelberg
Bachelorarbeit: 'Charakterisierung des Ionenstrahls der Hyper-EBIT',
durchgeführt am Max-Planck-Institut für Kernphysik, Heidelberg.

2011-2012 Auslandsjahr, Eidgenössische Technische Hochschule Zürich

2013-2015 Master-Studium Physik, Ruprecht-Karls-Universität Heidelberg
Masterarbeit: 'Injektion, Speicherung und Abbildung hochgeladener
Argon-Ionen in der kryogenen Paul-Falle CryPTE_x', durchgeführt am
Max-Planck-Institut für Kernphysik, Heidelberg.

Promotion

09/2015 - heute Wissenschaftlicher Mitarbeiter am Institut für Quantenoptik, Leibniz
Universität Hannover

Acknowledgments

In den fünf bis sechs Jahren meiner Zeit als Doktorand im Institut für Quantenoptik haben mich eine Reihe von Menschen persönlich und wissenschaftlich begleitet und geprägt. Ihnen möchte ich an dieser Stelle danken.

Zuallererst möchte ich mich bei Ernst für seine Betreuung und vor allem sein Vertrauen bedanken, das er in mich gesetzt hat. Einem unbeschriebenen Blatt, welches erst neu in die Thematik einsteigt, den Aufbau und die Verantwortung für ein neues Experiment aufzutragen, zeugt für mich von dem Zutrauen welches er stets in seine Mitarbeiter*innen setzt. Die Zeit, die ich mit dem Aufbau und der Arbeit am Experiment verbringen durfte, zählt für mich zu den wohl lehrreichsten und interessantesten Lebensjahren!

In dieser Zeit lernte ich die kollegiale Atmosphäre am Institut für Quantenoptik kennen und schätzen. Anfangs im LNQE wurde ich von Maral, Michael und Jonas M. in die Geheimnisse der Atomchips und Vakuumtechnik eingeweiht und betreut. In der nachfolgenden Zeit im Labor habe ich sehr viel von Dennis B. gelernt: Dort konnten wir die erste Rubidium 2D-MOT erzeugen - die 3D-MOT ließ allerdings noch auf sich warten. Nach vielen Monaten ergebnisloser Suche, dem erneuten Öffnen der Vakuumkammer, der Bewahrheitung des ersten bitteren Verdachts und eine nagelneue DPS später hat auch das endlich geklappt. Hätte man mal alles gleich richtig gemacht! Vielen Dank an dieser Stelle an Waldemar für seine klugen Sprüche, sein umfassendes Wissen und Begeisterung für unsere Experimente.

Nach dem erfolgreichen MAIUS-1 Start bekam ich kompetente und gut organisierte Laborverstärkung von Maike und es ging richtig voran. Zusammen haben wir MAIUS-B in den nächsten Jahren Schritt für Schritt zum Kalium-BEC geführt - vielen Dank dafür.

Mit weiterer Verstärkung durch Jonas B. konnten wir alles aus dem Experiment rausholen. Besonderer Dank auch dafür, dass Du so gut mit meinem Musikgeschmack klarkommst. So haben selbst die eintönigsten Messtage und 4D-Scanfits viel Spaß gemacht!

Thijs, Wolle, Manuel und Papos möchte ich für die geduldige Unterstützung bei allen Elektronikproblemen danken - ohne Euer Rundum-sorglos-Elektronik-Paket wäre unser Experiment niemals so schnell vorangekommen. Dasselbe gilt auch für Arnau, Jan, Hauke und Holger: Danke für Euer grandioses Softwarepaket, das gemeinsame Debugging und Eure Nachsicht mit einem unwissenden und oft ungeduldigen Windows-User.

Dem restlichen, über das halbe Land verstreuten MAIUS-Team möchte ich für die tolle Zusammenarbeit danken. Vielen Dank insbesondere an Jens und Maike für die Leitung und Organisation des Projekts. Dank Eures Einsatzes bin ich sehr zuversichtlich, dass unsere langjährige Arbeit an diesem Projekt mit zwei erfolgreichen Raketenmissionen belohnt wird.

Ein großer Dank geht an all die Bachelorant*innen, FWJler*innen, Hiwis und Masterand*innen, die das Experiment und den Aufbau des Bodensystems wesentlich mitgeprägt haben: Alex, Allen, Hanna-Lina, Kai, Magdalena, Mareike, Ole, Steffen und Vera.

Auch von Theorieseite bekommen wir sehr viel Unterstützung. Hier möchte ich mich vor allem bei Annie, Gabriel, Naceur und Eric für die Erstellung und Durchführung der Simulationen und die reibungslose Zusammenarbeit bedanken.

Die besten Ideen und kreativsten Problemlösungen entstehen oft in Kaffeepausen und Diskussionen im Büro. Was für ein Glück, dass ich mein Büro mit zweien der wohl unermüdlichsten und unterhaltsamsten Kaffeetrinker des Instituts teilen konnte, Knut und Sebastian. Dank Sebastians Laborerfahrung und Experimentiergeschick konnten viele Probleme besonders schnell gelöst werden - wie schwer kann das sein?

Die schnelle und unkomplizierte, gleichzeitig aber genaue Fertigung mechanischer Komponenten ist die halbe Miete für ein gut funktionierende Experiment. Wir haben wirklich großes Glück, dass wir eine eigene Feinmechanikwerkstatt haben, die genau auf unsere Bedürfnisse eingeht und mit der die Kommunikation immer unglaublich gut funktioniert hat. Besonderer Dank geht hierbei an Alex V., Jonas P. und Mathias S..

Für kleinere Mechanik- und Elektronikprobleme war die Werkstatt von Kai-Martin der richtige Anlaufpunkt. Danke für Deine Geduld bei all meinen Fragen und Dein geradezu enzyklopädisches Wissen über unterschiedliche Steckerbauformen, die Farbcodierung von Widerständen bis hin zur korrekten Handhabung von Fräs- und Bohrmaschine.

Es gibt noch viele weitere (Ex-)Kolleg*innen am Institut, bei denen ich mich hier für die Zusammenarbeit, Freundschaft oder einfach nur für eine schöne Zeit bedanken möchte: Torben, Dennis S., Christian S., Sven, Mirco, Sina, Jan-Niclas, Robin, Étienne, Doro, Matze, Hendrik, Nina, Henning, Logan, Dominika und Klaus Z.

Keine Promotion, Dienstreise, Bestellung, Vertragsverlängerung oder Zolleinfuhr hätte ohne die unermüdliche Arbeit unserer Sekretariate funktioniert. Mein herzlicher Dank geht hierbei an Frau Göldner-Pauer, Frau Ohlendorf, Frau Faber, Elke und Katrin, Stephanie, Marina und Madeleine für Ihre/Eure Geduld mit mir.

Ein großes Dankeschön geht an all die sorgfältigen Korrekturleser*innen des Manuskripts: Kai, Jonas, Maike, Naceur, Felix, Vicky, Klaus D. und Waldemar. Danke an meinen Bruder Jakob für die unkomplizierte und schnelle Hilfe bei den Abbildungen.

Zuletzt möchte ich mich bei meinen Eltern Marion und Bernhard, meinen Geschwistern und all meinen Freund*innen bedanken - Ihr habt mich immer unterstützt, hattet ein Ohr für mich und habt mich aufgebaut, wenn die Dinge mal nicht so wie geplant liefen.